GENERATION OF FEMTOSECOND PULSES AT NEW WAVELENGTHS IN FIBER LASERS

A Dissertation

Presented to the Faculty of the Graduate School

of Cornell University

in Partial Fulfillment of the Requirements for the Degree of

Doctor of Philosophy

by

Yuxing Tang

August 2017

GENERATION OF FEMTOSECOND PULSES AT NEW WAVELENGTHS IN FIBER LASERS

Yuxing Tang, Ph.D.

Cornell University 2017

The advancement of ultrafast laser sources has enabled both new discoveries in fundamental research and the development of many practical applications, such as nonlinear microscopy, biomedical imaging, micro-machining, laser surgery, etc. Among the light sources, solid-state laser systems, such as Ti:sapphire lasers, have long served as the workhorses to provide the femtosecond pulses with high peak power and average power. As versatile as they are, the accompanying prices to pay are the bulky size, high cost, requirement for water-cooling and high sensitivity to alignment, which are all impediments for their operations outside the laboratory environments.

Rare-earth doped fiber lasers come naturally with the advantages of being alignment-free, compact and possessing large surface-to-volume ratio for efficient heat dissipation at low costs. Single mode fibers provide nearly perfect gaussian beams for applications. Starting from the year of 2006 when the all-normal dispersion fiber lasers were discovered, researchers have devoted great efforts to studying nonlinear pulse evolution and ultrashort pulse generation in fiber lasers with high energy and peak power. Multiple novel pulse evolutions have been thoroughly explored, including dissipative soliton, passive self-similar, amplifier similariton and extended self-similar evolution. The performance of fiber lasers have also been boosted up to the comparable level as that of the Ti:sapphire lasers.

With all these pulse evolutions and mechanisms studied and well understood,

there is still work to be done about fiber lasers, such as the exploration of femtosecond pulse generations in the few-cycle regime and at other new wavelengths. The study of few-cycle pulse generation directly from fiber oscillators is first explored in an erbium laser with comb-like dispersion decreasing fiber, based on the idea of the extended self-similar evolution.

Most of the fiber laser developments have been focused on using the gain medium of erbium and ytterbium with emission peaks around 1030 nm and 1550 nm. Thulium (Tm) doped and thulium-holmium codoped fibers emit light covering 1.7 to 2.1 μm with a 100-nm wide gain bandwidth, which opens the door for many other applications. The benefits of operating Tm fiber lasers with net normal dispersion cavities are explored in this thesis. A Tm-doped fiber laser with hybrid pulse evolution with elements of self-similar evolution is demonstrated, with a 4-fold improvement in peak power over previous results. Similar thoughts can be applied to erbium doped ZBLAN fiber lasers operating at 2.8 μm, at which wavelength only soliton lasers have been realized. Simulations predict promising results in cavities with dispersion management and some initial experimental results are presented.

To further pursue the femtosecond pulse generation over 3 μm into the mid-infrared region, a fiber-based laser system employing the soliton self-frequency shift in fluoride fibers is investigated. Soliton pulses with 100-fs duration, nanojoule-level energies are generated, with wavelength tunable from 2-4.3 μm. Compared with previous reports, the pulse energies are two orders of magnitude higher and the range of wavelengths is extended by 1000 nm.

Finally, future directions and the extension of the work in the thesis are discussed.

BIOGRAPHICAL SKETCH

Yuxing Tang was born in Xi'an, Shaanxi, China in 1990. Brought up in a family of an engineer and a doctor, he is always curious about the world around him and like to ask various questions starting from a young age. He got interested in math and natural sciences in middle school. Following high school in 2008, he decided to major in electronics engineering in Peking University. Thanks to the comprehensive course settings of the program, he also got a chance to study all the undergraduate physics courses in addition to learning how to design integrated and digital circuits.

Intrigued by the optics course he took in the sophomore year, he wanted to learn more about nonlinear optics and participated in a research group to work on laser experiments, such as building up fiber lasers for medical applications. He found it fascinating and enjoyed the process of obtaining the rainbow-like light from the "mysterious" processes he couldn't understand at that time. Upon graduation with a bachelor's degree in 2012, he opted to pursue Ph.D. studies in nonlinear optics and fiber lasers.

Luckily, he got enrolled in the Applied Physics Ph.D. program at Cornell University. After the first year's exploration of the research directions in the department, he decided to join the fiber laser group of Prof. Frank Wise in the summer of 2013. Since then, he's greatly enjoyed his time in the group researching on nonlinear fiber optics and ultrashort pulse generations at new colors.

After completing his Ph.D., he will step on a new journey in San Francisco, CA to work as a quantitative analyst and hope to explore his technical and modeling skills in other areas as well.

To my wife, Yi, and my parents for their constant support and unwavering love.

ACKNOWLEDGEMENTS

First, I would like to give my sincere thanks to Prof. Frank Wise for all of his help, support, and guidance during my time at Cornell. I truly appreciate the opportunity of learning from someone as knowledgable and kind as Frank, and it has been an honor to be a member of his team. I learnt from him not only the knowledge of physics and ways of thinking, but also the philosophy of how to make life-changing choices.

I also want to thank my committee members, Prof. Clifford Pollock and Prof. Jeffrey Moses, for their support and guidance in various aspects of my academic life.

I give special thanks to my wife Yi Xin for all of her help, encouragement, support for all these years, and to my parents for always being there and supporting me whenever I couldn't get the lasers mode-locked. I am indebted to them for all their care and understanding.

I also appreciate the help and friendship of my group members, including Will Renninger, Hui Liu, Erin Lamb, Peng Li, Jun Yang, Logan Wright, Zhanwei Liu, Zimu Zhu, Walter Fu, Zachary Ziegler, Andrei Isichenko and Pavel Sidorenko. I additionally thank Logan for the insightful discussions with him and his help all along.

I have also enjoyed the chance to work with some excellent collaborators and am grateful to them too. In particular, I thank Andy Chong, Kriti Charan, Tianyu Wang and Prof. Chris Xu for collaborating with me.

Finally, I want to thank the National Science Foundation for providing financial support for my work presented in this thesis.

TABLE OF CONTENTS

Biographical Sketch . . . iii
Dedication . . . iv
Acknowledgements . . . v
Table of Contents . . . vi
List of Tables . . . viii
List of Figures . . . ix

1 Introduction 1
1.1 Organization of thesis . . . 3
1.2 Pulse propagation in fiber . . . 4
1.2.1 Generalized nonlinear Schrödinger equation . . . 4
1.2.2 Simulating the fiber laser cavity . . . 6
1.3 Pulse evolutions in fiber lasers . . . 9
1.3.1 Soliton lasers . . . 11
1.3.2 Dispersion-managed soliton lasers . . . 12
1.3.3 Dissipative soliton lasers . . . 13
1.3.4 Passive self-similar lasers . . . 14
1.3.5 Amplifier similariton lasers . . . 16
1.3.6 Extended self-similar lasers . . . 18
1.4 Fiber laser components . . . 19
1.4.1 Spectral filters . . . 19
1.4.2 Saturable absorbers . . . 23

Bibliography 28

2 Self-similar pulse evolution in a fiber laser with comb-like dispersion decreasing fiber 31
2.1 Introduction . . . 31
2.2 Er fiber laser with comb-like dispersion-decreasing fiber . . . 33
2.2.1 Modeling . . . 34
2.2.2 Experiments . . . 38
2.2.3 Discussion . . . 40
2.3 Yb fiber laser with comb-like dispersion-decreasing fiber . . . 42
2.4 Conclusion . . . 44

Bibliography 45

3 High energy pulses from thulium fiber lasers 47
3.1 Introduction . . . 47
3.2 Laser design and numerical simulations . . . 49
3.3 Experiments . . . 52
3.4 Conclusion . . . 55

Bibliography **57**

4 Generation of intense 100-fs solitons tunable from 2 to 4.3 μm in fluoride fiber **59**
4.1 Introduction . . . 59
4.2 Description of fibers . . . 62
4.3 Numerical simulations . . . 63
4.4 Experiments . . . 67
4.5 Stability measurement . . . 72
4.6 Discussion . . . 73
4.7 Conclusion . . . 74

Bibliography **75**

5 High energy pulses from erbium ZBLAN fiber lasers **78**
5.1 Introduction . . . 78
5.2 Laser design and numerical simulations . . . 80
5.2.1 Chalcogenide fiber . . . 80
5.2.2 Laser design and simulation setup . . . 82
5.2.3 Simulation results for dispersion-managed soliton lasers . . . 84
5.2.4 Simulation results for hybrid self-similar lasers . . . 87
5.3 Experiments . . . 89
5.3.1 Fiber cleaving . . . 89
5.3.2 Soliton laser . . . 90
5.4 Conclusion . . . 92

Bibliography **94**

6 Future Directions **96**
6.1 Thulium fiber lasers with all normal-dispersion cavity . . . 96
6.1.1 Modulation instability in Tm fiber laser . . . 96
6.1.2 Dissipative soliton Tm fiber laser . . . 98
6.1.3 Amplifier similariton Tm fiber laser . . . 100
6.2 Divided-pulse Tm laser . . . 102
6.3 Modelocked praseodymium fiber laser at 5 μm and its application . 106

Bibliography **109**

A Appendix A: Fiber parameters **111**
A.1 Mathematica code for calculating the fiber parameters . . . 111

LIST OF TABLES

2.1 Values of Parameters Used in Simulation 36
2.2 Parameters Used in Simulation for Yb DDF laser 42

3.1 Values of parameters used in Tm laser simulation 50

5.1 Values of parameters used in the Er ZBLAN laser simulations . . . 84

6.1 Values of fiber parameters used in the Tm ANDi laser 99
6.2 Values of fiber parameters used in the Tm amplifier similariton laser 101

LIST OF FIGURES

1.1 Schematic of the all-normal dispersion fiber laser: BPF: bandpass filter; PBS: polarizing beam splitter; ISO: isolator; QWP: quarter waveplate; HWP: half waveplate; SMF: single mode fiber. 7
1.2 The simulation results of the Yb fiber laser cavity: (a) output spectrum; (b) output chirped pulse profile; (c) transform limited pulse; (d) pulse evolution in spectral and temporal domains. (position 1-11: passive fiber; position 12-21: gain fiber; position 22-31: passive fiber; position 32: SA; position 33: output port.) 9
1.3 Schematic of the dispersion managed soliton design. 12
1.4 The concept of the extended self-similar laser design. 18
1.5 Transmission function of a Birefringent filter made of a 12-T (6 mm thick) quartz plate near 1030 nm. 21
1.6 A Lyot filter, consisting of a sequence of birefringent crystals (BC) and polarizers (P). Each birefringent plate has the thickness half of the previous one. 22
1.7 Transmission function of a Lyot filter made of a 6 T and 12 T quartz plate near 1900 nm. The bandwidth is 35 nm and the free spectral range is 150 nm. 22
1.8 Schematic of a grating-based filter. 23
1.9 A 1-nm bandwidth grating filter at 1030 nm. (a) The transmission profile of the filter; (b) The incident and diffracted angle of the beam; The dependence of the introduced (c) 2nd order and (d) 3rd order dispersion on distance between the collimator and the grating. 24
1.10 Illustration of saturable absorbers promoting pulse generation. . . 24
1.11 Illustration of NPE saturable absorber (PBS: polarizing beam splitter; QWP: quarter waveplate; HWP: half waveplate). 26

2.1 Comparison of the GVD values of the ideal DDF (green) with the comb-like DDF (blue) at 1550 nm. The lengths of the segments are 14, 6, 5, 20, 5 and 50 cm. The upper and lower red dashed lines are for the ideal DDF at 1700 and 1400 nm, respectively. 35
2.2 (a) Schematic of the Er DDF laser: PBS: polarizing beam splitter; QWP: quarter-wave plate; HWP: half-wave plate. (b)-(d) Simulation results for an ideal (red) or a comb-like DDF (black), with net cavity dispersion of -0.087 ps^2. (b) Evolution of pulse duration (SA, saturable absorber; SF, spectral filter). (c) Evolution of spectral bandwidth. (d) Evolution of misfit parameter. 37
2.3 (a) Measured mode-locked spectrum of the Er DDF laser. (b) Fitting of the cross correlation signal to a parabola. (c) Interferometric autocorrelation of the dechirped pulse using two-photon absorption. (d) Radio frequency spectrum of the mode-locked laser with resolution bandwidth of 10 Hz and span range of 100 kHz. 39

2.4 (a) The pulse spectrum at the input and output end of the peak power testing segment with coupled-in energy of 0.54 nJ. (b) Comparison of the spectral broadening in experiments (in black) and simulations (Gaussian pulses; in red) at different input energy level. 40
2.5 (a) Pulse energy and dechirped pulse duration at various cavity dispersions. (b) Pulse chirp and deviation of dechirped pulse duration from the transform limit at various cavity dispersions. 41
2.6 (a) Schematic of the Yb DDF laser: PBS: polarizing beam splitter; QWP: quarter-wave plate; HWP: half-wave plate. (b) Comparison of the GVD values of the ideal DDF (green) with the comb-like DDF (blue) at 1030 nm. (c)-(d) Comparison of the output spectra and dechirped pulse (using comb DDF) with transform limit pulse. 43

3.1 Schematic of laser: BRP: birefringent plate; IF: interference filter; PBS: polarizing beam splitter; ISO: isolator; WDM: wavelength-division multiplexer. 50
3.2 (a) Simulated variation of pulse duration and spectral bandwidth along the cavity (SA: saturable absorber, SF: spectral filter). The pigtail segment of WDM is neglected for clarity; (b) pulse shape evolution compared with a parabolic pulse; inset: comparison of pulse shape after UHNA4 (black) with Gaussian pulse (blue) and parabolic pulse (red) in log scale. 51
3.3 (a, b) Comparison between experimental and simulation results (squares: experimental data, triangles: simulation results); (c) mode-locked spectra at various cavity GDD with the 16-nm filter (blue: 0.08 ps^2, green: 0.17 ps^2, red: 0.26 ps^2, black: 0.37 ps^2); (d) mode-locked spectra with varying filter BW at cavity GDD $\sim$ 0.28 ps^2 (blue: 16 nm filter BW, black: 35 nm filter BW, red: 40 nm filter BW). 53
3.4 Experimental (a) output spectrum, (b) autocorrelation of dechirped pulse (inset: autocorrelation of transform limited pulse), (c) radio-frequency spectrum (span range: 200 kHz, RBW: 1 kHz) corresponding to 7.6 nJ pulse energy. 54

4.1 The parameters of the fluoride fibers used in the experiments. The group velocity dispersion (GVD) of the fundamental mode and the propagation loss for the (a) InF_3 fiber; (b) ZrF_4 fiber. The horizontal blue dashed line indicates the position of the zero GVD value. The vertical blue dashed line indicates the single mode cutoff wavelength. 63
4.2 Simulation results for the (a) spectral output, (b) spectral evolution, (c) temporal output and (d) temporal evolution in a 2-m long InF_3 fiber with 40-nJ and 70-fs pulses coupled into the fundamental mode. RS: Raman soliton of interest at the longest wavelength. . . 66

4.3 Schematic of the experimental setup for SSFS in fluoride fibers: LPF: long pass filter. LPF1 cuts on at 1.8 μm. LPF2 cuts on at 2.85 μm or 3.75 μm. 68
4.4 (a) The spectra and (b) the interferometric autocorrelation of the input light source at 1.9 μm. 68
4.5 Measured spectra and the interferometric autocorrelations of the most-redshifted solitons at (a,b) 3.2 μm; (c,d) 3.9 μm; (e,f) 4.3 μm in the InF_3 fiber. The red lines indicate the spectra after noise reduction. A deconvolution factor of 1.54 was assumed to obtain the indicated pulse durations. 69
4.6 Measured full spectra in a 2-m long InF_3 fiber with shifted solitons at 3.9 μm. PSD: power spectral density. 70
4.7 Spectra of the most redshifted soliton in the 2-m long InF_3 fiber at different wavelengths in (a) experiments; (b) numerical simulations. The dotted lines show the range which could not be covered by available spectrum analyzers. The soliton and input-pulse energies are indicated. 71
4.8 The stability measurement of the power and center wavelength variation of (a,b) the pump pulse; (c,d) the seed pulse; (e,f) the output soliton at 3.6 μm. SD: standard deviation. 72

5.1 Group velocity dispersion of the chalcogenide fiber IRF-S-6.5. . . . 81
5.2 (a) Measurement of n_2 of the chalcogenide fiber IRF-S-6.5 using peak power test; (b) Extrapolation of n_2 at longer wavelengths using Miller's formula. 81
5.3 Schematic of the Er ZBLAN laser with dispersion compensation: PBS: polarizing beam splitter; ISO: isolator; BPF: bandpass filter; M: mirror; DM: dichroic mirror. 83
5.4 (a) Simulated variation of pulse duration and spectral bandwidth with net cavity dispersion of -0.0084 ps^2 (Page 22: spectral filter, Page 23: output port); (b) comparison between the output pulse and transform-limit pulse; (c) output spectrum with FWHM bandwidth of 60 nm. 85
5.5 (a) Simulated variation of pulse duration and spectral bandwidth with net cavity dispersion of 0.012 ps^2 (Page 22: spectral filter, Page 23: output port); (b) output chirped pulse with duration of 177 fs; (c) comparison between the de-chirped pulse and transform-limit pulse; (d) output spectrum with FWHM bandwidth of 137 nm, corresponding to 106 fs. 86

5.6 (a) Simulated pulse duration and spectral bandwidth with net cavity dispersion of 0.1 ps^2 (Page 22: spectral filter, Page 23: output port); (b) comparison between the de-chirped pulse and transform-limit pulse; (c) misfit parameter evolution compared with a parabolic pulse; (d) the output spectrum with FWHM bandwidth of 110 nm and pulse energy of 188 nJ. 88
5.7 The end view, front view and back view of the bad angle cleave (top row) and good angle cleaves (bottom row). 90
5.8 Schematic of the Er ZBLAN soliton laser: PBS: polarizing beam splitter; ISO: isolator; BPF: bandpass filter; M: mirror; DM: dichroic mirror. 91
5.9 Picture of the Er ZBLAN soliton laser.Line with red color indicates the pump beam and the green one is the signal light. 91
5.10 Slope efficiency of the Er ZBLAN soliton laser. 92

6.1 (a) Mode-locked spectrum from the Tm fiber laser in Figure 3.1; (b) Zoomed-in spectrum in THz unit with multiple peaks indicated. 98
6.2 The schematic of the all normal-dispersion Tm laser design with filter bandwidth of 50 nm. 99
6.3 (a) Simulated output chirped pulse; (b) output spectrum with 150-nm bandwidth and 280-nJ pulse energy; (c) spectral and temporal evolution along the cavity; (d) comparison between the de-chirped pulse (90 fs) and the transform-limit pulse (70 fs). 100
6.4 (a) Evolution of the misfit parameter comparing the pulse profile to a parabola; (b) output spectrum with 87-nm bandwidth; (c) spectral and temporal evolution inside the cavity; (d) comparison between the de-chirped pulse (97 fs) and the transform-limit pulse. 101
6.5 Schematic for the divided-pulse Tm fiber laser: BRP: birefringent plate; PBS: polarizing beam splitter; ISO: isolator; F.R: Faraday Rotator; M: mirror. 103
6.6 (a) Modelocked spectrum; (b) autocorrelation of the Tm soliton laser in divided-pulse configuration. 104
6.7 Schematic for the divided-pulse Tm fiber laser with NPE for mode-locking. 105
6.8 Mode-locked spectrum (a) and autocorrelation (b) of the Tm soliton laser in divided-pulse configuration, without SESAM. 105
6.9 Broadband emission in the 3$\sim$5 μm wavelength region from a diode-pumped Pr^{3+} doped chalcogenide fiber source. 108

CHAPTER 1

INTRODUCTION

The advancement of scientific research and industrial applications is accompanied by the development of versatile laser sources. Among them, ultrafast laser sources enable the researchers to dive into the regime of nonlinear optical sciences, as well as various important applications, including biomedical imaging, laser surgery, frequency metrology and material processing. It wouldn't be possible to observe and study the most fundamental and interesting nonlinear optical phenomena without these energetic femtosecond pulses. The continued and rapid growth in applications will also require and benefit from the developments of ultrafast laser sources.

Solid state lasers, represented by mode-locked titanium sapphire (Ti:sapphire) lasers, have long served as the main driving forces for ultrafast sciences and dominated the laser markets. Perceived as a gift from the nature, Ti:sapphire crystal has great material properties and a hugely broad gain bandwidth in the visible range, which supports the generation of sub-10 fs pulses. With the discovery of Kerr-lens mode-locking in 1991 [1] and two decades of engineering, Ti:sapphire lasers have achieved a huge success and largely used as femtosecond light sources. However, their widespread applications are still limited by a few factors, such as the high cost, bulky size, cooling requirement and high sensitivity to the alignment. Laser technicians or staff with special training are required to operate the Ti:sapphire lasers routinely and continuously. This, along with their bulky sizes, prevent them from being used by doctors in the real clinical environments.

Fiber lasers possess the intrinsic properties of being robust, compact and cost effective. They have grown into important high energy ultrashort pulsed sources

both in scientific research and applications. With the maturity of manufacturing fiber components at low cost, it becomes quick and easy to assemble a fiber laser using fibers out of the shelves and splicing them together. The large gain provided by the highly-doped gain fibers enable fiber lasers to tolerate large losses and high output coupling ratio. The light is guided inside the waveguide and has a perfect Gaussian beam profile in single mode fibers. The prospect of all-fiber-format lasers will totally eliminate the free space components and shrink the size of femtosecond fiber lasers to that of a briefcase. It requires no or minimal water cooling due to the fiber's large surface-to-volume ratio for efficient hear dissipation.

Another main reason for the fast development of fiber lasers is the discovery of various pulse evolutions in laser cavities. Since the discovery of the all normal dispersion (ANDi) fiber laser [2], the performance has increased by orders of magnitude from the previous soliton and dispersion-managed soliton lasers, starting to compete with the performance of Ti:sapphire lasers. It remains a question to see how short pulses fiber lasers can generate directly from oscillators, since these broadband pulses can replace the role of those from Ti:sapphire lasers.

Despite the improvement in output pulse energy and durations, fiber lasers still lag behind solid state lasers in delivering light at new colors. Fiber-based light sources at new wavelengths are greatly needed for various types of applications and their developments also open doors for new ideas. It's interesting and exciting to see how the idea of operating fiber lasers in the normal dispersion regime works for other wavelengths and what the scaling rules of performance are. In particular, people are becoming increasingly interested in developing light sources into the mid-infrared region over 3 μm, which is beneficial to a full range of new applications.

1.1 Organization of thesis

This thesis focuses on the study of generating few-cycle pulses directly from fiber lasers as well as the routes to obtain femtosecond pulses from fiber lasers at new wavelengths. The detailed introductions are organized as follows.

Chapter 1 introduces the basic concepts and modeling of pulse propagation in optical fibers and fiber lasers. Multiple important pulse evolutions are summarized. Finally, a brief description of the important components used in fiber lasers is presented.

Chapter 2 presents the work on generation of sub-40 fs pulses in an erbium (Er) fiber laser with a comb-like dispersion decreasing fiber. A hybrid pulse evolution with elements of passive self-similar evolution is discovered and the pulse performance shows a 4-fold improvement over previous results. Promising simulation results of applying the same idea to a ytterbium (Yb) fiber laser are discussed.

Chapter 3 describes the study of a thulium (Tm) fiber laser at 2 μm operating at net normal dispersion regime. Its behavior with varying cavity dispersion and filter bandwidth is studied systematically. This is the first Tm fiber laser that reaps the benefits of normal dispersion operation.

Chapter 4 demonstrates the routes to obtain 100-fs solitons, continuously wavelength-tunable over 2-4.3 μm through the soliton self-frequency shift (SSFS) in fluoride fibers. The pulse energies are 2 orders of magnitude higher than those previously achieved by SSFS, around 3 μm, and the range of wavelengths is extended by 1000 nm. Peak power ranges from 20 to 75 kW are achieved across the tuning range.

Chapter 5 describes the efforts to develop normal dispersion Er ZBLAN fiber lasers at 2.8 μm. Promising simulation results show an order of magnitude improvement over those of the previous soliton lasers at this wavelength. Some initial experimental results are presented.

Finally, future directions of these work will be discussed in Chapter 6.

1.2 Pulse propagation in fiber

The propagation of optical fields in fibers is governed by the generalized nonlinear Schrödinger equation (GNLSE), which can be derived from the Maxwell's equations. The derivations are presented in [3] in detail. Some main results related to this thesis are listed below.

1.2.1 Generalized nonlinear Schrödinger equation

Normally, we start with the equation below:

$$\nabla^2 \mathbf{E} - \frac{1}{c^2}\frac{\partial^2 \mathbf{E}}{\partial t^2} = \mu_0 \frac{\partial^2 \mathbf{P}_L}{\partial t^2} + \mu_0 \frac{\partial^2 \mathbf{P}_{NL}}{\partial t^2}, \tag{1.1}$$

where $\mathbf{E}(\mathbf{r}, t)$ is the electric field, c is the speed of light in vacuum. $\mathbf{P}_L$ and $\mathbf{P}_{NL}$ are the linear and nonlinear portions of the induced polarization and μ_0 is the magnetic permeability in free space.

Under the assumptions of slowly varying envelop approximation (SVEA) and the optical fields being quasi-monochromatic ($\frac{\Delta\omega}{\omega_0} \ll 1$), the slowly varying part

$A(z,t)$ of the full electric field $\mathbf{E}(\mathbf{r},t)$ can be factored out:

$$\mathbf{E}(\mathbf{r},t) = \frac{1}{2}\hat{x}(F(x,y)A(z,t)\exp\left[i(\beta_0 z - \omega_0 t)\right] + c.c.), \tag{1.2}$$

where *F(x,y)* is the spatial distribution of the field in the cross section of fibers and *c.c.* stands for the complex conjugate. With a further assumption that the optical field maintains the polarization along propagation, we can regard this as a scalar model. In practice, it works quite well, but if needed, a vector code modeling two polarization directions is used. After factoring out the rapidly varying part of the field, we can arrive at the GNLSE:

$$\begin{aligned}\frac{\partial A}{\partial z} + \frac{\alpha}{2}A - \sum_{n=2}^{\infty} i^{n+1}\frac{\beta_n}{n!}\frac{\partial^n A}{\partial t^n} = \\ i\gamma\left(1 + \frac{i}{\omega_0}\frac{\partial}{\partial t}\right)\left(A(z,t)\int_{-\infty}^{t} R(t')|A(z,t-t')|^2 dt'\right).\end{aligned} \tag{1.3}$$

where *R(t)* is the normalized nonlinear response function, β_n are the n-th order of the fiber's dispersion. Linear loss is introduced through the term α. Nonlinear coefficient $\gamma = \frac{n_2(\omega_0)\omega_0}{cA_{eff}}$ models the Kerr nonlinear effect in fibers. One point needs to be made here that γ scales inversely with the third power of wavelength, which indicates the potential benefits of lasers at longer wavelengths.

The nonlinear response function *R(t)* incorporates both the electronic and the nuclear contributions and takes the form:

$$R(t) = f_R h_R(t) + (1 - f_R)\delta(t - t_e) \tag{1.4}$$

where t_e represents the instantaneous electronic response time [3]. The proportion

of contribution from delayed Raman response is controlled by f_R, which is 0.18 for silica fibers. It's hard to determine the exact form of the Raman response function $h_R(t)$, which is approximated in simulations by a simple model:

$$h_R(t) = \frac{\tau_1^2 + \tau_2^2}{\tau_1 \tau_2^2} exp(-t/\tau_2) sin(t/\tau_1) \tag{1.5}$$

The parameters τ_1 and τ_2 are two time constants unique to the material and are chosen to match the actual Raman gain spectrum. For silica glasses, values of $\tau_1 = 12.2fs$, $\tau_2 = 32fs$ are used [4].

This equation can model 3rd order nonlinear effects, including self-phase modulation, stimulated Raman scattering, self-steepening, and shock formation. It is capable of modeling pulses as short as a few optical cycles, which is sufficient for the scope of the thesis.

Sometimes, when the pulse duration is long enough ($>$ 100 fs), a simplified version of GNLSE is used, given by the nonlinear Schrödinger equation (NLSE).

$$\frac{\partial A}{\partial z} = -\frac{i\beta_2}{2}\frac{\partial^2 A}{\partial t^2} + i\gamma|A|^2 A, \tag{1.6}$$

This equation can be solved using the inverse scattering method and yields the important soliton solution when the group velocity dispersion β_2 is anomalous.

1.2.2 Simulating the fiber laser cavity

As the illustration of numerical simulation of a fiber laser cavity, we consider the all-normal dispersion fiber laser design in Figure 1.1 working at 1 μm. Single

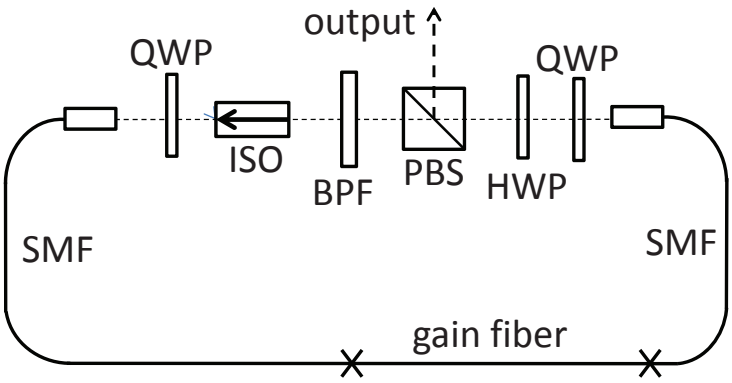

Figure 1.1: Schematic of the all-normal dispersion fiber laser: BPF: bandpass filter; PBS: polarizing beam splitter; ISO: isolator; QWP: quarter waveplate; HWP: half waveplate; SMF: single mode fiber.

mode fiber is Hi1060 and the gain fiber is Yb doped fiber. The laser is mode-locked through nonlinear polarization evolution (NPE), implemented by wave plates and polarizing beam splitter (PBS). PBS also serves as the output port for the cavity. The isolator ensures unidirectional operation of the laser. The band-pass filter is a critical element for stabilizing a positively chirped pulse circulating inside the normal dispersion cavity.

Pulse propagation inside the cavity is modeled using the following NLSE with gain term:

$$\frac{\partial A(z,\tau)}{\partial z} + i\frac{\beta_2}{2}\frac{\partial^2 A(z,\tau)}{\partial \tau^2} = i\gamma|A(z,\tau)|^2 A(z,\tau) + g(E_{pulse})A(z,\tau) \tag{1.7}$$

$A(z,\tau)$ is the electric field envelope, where z is the propagation distance and τ models the local time in the frame moving at the group velocity of the pulse. Group velocity dispersion (GVD) is modeled using β_2, which is 23 fs^2/mm for Hi1060 at 1 μm. γ is the Kerr nonlinear coefficient of the single mode fiber, with the value of 0.0047 /(W·m). The gain term only appears in the gain segment and

the saturation of the gain fiber is modeled through $g(E_{pulse}) = g_0/(1+E_{pulse}/E_{sat})$, where g_0 is the small signal gain corresponding to 30 dB. E_{pulse} is the total intra-cavity pulse energy in a round trip, which is $\int_{-T_R/2}^{T_R/2} |A(z,t)|^2 dt$. The modeling of the pump power level is introduced via E_{sat}.

Mode-locking is achieved using NPE, but it's modeled in simulations as an ideal saturable absorber with monotonically-increasing transmission curve of $T(t) = 1 - l_0/(1 + P(t)/P_{sat})$, where l_0 is the unsaturable loss, with $l_0 = 1$ for a perfect SA [5]. P_t is the instantaneous pulse power and P_{sat} is the saturation power of the SA, which is normally 1$\sim$4 kW in simulations. The linear loss and the output coupling ratio of 70% are used. The simulation can be seeded with Gaussian white noise or a pulse, which may speed up the convergence process.

Split-step Fourier method is used in this thesis [3], by modeling the dispersion part $\hat{D}$ in frequency domain and the nonlinear part $\hat{N}$ in time domain using fourth-order Runge Kutta method. Propagation is conducted over a very small longitudinal distance h each time and the accuracy of the method is limited on the order of $O(h^2)$. The accuracy of the algorithm can be improved by employing the symmetric split-step Fourier method, where the dispersion part is split into two halves and modeled symmetrically before and after the nonlinear part. Then the accuracy of $O(h^3)$ can be achieved.

The converged solution for the cavity with 2-m SMF, 1-m gain fiber and 1-m SMF is shown in Figure 1.2. A 10-nm bandwidth filter is used and the saturation energy for the gain segment is 5.7 nJ. Under these conditions, the laser generates chirped pulses with 8-nJ energy and 3.8-ps duration. The spectra has the characteristic bat-man ears and steep edges [6]. With increasing pump power, or increasing saturation energy of the gain fiber, higher pulse energy and broader

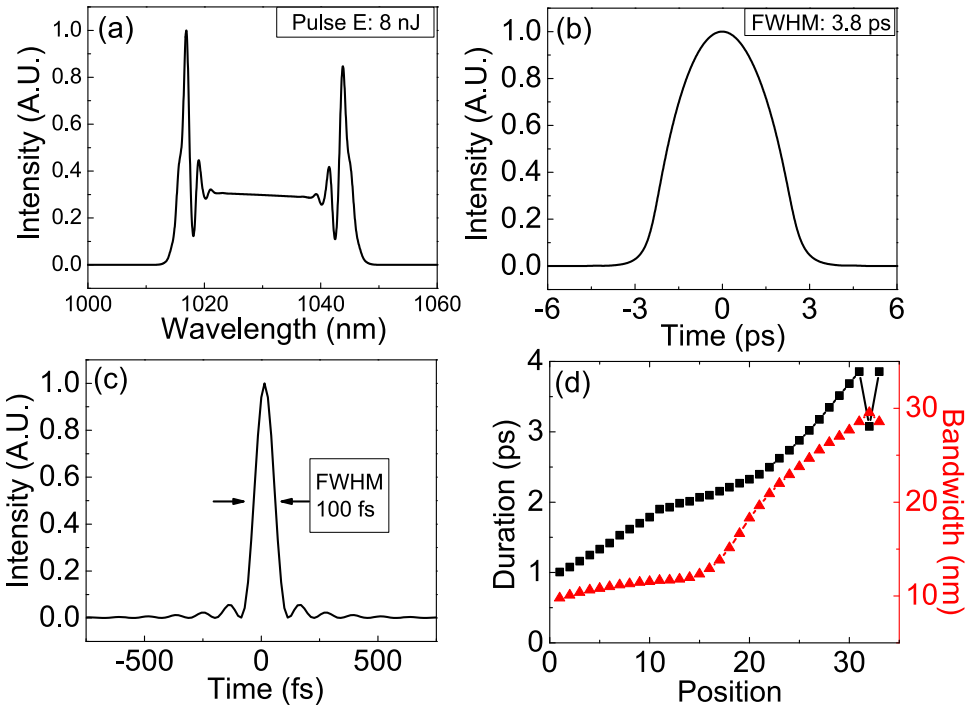

Figure 1.2: The simulation results of the Yb fiber laser cavity: (a) output spectrum; (b) output chirped pulse profile; (c) transform limited pulse; (d) pulse evolution in spectral and temporal domains. (position 1-11: passive fiber; position 12-21: gain fiber; position 22-31: passive fiber; position 32: SA; position 33: output port.)

spectrum is produced.

1.3 Pulse evolutions in fiber lasers

Pulse generation in this thesis is mainly focused on mode-locking technique for pulses in the picosecond and femtosecond range [7]. There are other pulse generation methods as well, such as gain switching, cavity dumping, Q-switching, but these typically produce pulses with nanosecond durations.

Mode-locking, in frequency domain, can be understood as locking of the phases of different longitudinal modes in the cavity. In time domain, it is a pulsed mode

operation of the laser, as opposed to the continuous-wave (CW) operation. The separation between the pulses is the round trip time. Mode-locking can be realized in two ways: active and passive mode-locking. Active mode-locking is employed by periodically modulating the cavity loss at a matched frequency of the mode spacing. Usually it is done using acousto-optic, electro-optic modulator or a Mach-Zehnder integrated-optic modulator. Picosecond pulses can be generated, but further downscaling will be limited by the speed of the modulations or electronics. Passive mode-locking can generate pulses with much shorter durations down to femtosecond range. It makes use of the pulse itself to introduce intensity-dependent loss into the cavity using a saturable absorber. It's an element which has higher transmission for higher intensity. Some initial higher background noise in the cavity, after many round trips, will win the competition with other fluctuations and eventually become the circulating pulse in the cavity. This technique is easy to implement and has superior performance over other active mode-locking techniques.

Fiber lasers are great tools and stages for these physical processes to interact with each other and study the nonlinear pulse evolutions when the lasers are mode-locked. With stable mode-locking, the pulse characteristics and pulse evolutions can be very different depending on the elements in the cavity. The rest of this section is to go over the various pulse evolutions discovered in fiber lasers so far. The theories and characteristics of these pulse evolutions not only help to identify the specific regime the laser operates in, but also serve as a guidance to design fiber lasers for different needs.

1.3.1 Soliton lasers

The story of fiber lasers starts with soliton lasers. When the laser is made up of only anomalous dispersion fibers, it can be modeled using the NLSE:

$$\frac{\partial A}{\partial z} = -\frac{i\beta_2}{2}\frac{\partial^2 A}{\partial t^2} + i\gamma|A|^2 A, \tag{1.8}$$

This well-studied equation is integrable and has static solutions called solitons. They have minimal breathing in spectral and temporal domain. These solitons are the result of balance between anomalous GVD and third order nonlinearity modeled by γ, and can be described as:

$$A(t,z) = \sqrt{A}\,\mathrm{sech}\left(\frac{t}{\tau}\right)\exp i\theta z, \tag{1.9}$$

One important relation between the relevant parameters is the soliton area theorem [8]:

$$E\tau = \frac{2|\beta_2|}{\gamma}. \tag{1.10}$$

where τ is the pulse width and E is the pulse energy. For each combination of the values β_2 and γ, we have a family of soliton solutions under the soliton area theorem.

As the solitons traverse in the cavity, they experience perturbations such as gain and loss. Solitons adjust themselves by shedding excessive energy in the form of dispersive waves and these can interfere with the original solitons to exhibit the

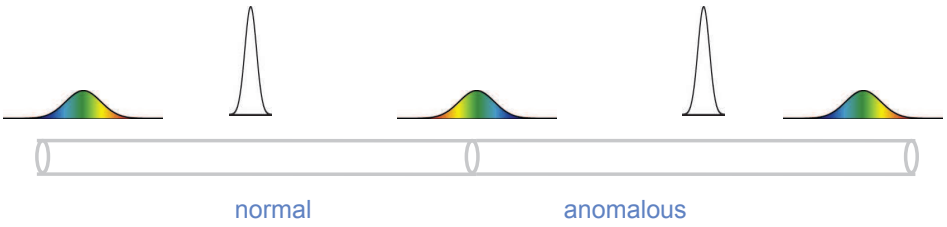

Figure 1.3: Schematic of the dispersion managed soliton design.

characteristic Kelly sidebands [9]. These features on the output spectra are the signature of the soliton mode-locking inside a laser cavity.

However, these Kelly sidebands set the limits on how high the soliton's energy can be. Usually, the pulse energy is limited to 100-pJ level in single mode fiber lasers. The corresponding pulse duration is in the picosecond range. Higher pump power results in the soliton fission and multi-pulsing.

1.3.2 Dispersion-managed soliton lasers

To further improve the pulse energy, a strategy called dispersion management was developed by introducing a dispersion map in the cavity. Here we focus on the net cavity dispersion near 0. One way is to introduce alternating segments of normal and anomalous dispersion fibers [10]. Other methods such as fiber Bragg gratings, telescope grating systems or prisms are also used.

These dispersion-managed (DM) solitons get stretched in the normal dispersion part and get compressed back in the anomalous dispersion fibers, having a large breathing ratio in the time domain, as shown in Figure 1.3. This breathing evolution in temporal domain can reduce the peak power, thus the nonlinear phase accumulation to allow stable pulse energies to increase by an order of magnitude.

The net cavity dispersion can be slightly anomalous or normal. Solutions with the shortest pulse duration exist on the slightly anomalous dispersion side, and the higher energy happens on the net normal side. Up to now, some of the world-record shortest pulse generations from fiber oscillators are still from DM solitons [11, 12, 13].

A more thorough and theoretical summary of dispersion-managed solitons can be found in [14].

1.3.3 Dissipative soliton lasers

Next, we are moving towards the direction of net cavity dispersion being large and normal. A good summary of the pulse evolutions in the normal dispersion regime can be found in [15].

In 2006, dissipative solitons were discovered by Andy Chong and coworkers [2] in an all-normal dispersion fiber laser at 1 μm. They removed the dispersion compensation elements in the cavity and managed to stabilize the highly chirped high-energy solution by introducing a bandpass filter. The output spectra do not share any similar features as previous solutions, but have steep edges and batman ears. This is the result from the balance between normal dispersion, self-focusing nonlinearity, dissipation by spectral filtering and saturable absorption. The equation used to model this is the cubic-quintic Ginzburg-Landau equation (CQGLE) [16, 17]:

$$\frac{\partial A}{\partial z} = gA + \left(\frac{1}{\Omega} - i\frac{D}{2}\right)\frac{\partial^2 A}{\partial t^2} + (\alpha + i\gamma)|A|^2 A + \delta|A|^4 A, \tag{1.11}$$

where g models the gain or loss, D is the 2nd order dispersion, and α and γ together model the property of the SA. The gain filter is introduced by the Ω term and γ is the Kerr nonlinear coefficient.

Without the filter, self-consistent solutions do not exist in a highly chirped fiber cavity. By cutting the pulses in both the temporal and spectral domains, the filter forces the pulses to go back to the starting state and circulate for the next round trip. The chirped pulses are far from the transform limited duration of the spectra and can accumulate large nonlinear phase shift with high energies. These output pulses can be dechirped to close to the transform limited duration by grating pairs.

A good example of the DS soliton laser is shown in Figure 1.2 above. Thus, the resulting peak power can be orders of magnitude higher than the ordinary soliton lasers. Currently, single mode fiber lasers with best performances have been achieved using this evolution with 100-fs duration and 30-nJ pulse energy [18, 6]. These numbers are starting to compete with those from the Ti:sapphire lasers on the market.

Further studies continue to reveal the properties of the DS solutions, such as the DS-version of the soliton area theorem [5], giant chirped oscillator [19], Raman dissipative solitons [20], etc.

1.3.4 Passive self-similar lasers

Even with the normal-dispersion operation of fiber lasers, the excessive nonlinear phase accumulation imposes the ultimate limit on the highest achievable pulse energies. Under the interplay of dispersion and nonlinearity in fibers, pulses undergo the process called wave breaking [21], where they develop side lobes on the spectra

and oscillations on the pulse wings. They can not be de-chirped close to transform limited durations any more. Then the idea of the wave-breaking-free pulses was put forward [22], which share parabolic intensity profiles and linear chirps in the time domain.

These are the wave-breaking-free solutions of the NLSE with normal dispersion in the high intensity regime. Along further propagation, pulses maintain their parabolic shapes and propagate self-similarly without any distortion and wave-breaking. This form-invariant propagation is the origin and the meaning of the word self-similar and sometimes these pulses are called similaritons.

These pulses share the temporal profile in the following analytical form:

$$A^2(0,t) = A_0^2\left(1 - \left(\frac{t}{\tau}\right)^2\right), t \leq \tau \tag{1.12}$$

After conducting the Fourier transform of the parabolic profile in the time domain, we can find it's also a parabola in the frequency domain. It then took a decade until the first self-similar laser was developed by Ilday *et al.* [23]. The main component of the laser is the dispersion map, formed by the normal dispersion fiber and a dispersive delay line (DDL), without any extra introduced spectral filters. The pulse evolution is defined by the dispersion map with minimal spectral evolution. The pulse duration increases in the normal dispersion fiber segment and gets compressed in the DDL. The temporal breathing ratio can be as high as 10$\sim$50. The output chirped pulse has a parabolic shape before the DDL and can be de-chirped close to the transform limited duration using a grating pair outside the cavity.

In contrast with the self-similar evolution in the gain fiber, which admits a local

nonlinear attractor, this pulse shaping process is based on the whole cavity. The pulses have minimal spectral evolution and the DDL is primarily responsible for returning the chirped pulses to their original pulse durations in the cavity. These are the asymptotic solutions of the NLSE with only nonlinearity and normal GVD, without any gain term. With the features of the pulses propagating in the time domain and to differentiate it from the amplifier similariton lasers, we call them passive self-similar lasers. The maximum pulse energy achievable using dissipative soliton lasers and passive self-similar lasers are comparable.

1.3.5 Amplifier similariton lasers

The asymptotic solution of the NLSE with normal dispersion and constant gain term without bandwidth limit [24]:

$$\frac{\partial A}{\partial z} = -\frac{i\beta_2}{2}\frac{\partial^2 A}{\partial t^2} + i\gamma|A|^2 A + \frac{g}{2}A, \tag{1.13}$$

also has the property of propagating self-similarly in the gain fiber. Distinct from the above passive self-similar solutions, these are the local nonlinear attractors in the gain fiber, called amplifier similaritons. Any input arbitrary pulses for the gain fiber eventually converge to the parabola-shaped solutions and scale self-similarly along propagation. The features of the asymptotic solution depends solely on the input pulse energy E and the gain fiber parameters with the form:

$$A(z,t) = A_0(z)\sqrt{\left(1-\left(\frac{t}{\tau(z)}\right)^2\right)}e^{i\phi(z,t)}, t \leq \tau \tag{1.14}$$

The pulse phase $\phi(z,t)$ and pulse chirp $\delta\omega(t)$ have the form of:

$$\phi(z,t) = \phi_0 + 3\gamma\left(\frac{1}{2g}\right)A_0^2(z) - g\left(\frac{1}{6\beta_2}\right)t^2, \tag{1.15}$$

$$\delta\omega(t) = \frac{-\partial\phi(z,t)}{\partial t} = g\left(\frac{1}{3\beta_2}\right)t, \tag{1.16}$$

The pulse amplitude $A_0(z)$ and duration $\tau(z)$ scale as $\exp(gz/3)$, where g is the constant gain coefficient. The exponential growth of the bandwidth will eventually be limited by the gain bandwidth.

The stabilization of the amplifier similariton solution inside a laser cavity was realized around the same time by 3 groups of people. Oktem *et al.* [25] make use of the anomalous dispersion fiber to transform the pulses after the gain fiber into solitons, which are also nonlinear attractors, and prepare them as the seed input for the gain fiber. Aguergaray *et al.* [26] rely on a km-long Raman gain fiber to provide enough propagation length for the input pulses to reach the asymptotic solution. Renninger *et al.* [27] conceive the idea of employing a narrow filter to stabilize the amplifier similariton in an all-normal-dispersion fiber laser without dispersion compensation.

The attractive feature of the amplifier similariton is that it's a local nonlinear attractor, which allows the manipulation of other parts of the cavity. For example, the net cavity dispersion can be changed by introducing dispersion compensation outside the gain fiber, without disturbing the nonlinear attractor in the gain fiber, as long as the proper seed pulse is provided [28]. In contrast, passive self-similar solutions are defined by the average cavity parameters in a narrow parameter space. Amplifier similaritons have a large breathing ratio in both temporal and frequency domains, which is different from DS solitons and passive self-similar lasers.

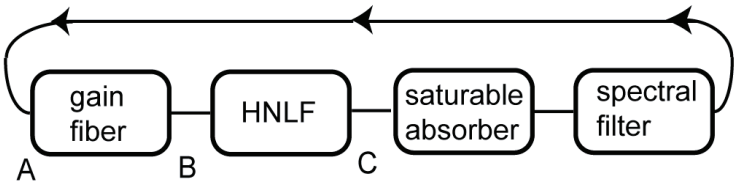

Figure 1.4: The concept of the extended self-similar laser design.

Some of the nice high-energy short pulse generations are based on this evolution, where 40-fs pulses from Yb fiber laser and 70-fs pulses from Er fiber laser are obtained [29, 30]. Generating broader bandwidth using amplifier similaritons are limited by the gain bandwidth [31]. The chirp of the pulses is disrupted and the pulse quality is degraded. Other methods need to be developed to pursue shorter pulse generation beyond the gain bandwidth limits.

1.3.6 Extended self-similar lasers

The conventional way to make shortest pulses from fiber lasers is to operate them with net cavity dispersion near 0, but this method is ultimately limited by the bandwidth of the gain medium. For example, pulses from Yb fiber lasers are limited to durations of 30 fs due to the 40-nm gain bandwidth. And this evolution only generates pulse energies of a fraction of a nanojoule. It requires new wisdom to generate mode-locked spectrum beyond the gain bandwidth limit in fiber lasers.

Chong *et al.* came up with the idea employing amplifier similariton as the local nonlinear attractor to make the significant spectral broadening happen after the gain segment in a highly nonlinear fiber [32]. As long as the pulses can reach the self-similar solutions in the gain fiber, the nonlinear pulse propagation in the passive fiber can be stabilized. These are all possible with the help of the narrow

spectral filter. The linearly chirped parabolic pulses in the amplifier will maintain the parabolic shape and linear chirp in the passive highly nonlinear fiber. This is the reason why this evolution is called extended self-similar. This method demonstrated 1-nJ pulses with 20-fs duration after dechirping at 1 μm, which are the shortest pulses ever generated directly from a Yb fiber oscillator.

1.4 Fiber laser components

This thesis is mainly focused on building up fiber lasers and mode-locking them to obtain ultrashort pulses. A summary of the important components that appear in a fiber laser is necessary. This part is to introduce different kinds of individual components, such as spectral filters and saturable absorbers (SA) in the laser cavity.

1.4.1 Spectral filters

As we have seen in the descriptions of dissipative soliton and amplifier similariton lasers, spectral bandpass filters are the critical and core elements for pulse shaping. They are employed to cut the intra-cavity chirped pulses in spectral and temporal domain, to enable a self-consistent solution in the cavity. In fiber lasers, we mainly use birefringent filters and grating filters, due to their easy implementation and flexibility.

Birefringent filters

Birefringent filters work based on the wavelength-dependent phase shift difference between the ordinary (o-wave) and extraordinary waves (e-wave) in the birefringent plate [33]. When a linearly polarized light is launched into the birefringent plate, it splits into these 2 components. The phase delay difference between them, combined with a second polarizer placed after the birefringent plate will induce a sinusoidal transmission curve with respect to the wavelengths.

When the incident angle of the input light with respect to the principal axis of the material is set to 45 degree, the distribution of the intensity between o-wave and e-wave is the same. Then the transmission function through the birefringent plate is:

$$T = \cos^2\left(\frac{\pi(n_e - n_o)d}{\lambda}\right), \tag{1.17}$$

where n_e and n_o are the refractive indices of the material for e-wave and o-wave. And d is the thickness of the birefringent plate. If quartz is used as the birefringent material, the bandwidths near $\sim$ 10nm can be created in the near infrared color range. An 8-nm bandwidth filter using a 12-T quartz plate has the transmission curve shown in Figure 1.5. Attractive properties of this filter are that it can achieve a modulation depth of 100% and the filter peak positions can be tuned simply by rotating the plates.

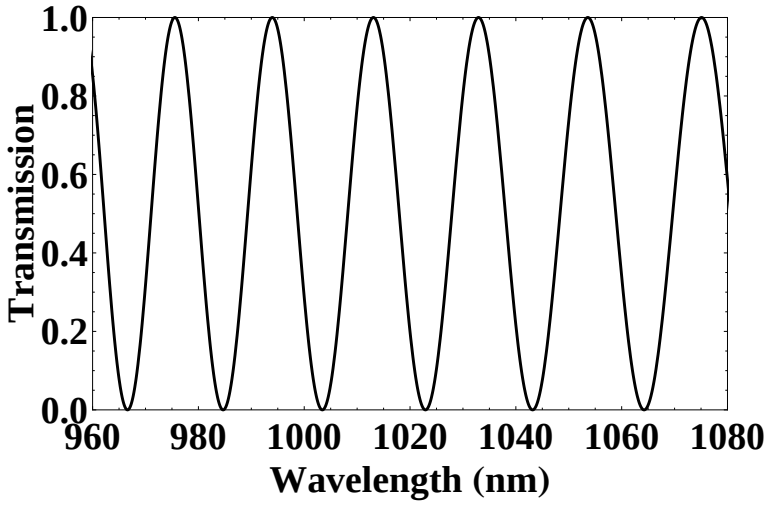

Figure 1.5: Transmission function of a Birefringent filter made of a 12-T (6 mm thick) quartz plate near 1030 nm.

Lyot filters

Lyot filters, invented by Bernard Lyot, also make use of the material birefringence to produce a narrow bandpass filter based on the wavelength-dependent power transmission. However, unlike birefringent filters introduced above, Lyot filters are made up of a sequence of birefringent plates with each plate being half the thickness of the previous one, as shown in Figure 1.6. The light can be considered as containing ordinary and extraordinary polarization components, which respectively experience a different phase delay. The relative phase delay depends on the wavelength, thus making the transmission of optical power at a subsequent polarizer wavelength-dependent.

The key feature of the multiple-plate design is to obtain a sharper/narrower filter with a larger free spectral range. This is particularly useful when it's employed in a gain medium with broad gain bandwidth and to avoid the gain competition between multiple lasing peaks. One illustration of the Lyot filter is shown in Figure 1.7 to produce a 35-nm bandwidth filter at 1900 nm. With more plates introduced

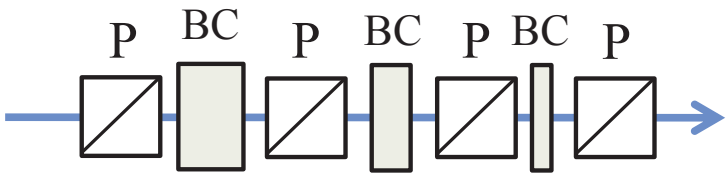

Figure 1.6: A Lyot filter, consisting of a sequence of birefringent crystals (BC) and polarizers (P). Each birefringent plate has the thickness half of the previous one.

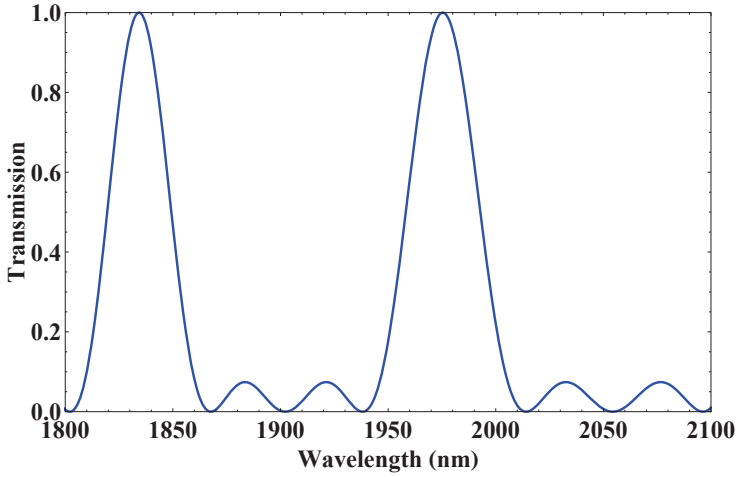

Figure 1.7: Transmission function of a Lyot filter made of a 6 T and 12 T quartz plate near 1900 nm. The bandwidth is 35 nm and the free spectral range is 150 nm.

into the sequence, the filter peaks become sharper.

Grating filters

Grating filter is another option to provide a singly-peaked filter with a nice Gaussian transmission profile due to the Gaussian mode in the single mode fiber. Typically, it's formed by the combination of a fiber-pigtailed collimator and a grating. The spectra of the incident beam is dispersed and spread out by the grating spatially and the acceptance collimator collects only a small portion of the wide beam,

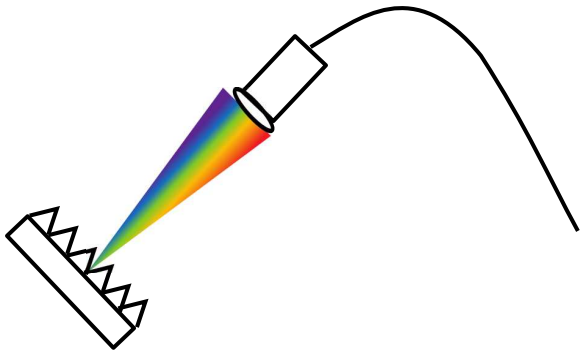

Figure 1.8: Schematic of a grating-based filter.

as shown in Figure 1.8. The bandwidth of the grating filters is usually in the range of a few nanometers and is mainly dependent on the line density of the grating. To gain access to a broader filter bandwidth, one should either employ a grating with lower line density, such as 50 lines/mm, or replace the grating with a much less dispersive element, e.g. a prism. Other factors, such as the beam size, mode field diameter, distance of the collimator to the grating, focal length of the collimator all have influence on the filter transmission profile.

There's one point to be made that grating filters can introduce a large amount of dispersion, which influences pulse evolutions under certain circumstances. Normally, group delay dispersion with a negative sign is introduced and the amount of dispersion increases with the number of lines of the grating used. In Figure 1.9, the 1-nm bandwidth filter at 1030 nm is formed using a 1000 lines/mm grating. The introduced dispersion is $\sim$ -0.1 ps^2, which needs to be taken into consideration.

1.4.2 Saturable absorbers

Saturable absorbers (SA) are elements that provide decreasing loss as the intensity of the incident light increases. This nonlinear feature helps to select and promote

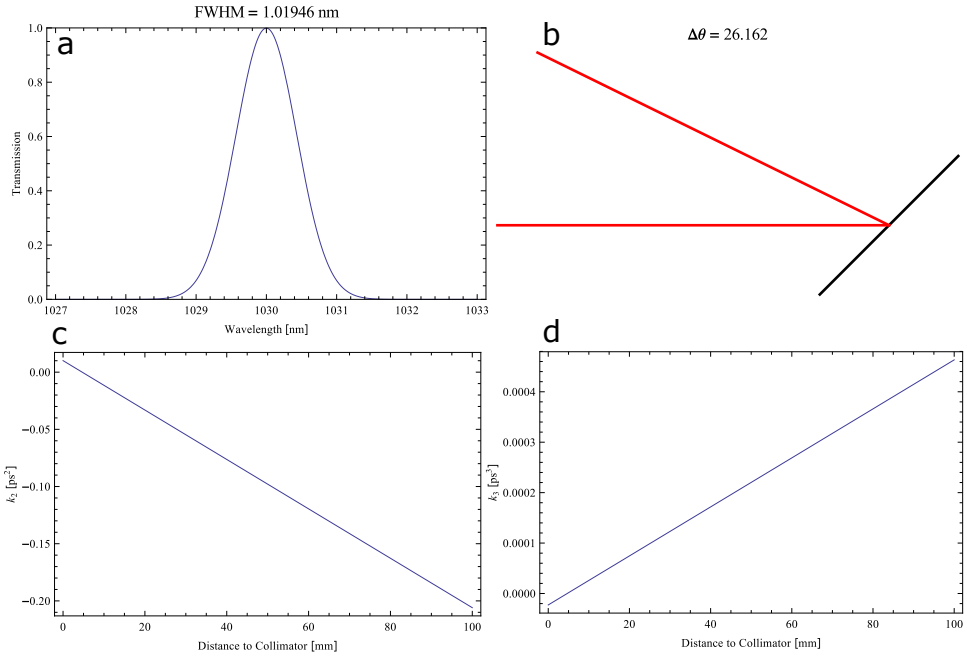

Figure 1.9: A 1-nm bandwidth grating filter at 1030 nm. (a) The transmission profile of the filter; (b) The incident and diffracted angle of the beam; The dependence of the introduced (c) 2nd order and (d) 3rd order dispersion on distance between the collimator and the grating.

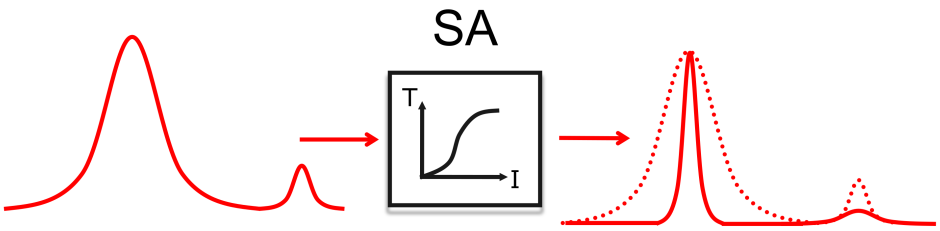

Figure 1.10: Illustration of saturable absorbers promoting pulse generation.

some slightly higher intensity fluctuations initially out of the noise background and gradually build them up into mode-locked pulse trains.

There are two categories of saturable absorbers used in lasers, the artificial saturable absorbers and the material-based saturable absorbers. The former ones include Kerr-lens mode-locking [34], nonlinear polarization evolution (NPE) [35, 36], nonlinear optical loop mirror (NOLM). The latter ones include semiconductor

saturable absorber mirrors (SESAM) [37], quantum dots [38], carbon nanotubes [39], and multiple novel materials. Two types of SAs, SESAM and NPE, are discussed below.

Semiconductor saturable absorber mirrors

SESAMs for passive mode-locking were invented by Prof. Ursula Keller for solid state lasers. They are the optical devices based on the semiconductor materials and can control the magnitude and phase of the optical absorption and reflection at different wavelengths. The optical characteristics of the modulation depth, saturation fluence, and non-saturable loss are key parameters for laser mode-locking.

In case of slow response time from SESAM relative to the pulse durations, the dynamics of SESAM can be complex and needs to be modeled through:

$$\frac{\partial l}{\partial t} = -\frac{l - \Delta R}{\tau_{res}} - \frac{|A|^2}{E_{sat}} l, \tag{1.18}$$

where l is the time-dependent saturable loss, ΔR is the saturable loss or modulation depth, τ_{res} is the response time, and E_{sat} is the saturation fluence of the SESAM.

SESAMs have the advantage of being environmentally stable for self-starting mode-locked lasers. However, they are prone to damage at high power operations, and they typical have low modulation depth of $\sim 10\%$. These impede their use in the high power fiber lasers.

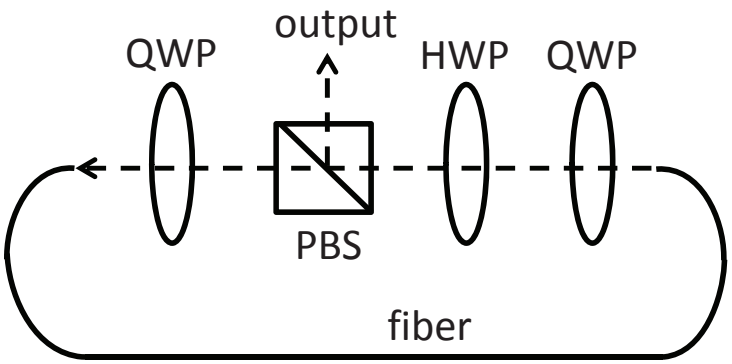

Figure 1.11: Illustration of NPE saturable absorber (PBS: polarizing beam splitter; QWP: quarter waveplate; HWP: half waveplate).

Nonlinear polarization evolution

Nonlinear polarization evolution (NPE) [40] is the artificial SA of choice for lasers in this thesis. It is highly tunable with ultrafast response time and deep modulation depth. It works by converting the nonlinear polarization rotation of light in fibers to amplitude modulation via polarization-dependent loss.

As shown in Figure 1.11, NPE is implemented by 1 polarizer beam spitter (PBS) and 3 waveplates, including two quarter waveplate (QWP) and one half waveplate (HWP). The linearly polarized light after the PBS is set to elliptically polarized light by the quarter waveplate, then launched into the fiber. Self-phase modulation and cross-phase modulation of the two orthogonally polarization ellipse produce intensity-dependent phase shifts. After the fiber, a half waveplate and a quarter waveplate set the polarization back to linear and try to match the axis to the second polarizer. Intensity-dependent loss is induced through the intensity-dependent rotation of the polarization plane. The PBS usually serves as the output port as well.

The transmission curve was derived in [41]. If the angles between the principle

axis of the polarizer with QWP, QWP and HWP are α_1, α_2 and β_1, the normalized output intensity after the second polarizer is:

$$I = \frac{1}{2}(1 - sin(2\alpha_1)sin(2\alpha_2) + cos(2\alpha_1)cos(2\alpha_2)cos(2(\alpha_1 + \alpha_2 - 2\beta_1 + \Delta\phi))) \quad (1.19)$$

It depends on the intensity through the term $\Delta\phi$, which is the rotation angle of the polarization in the Kerr medium (fiber). By changing the angles of the waveplates to certain positions, the transmission of the NPE will act as a SA. The drawback of the NPE is the lack of environmental stability. The retardation of the waveplates depends on the ambient temperature and the polarization rotation is changed if the fiber segment is touched or moved. Under these circumstances, the operating state of SA will be changed and the laser may lose its mode-locking state.

BIBLIOGRAPHY

[1] D. E. Spence, P. N. Kean, and W. Sibbett, **16**, 42 (1991).

[2] A. Chong, J. Buckley, W. Renninger, and F. Wise, Opt. Express **14**, 10095 (2006).

[3] G. P. Agrawal, *Nonlinear fiber optics* (Academic press, ADDRESS, 2007).

[4] K. Blow and D. Wood, IEEE J. Quantum Electron. **25**, 2665 (1989).

[5] W. H. Renninger, A. Chong, and F. W. Wise, **27**, 1978 (2010).

[6] A. Chong, W. H. Renninger, and F. W. Wise, Opt. Lett. **32**, 2408 (2007).

[7] H. A. Haus, IEEE J. Sel. Top. Quantum Electron. **6**, 1173 (2000).

[8] L. E. Nelson, D. J. Jones, K. Tamura, H. A. Haus, and E. P. Ippen, Appl. Phys. B **65**, 277 (1997).

[9] S. Kelly, Electron. Lett. **28**, 806 (1992).

[10] K. Tamura, E. P. Ippen, H. a. Haus, and L. E. Nelson, Opt. Lett. **18**, 1080 (1993).

[11] D. Ma, Y. Cai, C. Zhou, W. Zong, L. Chen, and Z. Zhang, Opt. Lett. **35**, 2858 (2010).

[12] X. Zhou, D. Yoshitomi, Y. Kobayashi, and K. Torizuka, Opt. Express **16**, 7055 (2008).

[13] Y. Nomura and T. Fuji, Opt. Express **22**, 12461 (2014).

[14] S. K. Turitsyn, B. G. Bale, and M. P. Fedoruk, Phys. Rep. **521**, 135 (2012).

[15] F. Wise, A. Chong, and W. Renninger, Laser Photonics Rev. **2**, 58 (2008).

[16] W. Renninger, A. Chong, and F. Wise, Phys. Rev. A **77**, 023814 (2008).

[17] P. Grelu, S. Chouli, J. M. Soto-Crespo, W. Chang, A. Ankiewicz, and N. Akhmediev, 2010 Photonics Glob. Conf. PGC 2010 **6**, 84 (2010).

[18] K. Kieu, W. H. Renninger, A. Chong, and F. W. Wise, Opt. Lett. **34**, 593 (2009).

[19] W. H. Renninger, A. Chong, and F. W. Wise, Opt. Lett. **33**, 3025 (2008).

[20] D. S. Kharenko, A. E. Bednyakova, E. V. Podivilov, M. P. Fedoruk, A. Apolonski, and S. A. Babin, Opt. Express **23**, 1857 (2015).

[21] D. Anderson, M. Desaix, M. Lisak, and M. L. Quiroga-Teixeiro, J. Opt. Soc. Am. B **9**, 1358 (1992).

[22] D. Anderson, M. Desaix, M. Karlsson, M. Lisak, and M. L. Quiroga-Teixeiro, J. Opt. Soc. Am. B **95**, 4869 (1993).

[23] F. Ilday, J. Buckley, W. Clark, and F. Wise, Phys. Rev. Lett. **92**, 213902 (2004).

[24] M. Fermann, V. Kruglov, B. Thomsen, J. Dudley, and J. Harvey, Phys. Rev. Lett. **84**, 6010 (2000).

[25] B. Oktem, C. Ülgüdür, and F. Ö. Ilday, Nat. Photonics **4**, 307 (2010).

[26] C. Aguergaray, D. Méchin, V. Kruglov, and J. D. Harvey, Opt. Express **18**, 8680 (2010).

[27] W. H. Renninger, A. Chong, and F. W. Wise, Phys. Rev. A **82**, 021805 (2010).

[28] W. H. Renninger, A. Chong, and F. W. Wise, Opt. Express **19**, 1 (2011).

[29] B. Nie, D. Pestov, F. W. Wise, and M. Dantus, Opt. Express **19**, 12074 (2011).

[30] H. Liu, Z. Liu, E. S. Lamb, and F. Wise, Opt. Lett. **39**, 1019 (2014).

[31] D. Soh, J. Nilsson, and A. Grudinin, J. Opt. Soc. Am. B **23**, 10 (2006).

[32] A. Chong, H. Liu, B. Nie, B. G. Bale, S. Wabnitz, W. H. Renninger, M. Dantus, and F. W. Wise, Opt. Express **20**, 14213 (2012).

[33] J. W. Evans, J. Opt. Soc. Am. **39**, 229 (1949).

[34] T. Brabec, C. Spielmann, P. F. Curley, and F. Krausz, Opt. Lett. **17**, 1292 (1992).

[35] M. E. Fermann, Opt. Lett. **18**, 894 (1993).

[36] R. H. Stolen, J. Botineau, and A. Ashkin, Opt. Lett. **7**, 512 (1982).

[37] U. Keller, K. J. Weingarten, F. X. Kärtner, D. Kopf, B. Braun, I. D. Jung, R. Fluck, C. Hönninger, N. Matuschek, and J. Aus Der Au, IEEE J. Sel. Top. Quantum Electron. **2**, 435 (1996).

[38] M. A. C. &. W. S. E. U. Rafailov, Nat. Photonics **1**, 395 (2007).

[39] S. Y. Set, H. Yaguchi, Y. Tanaka, and M. Jablonski, J. Light. Technol. **22**, 51 (2004).

[40] H. A. Haus, E. P. Ippen, and K. Tamura, IEEE J. Quantum Electron. **30**, 200 (1994).

[41] C. Y. Chong, Thesis (Ph.D.)–Cornell Univ. (2008).

CHAPTER 2

SELF-SIMILAR PULSE EVOLUTION IN A FIBER LASER WITH COMB-LIKE DISPERSION DECREASING FIBER[1]

Here we demonstrate an erbium fiber laser with self-similar pulse evolution inside a comb-like dispersion-decreasing fiber. We show numerically and experimentally that the comb-like dispersion-decreasing fiber works as well as an ideal one, and offers major practical advantages. The existence of a nonlinear attractor is verified by the invariant pulse chirp over a wide range of net cavity dispersion in experiments. The laser generates 1.3-nJ pulses with parabolic shape and linear chirp, which can be dechirped to 37 fs. Comb-like dispersion-decreasing fiber should enable the generation of high energy few-cycle pulses directly from a fiber oscillator.

2.1 Introduction

Lasers with few-cycle pulse durations are attractive for applications in frequency combs, high-harmonic generation, and ultrafast spectroscopy, among others. The few-cycle regime in the near infrared region is currently dominated by solid-state lasers, such as Ti:sapphire, Cr:forsterite and Cr:YAG [2], due to their broad gain bandwidths. Fiber lasers have started to compete with solid state lasers in terms of pulse energy and average power, but they still lag behind in obtaining high energy few-cycle pulses directly from an oscillator. Ultimately, mode-locked fiber lasers that generate octave-spanning spectra and few-cycle pulses will be very attractive for applications.

[1]Much of the work presented in this chapter was published in Optics Letters [1].

Ultrashort pulses are obtained routinely from fiber lasers with cavity dispersion close to zero [3], but the pulse energy is limited. Sub-30 fs pulses were obtained from Yb fiber lasers with pulse energies up to 0.7 nJ [4, 5], which corresponds to nonlinear phase shifts up to π. To obtain high-energy ultrashort pulses, pulse evolutions that can tolerate large nonlinear phase are desirable. Self-similar pulse evolution [6, 7, 8] has allowed the generation of 10-nJ and 42-fs pulses at 1030 nm [9]. However, the gain bandwidth limitation has to be circumvented to reach the few-cycle pulse regime.

Chong *et al.* [10] made use of the nonlinear attractor in the gain fiber and extended self-similar evolution in a highly-nonlinear passive fiber to obtain 20-fs pulses. However, the pulse accumulated a complex phase, and multiphoton intrapulse interference phase scan was required to dechirp the pulse. Dispersion-decreasing fiber (DDF) with normal dispersion is formally equivalent to a gain fiber and it supports self-similar pulse evolution, but without any bandwidth limitation [11]. Liu and coworkers [12] exploited extended self-similar evolution in a DDF made of tapered photonic crystal fiber to obtain 6-cycle pulses at 1 μm, dechirped with a standard grating pair. However, the fabrication of DDF is difficult [13]. Recently, aspects of self-similar pulse evolutions have been demonstrated in passive comb-like DDF by Kibler *et al.* [14] and Méchin *et al.* [15]. It was demonstrated [14] that an ideal DDF with a hyperbolic dispersion profile can be approximated by alternating segments of two ordinary fibers with different dispersion values (Figure 2.1). This so-called comb-like fiber offers a simple, engineerable, and practical alternative to a real DDF [16].

2.2 Er fiber laser with comb-like dispersion-decreasing fiber

Ultrashort pulse generation in erbium (Er) fiber lasers has followed a similar development path. Sub-45 fs pulses at 1550 nm were obtained based on dispersion management [17, 18, 19] with pulse energies below 0.5 nJ. Sub-50 fs pulses were generated, but with a long pedestal expanding over 800 fs, which indicates uncontrolled nonlinear phase [20]. Self-similar pulse evolution has been employed to generate 3.5-nJ and 70-fs pulses [21]. A single-cycle light source was realized by coherently combining two continuua driven by the same fiber laser [22]. Despite the significant progress people have made at this important wavelength, the generation of few-cycle pulses with nanojoule-level energy directly from an oscillator remains a challenge.

Here we demonstrate an Er fiber laser with self-similar evolution in a comb-like DDF in the cavity. Numerical simulations show that the pulse evolution and performance with the comb-like DDF are very similar to those that would be obtained with a real DDF. The nonlinear attractor is studied by varying the cavity dispersion over a large range, and confirmed by the invariant chirp on the output pulses. The experimental results agree well with numerical simulations. The laser generates 1.3-nJ pulses with a parabolic shape and linear chirp. These can be dechirped to 37 fs duration, which corresponds to 7 optical cycles. The pulse energy is a 4-fold improvement over previous Er fiber lasers with comparable pulse duration. Factors that limit the laser performance are discussed.

2.2.1 Modeling

Pulse propagation inside an ideal DDF is governed by a nonlinear Schrödinger equation with the group velocity dispersion (GVD) varying with the propagation distance z according to Eq. 2.1 [11]. The dispersion decreasing rate is given by Γ, and β_{20} denotes the GVD at $z = 0$.

$$\beta_2(z) = \frac{\beta_{20}}{1 + \Gamma z} \tag{2.1}$$

The full-width-half-maximum bandwidth of the asymptotic self-similar solution can be calculated using the method of steepest descent [23]:

$$\Delta\lambda = \sqrt{2}\frac{{\lambda_c}^2}{2\pi c}\left(\frac{E_{in}\gamma\Gamma}{2\beta_{20}^2}\right)^{1/3}(1 + \Gamma z)^{1/3} \tag{2.2}$$

where λ_c is the center wavelength of the pulse, c is the speed of light, E_{in} is the input pulse energy to the DDF, and γ is the fiber nonlinearity coefficient. Evaluation of the spectral bandwidth at the end of the DDF yields:

$$\Delta\lambda \propto \left(\frac{E_{in}\Gamma}{A_{eff}\beta_{20}\beta_2}\right)^{1/3} \tag{2.3}$$

where β_2 is the GVD at the end of the DDF and A_{eff} is the effective mode area, assumed to be constant along the fiber. A DDF optimized to obtain the broadest spectra should have small core area, low dispersion on both fiber ends, and a large-dispersion decreasing rate. In addition, the loss in the cavity should be kept small to maximize the input energy.

We use Eq. 2.3 as a figure of merit to choose the fibers to form the comb-like

DDF. It is desirable for one fiber to have dispersion as close to zero as possible, which led us to choose PWG1-XP (Nufern). The choice of the second fiber is a trade-off between minimizing β_{20} and maximizing Γ. Among commercially-available fibers, UHNA7 (Nufern) offers the largest bandwidth. The total length of DDF is chosen to be 1 m, to avoid the overdriving of nonlinear polarization evolution (NPE). We take the minimum segment length to be 5 cm, considering practical issues such as splicing. To find the optimum segment lengths, a simplex algorithm [24] was used to fit the comb-like DDF to an ideal hyperbolic DDF with the same initial and final dispersion, and constant fiber nonlinearity. We started with 2 segments in optimization and stopped at 6 segments, where the results are similar to an ideal DDF. The fitting result is shown in Figure 2.1. Use of the soliton number $N^2 \propto \frac{1}{A_{eff}\beta_2}$ to include the differences in nonlinearity of the fibers produces similar results for the optimum segment lengths. The dispersion profiles of an ideal DDF at 1400 nm and 1700 nm are shown to illustrate the dispersion variation across the expected spectral range. The large and negative third-order dispersion (TOD) of UNHA7 helps compensate the TOD of the cavity.

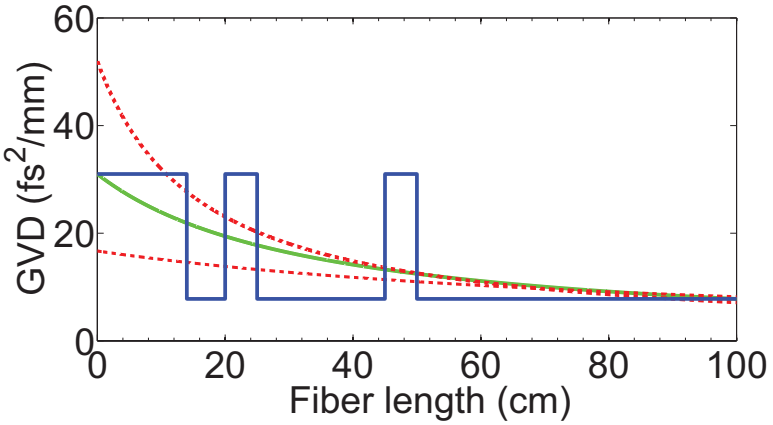

Figure 2.1: Comparison of the GVD values of the ideal DDF (green) with the comb-like DDF (blue) at 1550 nm. The lengths of the segments are 14, 6, 5, 20, 5 and 50 cm. The upper and lower red dashed lines are for the ideal DDF at 1700 and 1400 nm, respectively.

Numerical simulations are conducted assuming the laser setup of Figure 2.2 (a) and using appropriate terms of the generalized nonlinear Schrödinger equation for each segment, including stimulated Raman scattering and self-steepening. Values of the fiber parameters are listed in Table 2.1. A relatively-short (1 m) gain fiber is chosen for two reasons: we do not want the pulse to be stretched too much before entering the DDF, and we do not want the pulse to reach the asymptotic self-similar form in the gain medium. Instead, we rely on the nonlinear attractor in the DDF to stabilize the pulse evolution. The gain segment is modeled with 30-dB small signal gain, a 40-nm Gaussian gain spectrum centered at 1550 nm, and a saturation energy of 10 nJ. Normal-dispersion fibers (NDF) are inserted to reduce the repetition rate to 10∼20 MHz. Other fiber segments are 0.5 m of SMF28e and 0.5 m of OFS980 as the pigtails of the collimators and wavelength-division multiplexers, respectively. A 5-nm bandwidth Gaussian filter with peak transmission of 50% is assumed. It introduces dispersion of -0.11 ps^2 due to the combination of the grating and collimator. The output coupling ratio is 70%, while the linear cavity loss is 60% to reflect the collimator pair coupling efficiency. A lumped saturable absorber is modeled with modulation depth of 100% and saturation power of 2 kW.

Table 2.1: Values of Parameters Used in Simulation

Fiber Name	Aeff (μm^2)	GVD (fs^2/mm)	TOD (fs^3/mm)
UHNA7	7.6	31	-153
PWG1-XP	18	7.8	1.1
Er110	29	15	50
OFS980	44	4.5	109
NDF	48	3.8	83
SMF28e	85	-23	86

Simulations converge over a large range of parameters, and typical solutions are shown in Figure 2.2. The comb-like DDF functions similarly to the ideal one, as

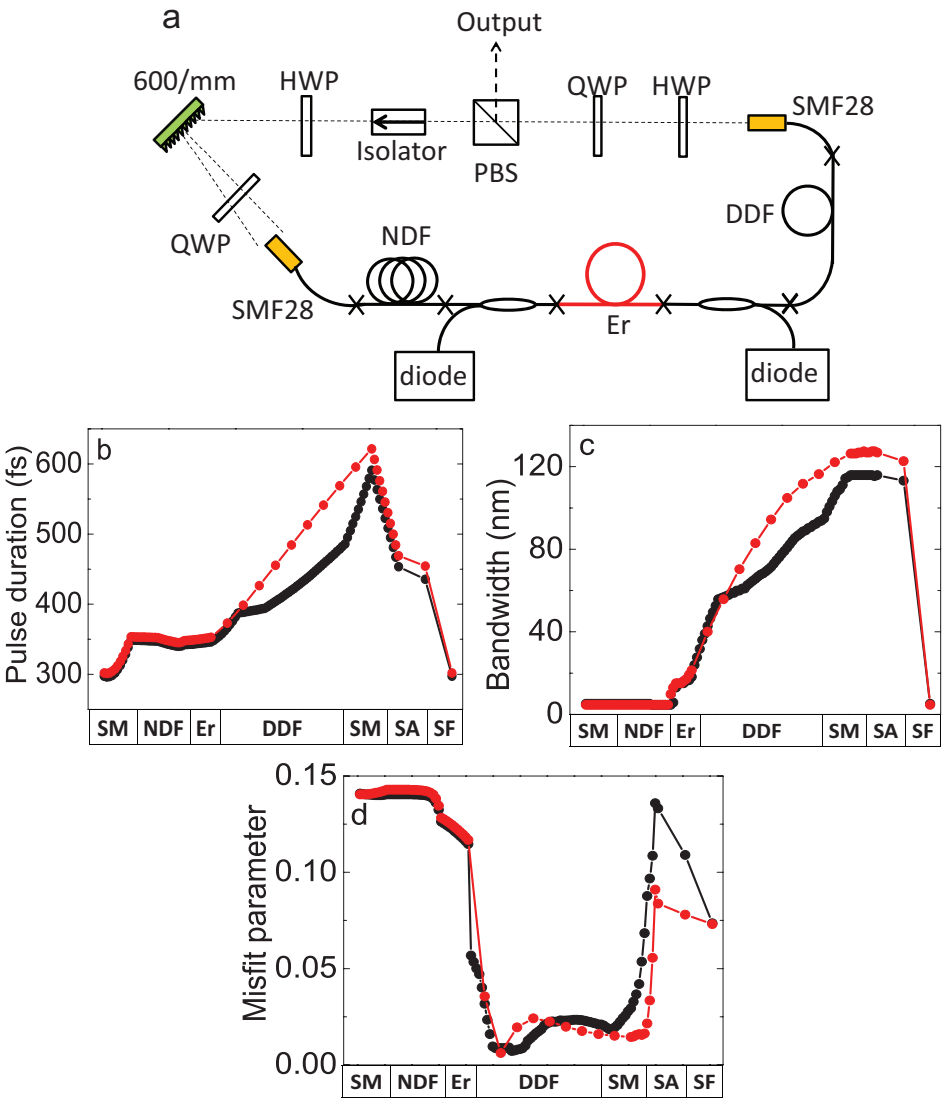

Figure 2.2: (a) Schematic of the Er DDF laser: PBS: polarizing beam splitter; QWP: quarter-wave plate; HWP: half-wave plate. (b)-(d) Simulation results for an ideal (red) or a comb-like DDF (black), with net cavity dispersion of -0.087 ps^2. (b) Evolution of pulse duration (SA, saturable absorber; SF, spectral filter). (c) Evolution of spectral bandwidth. (d) Evolution of misfit parameter.

they match well in both spectral and temporal pulse evolution. Pulse propagation is mainly defined by the 5-nm filter and the DDF segment. The spectral breathing ratio can be as large as 25, with bandwidth around 120 nm after the DDF segment. The pulse duration increases monotonically in the DDF, until the pulse is compressed by the anomalous-dispersion pigtail and cut by the narrow filter. To

get further insight into the pulse-shaping process, we employ the misfit parameter M, which is the root-mean-square deviation of the pulse intensity profile from a parabolic pulse of the same energy. Due to the presence of intermediate-asymptotic wings around the parabolic pulse core [25], we calculate the M parameter based on the central portion of the pulse, which contains 95% of the pulse energy (Figure 2.2 (d)). The pulse is primarily attracted to the self-similar solution in the DDF, with a small contribution from the gain fiber. The M parameter decreases sharply in the initial stage of the DDF and remains close to zero. The parabolic shape is maintained upon further propagation inside the SMF until the spectrum is cut by the filter.

2.2.2 Experiments

We built a laser as in Figure 2.2(a) with a comb-like DDF by simply splicing six segments of fiber together. Total loss of 0.25 dB is introduced by the comb-like structure. NPE is implemented with the wave plates and a polarizing beam splitter, which also serves as the output port. A half-wave plate in front of the grating is used to optimize the transmission efficiency. Typically, mode-locking with multi-pulsing is initiated at a pump power of 1 W by rotating the waveplates, and a single-pulsing state is obtained by decreasing the pump power to 500 mW. Single-pulsing is confirmed with an autocorrelator with 180-ps scan range and a fast detector with 30-ps rise time.

A representative set of experimental results is shown in Figure 2.3. The cross-correlation of the output pulse and the dechirped pulse fits a parabola well, which is evidence of the self-similar pulse shaping. Output pulses with 1.3-nJ energy and spectral bandwidth of 240 nm at the -20-dB level are obtained, in good agree-

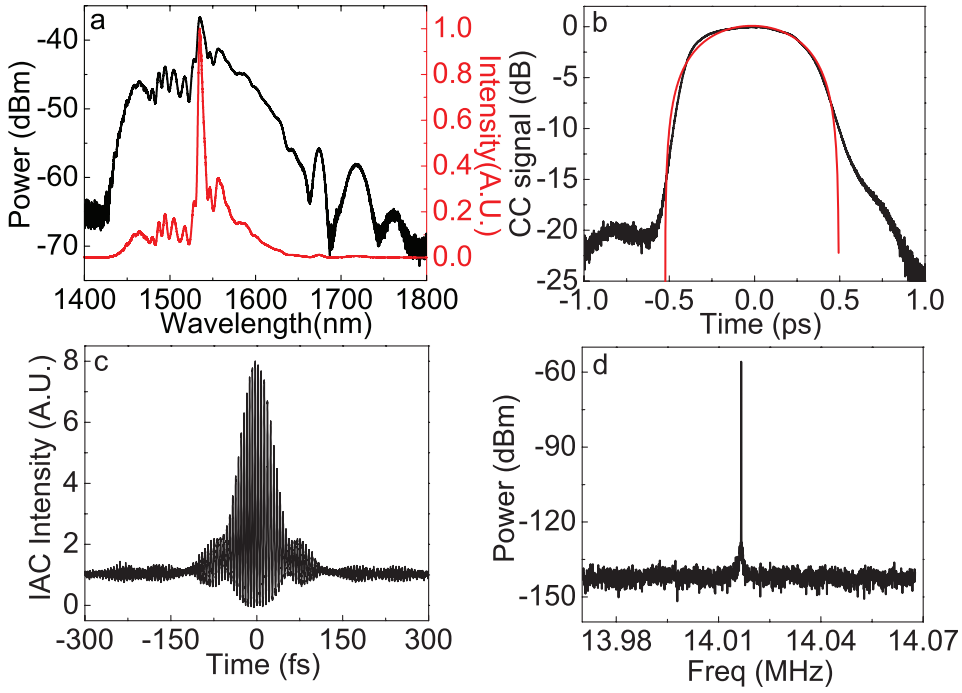

Figure 2.3: (a) Measured mode-locked spectrum of the Er DDF laser. (b) Fitting of the cross correlation signal to a parabola. (c) Interferometric autocorrelation of the dechirped pulse using two-photon absorption. (d) Radio frequency spectrum of the mode-locked laser with resolution bandwidth of 10 Hz and span range of 100 kHz.

ment with the simulations. The pulses can be dechirped with a prism pair to 37 fs, within 10% of the transform limit of 34 fs. The pulse energy is a 4-fold improvement compared with Er fiber lasers that have reached this pulse duration. The radio-frequency spectrum exhibits a contrast ratio over 85 dB, which confirms stable mode-locking. The pulse quality was verified by launching the dechirped pulses into a segment of PWG1-XP fiber. The observed spectral broadening in Figure 2.4 agrees reasonably with results of numerical simulations and confirms the approximately 30 kW peak power.

To demonstrate the nonlinear attractor in the DDF, the net cavity dispersion was varied by inserting normal-dispersion fiber into the laser cavity. Mode-locking is observed with net dispersion ranging from -0.1 ps^2 to 0.3 ps^2, at which point other

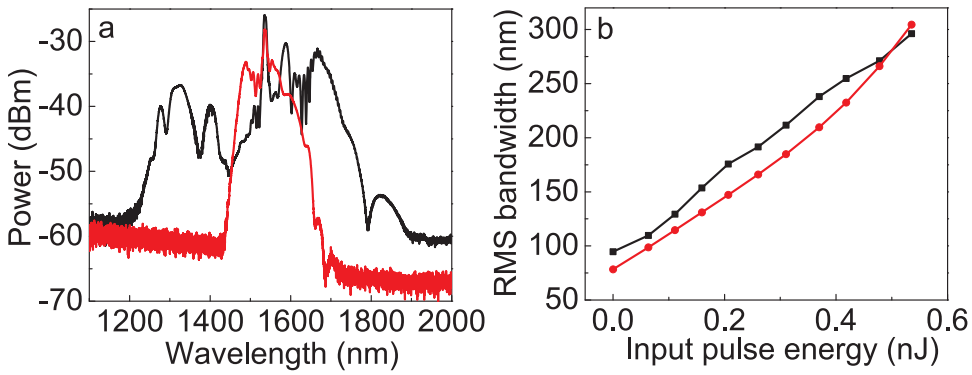

Figure 2.4: (a) The pulse spectrum at the input and output end of the peak power testing segment with coupled-in energy of 0.54 nJ. (b) Comparison of the spectral broadening in experiments (in black) and simulations (Gaussian pulses; in red) at different input energy level.

states that resemble dissipative solitons start to appear. The pulse performance is summarized in Figure 2.5. Over a large dispersion range, the pulse chirp is always much smaller than, and relatively independent of the cavity dispersion. This is a strong indication of the existence of a nonlinear attractor [26] in the DDF segment. The chirp of the asymptotic solution is determined only by the parameters of the DDF. The deviation of the dechirped pulse duration from the transform limit is always less than 10%, as expected for a parabolic pulse with linear chirp.

2.2.3 Discussion

The performance achieved in this proof-of-concept demonstration of the piecewise DDF inside a laser is significantly limited by losses in the cavity. The implementation of the filter by a diffraction grating and collimator is very lossy. In simulations, if these losses are reduced from 7 dB to 1 dB, 25-fs pulses with peak power over 200 kW are generated. The use of a fiber Bragg grating filter in an amplifier similariton laser to minimize the loss was recently reported [27], and this approach could be applied to a laser with a DDF. Excessive nonlinear phase accumulation

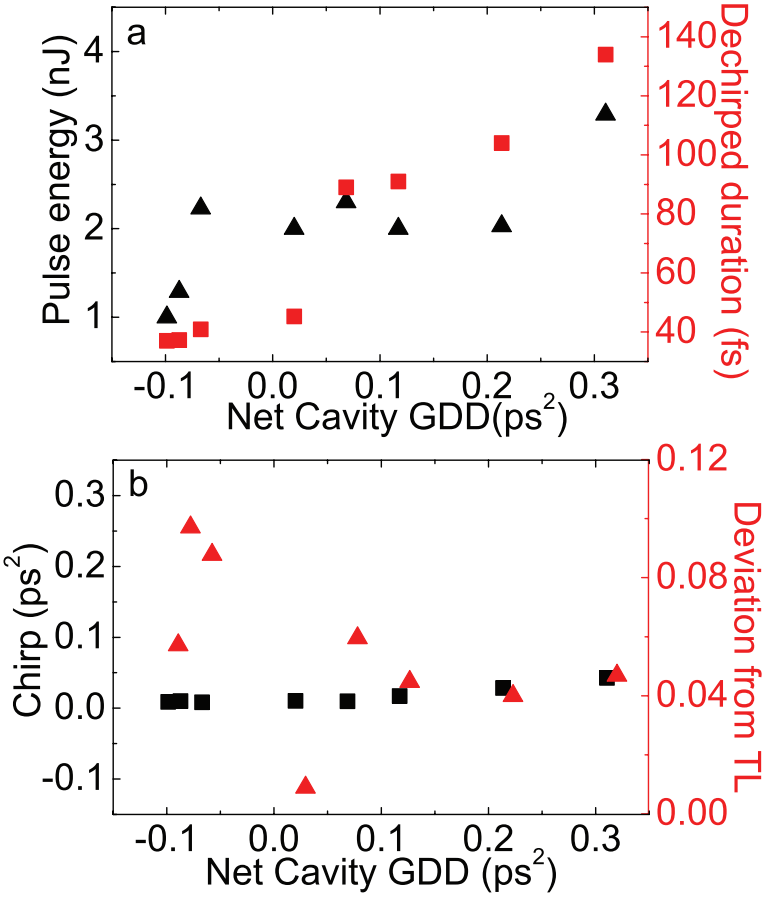

Figure 2.5: (a) Pulse energy and dechirped pulse duration at various cavity dispersions. (b) Pulse chirp and deviation of dechirped pulse duration from the transform limit at various cavity dispersions.

will then limit the performance.

The versatility of the comb-like DDF lies in the fact that we can tailor its properties freely using different combinations of fibers. Limitations of the gain spectrum are obviously eliminated, and it should be possible to mitigate other factors that limit self-similar evolution [28, 29, 30]. Third-order dispersion can be compensated in the fiber segments of the DDF (as is the case in the work here) and stimulated Raman scattering can be managed by using short overall lengths.

2.3 Yb fiber laser with comb-like dispersion-decreasing fiber

This flexible comb-like DDF will be valuable for fiber lasers at other wavelengths as well. For example, it will help with Tm fiber lasers at 2 μm, where it is difficult to design a similariton laser due to the lack of normal-dispersion gain fibers. With this home-made DDF, the formation of a nonlinear attractor inside the passive segment is possible.

Here I want to illustrate the application of comb-like DDF in a Yb fiber laser, although the implementation will be complicated a bit by the need to use microstructure fibers to obtain different dispersions. Considering the intrinsic material dispersions in fibers at 1 μm are $\sim$20 fs^2/mm, it's hard to obtain ordinary fibers with GVD close to 0 to form the DDF structure. Special microstructure fibers from NKT, such as NL-1050-ZERO-2, need to be considered as the low-dispersion fiber to form the comb structure. Employing the Eq. 2.3 as the figure of merit to choose the high-dispersion fiber, UHNA3 stands out as a choice. The parameters of the fibers are shown in Table 2.2.

Table 2.2: Parameters Used in Simulation for Yb DDF laser

Fiber Name	Aeff (μm^2)	GVD (fs^2/mm)	TOD (fs^3/mm)
UHNA3	4.5	60	-102
ZERO-2	3.8	2	0
Yb501	31	23	40
Hi1060	31	23	40
OFS980	14	27.3	57.5

If we assume a 6-segment structure for the DDF, with a total length of 1 m and dispersion deceasing rate of $\Gamma = 0.29/cm$, the fitted lengths are: 2.3 cm, 1 cm,

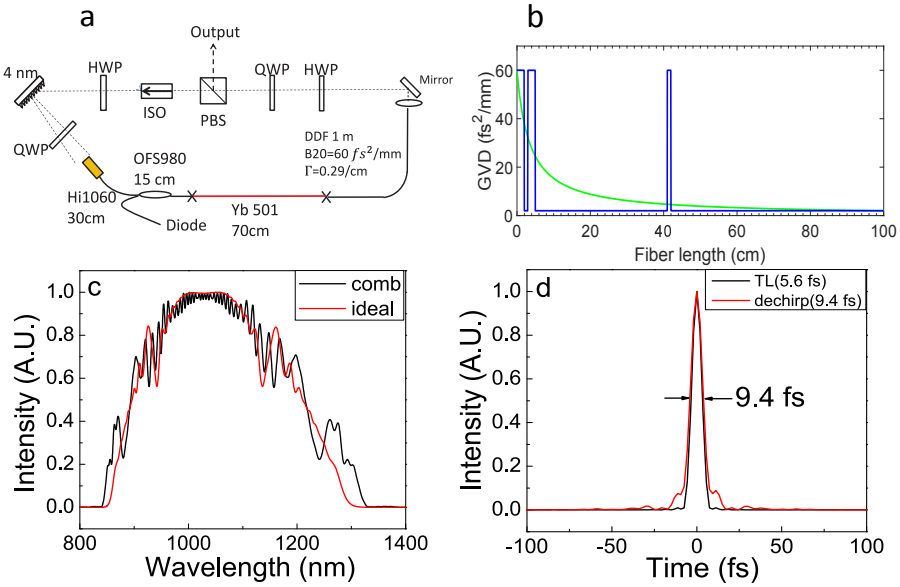

Figure 2.6: (a) Schematic of the Yb DDF laser: PBS: polarizing beam splitter; QWP: quarter-wave plate; HWP: half-wave plate. (b) Comparison of the GVD values of the ideal DDF (green) with the comb-like DDF (blue) at 1030 nm. (c)-(d) Comparison of the output spectra and dechirped pulse (using comb DDF) with transform limit pulse.

1.3 cm, 36 cm, 1 cm, 58 cm for an ideal DDF with $\beta_{20} = 60\ fs^2/mm$. The loss at the filter is set to 0 assuming the employment of a fiber Bragg grating.

In simulations, pulses with 4 nJ energy and transform-limit duration of 5.6 fs are obtained. The pulse evolution in terms of the Misfit parameter and the spectral bandwidth are very similar to the case where the DDF is ideal. The chirp is linearized by the nonlinear attractor inside the DDF and the pulses can be dechirped to 9.4 fs, close to the TL duration. In this cavity, the nonlinear phase is $\sim 80\ \pi$. Further increase of the pulse energy is limited by the nonlinear phase accumulation. But this laser has provided a route to the generation of few-cycle pulses directly from a fiber laser at 1 μm.

2.4 Conclusion

In conclusion, we have demonstrated a fiber laser with self-similar evolution in a comb-like dispersion-decreasing fiber, which works as well as an ideal dispersion-decreasing fiber but is much more practical to realize experimentally. The existence of the nonlinear attractor inside the DDF is experimentally confirmed. The laser generates 1.3-nJ pulses with 7-cycle duration at 1550 nm. This constitutes a 4-fold increase in pulse energy compared to previous reports of this pulse duration. Numerical results show great potential to obtain shorter pulses with much higher energy by minimizing cavity losses.

Portions of this work were supported by the National Science Foundation (ECCS-1306035).

BIBLIOGRAPHY

[1] Y. Tang, Z. Liu, W. Fu, and F. W. Wise, Opt. Lett. **41**, 2290 (2016).

[2] T. R. Schibli, O. Kuzucu, J. W. Kim, E. P. Ippen, J. G. Fujimoto, F. X. Kaertner, V. Scheuer, and G. Angelow, IEEE J. Sel. Top. Quantum Electron. **9**, 990 (2003).

[3] K. Tamura, E. P. Ippen, H. A. Haus, and L. E. Nelson, Opt. Lett. **18**, 1080 (1993).

[4] X. Zhou, D. Yoshitomi, Y. Kobayashi, and K. Torizuka, Opt. Express **16**, 7055 (2008).

[5] T. Kurita, H. Yoshida, T. Kawashima, and N. Miyanaga, Opt. Lett. **37**, 3972 (2012).

[6] F. Ilday, J. Buckley, W. Clark, and F. Wise, Phys. Rev. Lett. **92**, 213902 (2004).

[7] B. Oktem, C. Ülgüdür, and F. Ö. Ilday, Nat. Photonics **4**, 307 (2010).

[8] W. H. Renninger, A. Chong, and F. W. Wise, Phys. Rev. A **82**, 021805 (2010).

[9] B. Nie, D. Pestov, F. W. Wise, and M. Dantus, Opt. Express **19**, 12074 (2011).

[10] A. Chong, H. Liu, B. Nie, B. G. Bale, S. Wabnitz, W. H. Renninger, M. Dantus, and F. W. Wise, Opt. Express **20**, 14213 (2012).

[11] T. Hirooka and M. Nakazawa, Opt. Lett. **29**, 498 (2004).

[12] H. Liu, F. Yu, A. Chong, J. C. Knight, and F. Wise, Lasers Electro-Optics (CLEO), 2013 Conf. CM2I.1 (2013).

[13] U. G. Akhmetshin, V. A. Bogatyrev, A. K. Senatorov, A. A. Sysolyatin, and M. G. Shalygin, Quantum Electron. **33**, 265 (2003).

[14] R. F. B. Kibler, C. Billet, P. A. Lacourt, L. L. Dudley, and J. M., Electron. Lett. **42**, 965 (2006).

[15] D. Méchin, S.-H. Im, V. I. Kruglov, and J. D. Harvey, Opt. Lett. **31**, 2106 (2006).

[16] ALEXEJ A. SYSOLIATIN and D. A. NOLAN, J. Nonlinear Opt. Phys. Mat. **16**, 171 (2007).

[17] D. Ma, Y. Cai, C. Zhou, W. Zong, L. Chen, and Z. Zhang, Opt. Lett. **35**, 2858 (2010).

[18] X. Li, W. Zou, and J. Chen, Opt. Lett. **39**, 1553 (2014).

[19] X. Li, W. Zou, S. Member, G. Yang, and J. Chen, IEEE Photonics Technol. Lett. **27**, 93 (2015).

[20] D. Y. Tang and L. M. Zhao, Opt. Lett. **32**, 41 (2007).

[21] H. Liu, Z. Liu, E. S. Lamb, and F. Wise, Opt. Lett. **39**, 1019 (2014).

[22] G. Krauss, S. Lohss, T. Hanke, A. Sell, S. Eggert, R. Huber, and A. Leitenstorfer, Nat. Photonics **4**, 33 (2010).

[23] W. H. Renninger, Thesis (Ph.D.)–Cornell Univ. (2012).

[24] M. H. W. JEFFREY C. LAGARIAS, JAMES A. REEDS, WRIGHT, and P. E., SIAM J. Optim. **9**, 112 (1998).

[25] C. Billet, J. Dudley, N. Joly, and J. Knight, Opt. Express **13**, 3236 (2005).

[26] W. H. Renninger, A. Chong, and F. W. Wise, Opt. Express **19**, 1 (2011).

[27] Michel Olivier, Mathieu Gagnon, Simon Duval, Martin Bernier and M. Piché, Opt. Lett. **40**, 5650 (2015).

[28] A. B. G. Nilsson, Daniel B. S. Soh and Johan and Fianium, J. Opt. Soc. Am. B **23**, 1 (2006).

[29] D. Soh, J. Nilsson, and A. Grudinin, J. Opt. Soc. Am. B **23**, 10 (2006).

[30] V. I. Kruglov, C. Aguergaray, and J. D. Harvey, Opt. Lett. **35**, 3084 (2010).

CHAPTER 3

HIGH ENERGY PULSES FROM THULIUM FIBER LASERS[1]

3.1 Introduction

Ultrafast laser sources that emit with a wavelength around 2 μm are attracting increasing attention due to their various applications, which include medical treatment, spectroscopy, environmental monitoring, and remote sensing. Among them, fiber lasers that employ thulium-doped or thulium-holmium co-doped fibers stand out for covering the broad range from 1.7 μm to 2.1 μm, with great potential to produce sub-100 femtosecond pulses. The cross-relaxation process in highly-doped thulium (Tm) fiber pumped by 793-nm diodes can be exploited to obtain quantum efficiency near 2. Continuous-wave power as high as 1 kW has been obtained from a Tm fiber amplifier [2].

There has been significant progress in the development of femtosecond fiber lasers at $\sim$ 2 μm. Sub-500 fs pulses were realized in the first soliton Tm fiber laser back in 1995 [3]. Pulse durations as short as $\sim$ 50 fs have been achieved in dispersion-managed cavities, with pulse energy $<$ 1 nJ [4, 5]. A cavity containing a grating and telescope combination for the normal-dispersion segment generated 5.4-nJ and 216-fs pulses [6]. The pulse energy is the highest previously reported for a femtosecond Tm fiber laser, but the modified grating system for dispersion compensation compromises the practical benefits of fiber. A Ho-doped fiber laser operating with net cavity dispersion near zero generated 160-fs pulses at $\sim$ 2.1 μm [7].

[1]Much of the work presented in this chapter was published in Optics Letters [1].

Recent work has demonstrated the performance benefits of operating fiber lasers at large normal dispersion, and in particular the highest pulse energies have been obtained in the dissipative-soliton (DS) regime [8]. The DS and self-similar (SS) pulse evolutions [9, 10, 11] allow the best combinations of high energy and short pulse duration. Reports of normal-dispersion 2-μm fiber lasers are limited, and the performance lags behind that achieved at shorter wavelengths. A steep-sided spectrum with the characteristic cat-ear features, which is a signature of DS evolution, has been observed in several reports [12, 13, 14]. However, in these lasers the pulse energy is still well below that expected. An obvious challenge to designing normal-dispersion lasers is the anomalous dispersion of passive and standard Tm-doped silica fibers. Questions have also been raised about possible limitations that arise from gain-assisted modulation instability in lasers with anomalous-dispersion gain media [15, 16]. Thus, there is substantial motivation to investigate normal-dispersion Tm and Ho fiber lasers.

We report a study of a mode-locked Tm fiber laser with varying normal dispersion. It is difficult to reach the high-energy dissipative-soliton regime due to the anomalous dispersion of most fibers at 2 μm. With large normal dispersion, the laser exhibits elements of self-similar pulse evolution, and is the first Tm fiber laser to achieve the performance benefits of normal-dispersion operation. The behavior and performance with varying net cavity group delay dispersion (GDD) and filter bandwidth are presented. Experimental results agree well with trends in numerical simulations. The laser generates 7.6-nJ pulses, which can be dechirped to 130 fs duration. The resulting peak power is 4 times higher than that of previous Tm fiber lasers. This is a major improvement over the performance of previous Tm fiber lasers. Factors that limit the performance, and routes to further performance increases, will be discussed.

3.2 Laser design and numerical simulations

Tm-doped gain fibers typically exhibit large anomalous dispersion, which differs from Yb-doped and some Er-doped gain fibers. Numerical simulations were performed to assess the feasibility of reaching the DS regime in a laser with large anomalous dispersion in the gain medium. As a practical matter, the use of some anomalous-dispersion passive fibers (as component pigtails) is also unavoidable. The simulations were based on the ring cavity of Figure 3.1 and the parameters of the fibers are listed in Table 3.1. The fiber pigtails of the WDM and two collimators are all SMF28e, with a total length of 2 m. The gain fiber (TH512 from CorActive) has a core diameter of 9 μm and NA of 0.16, and is modeled with 30 dB small-signal gain, 100-nm Gaussian gain bandwidth at the center wavelength of 1920 nm, and saturation energy of 5 nJ. Due to the anomalous dispersion of the gain fiber and SMF28e, the laser will have a dispersion map and we need to consider its role in pulse propagation.

To shift the cavity GDD to the normal regime, ultra-high NA fibers (Nufern) are employed [17, 18]. In these fibers the strong waveguide dispersion exceeds the material dispersion. The mismatch of core sizes with other fibers can cause self-lasing within the cavity due to reflections at the splice points. Among the ultra-high NA fibers, UHNA4 has the lowest splice loss (0.4 dB) with SMF28e, and is employed after the gain segment to avoid reflections that can disrupt mode-locking. UHNA7 is designed for relatively low loss ($\sim$ 20 dB/km) and has a splice loss of 0.7 dB with SMF28e, so it is used in front of the gain fiber for GDD control. The combination of a long UHNA7 segment and a short UHNA4 segment (Figure 3.1) yields net normal cavity GDD, with minimal loss and reflections. The splice loss is negligible between other fibers and modeled using the same values between fiber

segments in simulations. The output coupling ratio and linear cavity loss are both assumed to be 70%. A lumped saturable absorber with 100% modulation depth and saturation power of 1 kW is assumed. A variety of filters were tried in simulations and a 16-nm Gaussian filter is used to achieve the broadest spectra for initial demonstrations.

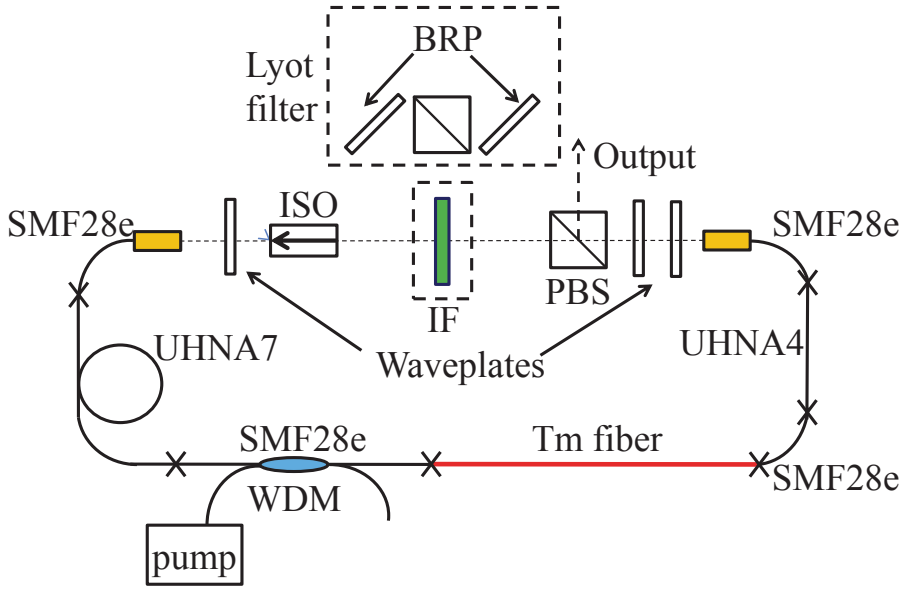

Figure 3.1: Schematic of laser: BRP: birefringent plate; IF: interference filter; PBS: polarizing beam splitter; ISO: isolator; WDM: wavelength-division multiplexer.

Table 3.1: Values of parameters used in Tm laser simulation

Fiber	Aeff	GVD	TOD	Length
	(μm^2)	(fs^2/mm)	(fs^3/mm)	(m)
UHNA7	11	90	-33	4.2
UHNA4	23	93	154	1.2
Tm	78	-73	96	1
SMF28e	98	-71	104	2

Simulations produce stable pulses for cavity GDD up to $\sim 10\ ps^2$ with the 16-nm filter. An example of a typical converged solution is shown in Figure 3.2 with GDD $\sim 0.3\ ps^2$. Pulse propagation is strongly affected by the filter, with negligible contribution from gain filtering. The pulse duration and spectral bandwidth

breathe by a factor of 5 as the pulse traverses the cavity. The pulse broadens in the normal-dispersion sections and compresses in the anomalous-dispersion sections, and is positively-chirped and far from the transform limit throughout the cavity. These features are qualitatively similar to the evolution in a passive self-similar laser [9]. However, the strong spectral breathing contrasts with the evolution in a passive self-similar laser; on the other hand, it is quite similar to that of lasers with self-similar evolution in the gain segment [10, 11]. The misfit parameter M is the root-mean-square deviation of the pulse shape from a parabolic pulse with the same energy. We see that the pulse reshapes dramatically in the first segment of UHNA fiber, and approximates a parabola well (M $\sim$ 0.02) after the second UHNA segment until it is filtered. The maximum stable pulse energy is 15 nJ. The cavity dispersion was varied by changing the length of UHNA7. Even with very large dispersion, the dispersion map evidently hinders the formation of DSs. The hybrid self-similar pulse evolution is a consequence of the joint action of the strong dispersion map and the filter.

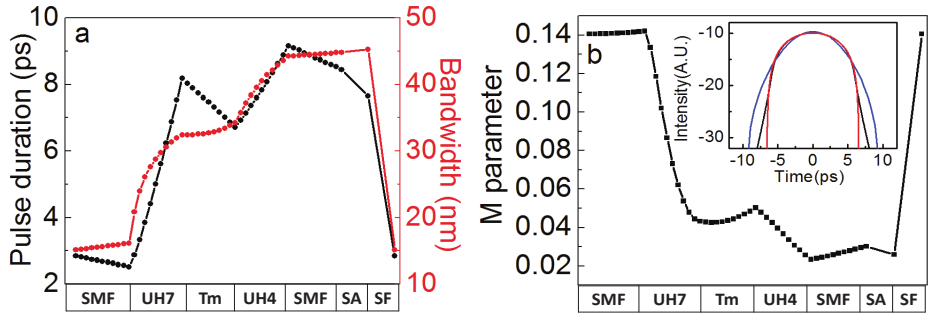

Figure 3.2: (a) Simulated variation of pulse duration and spectral bandwidth along the cavity (SA: saturable absorber, SF: spectral filter). The pigtail segment of WDM is neglected for clarity; (b) pulse shape evolution compared with a parabolic pulse; inset: comparison of pulse shape after UHNA4 (black) with Gaussian pulse (blue) and parabolic pulse (red) in log scale.

3.3 Experiments

We constructed a laser as in Figure 3.1. Pump light at 1569 nm is provided by a home-built erbium fiber laser and coupled into the cavity through a wavelength-division multiplexer (WDM) with 2-by-2 ports. The pigtails on the WDM and collimators amount to a total of 2 m of SMF28e. An interference filter with 16-nm bandwidth and peak transmission of 90% was used initially. The wave plates and PBS implement nonlinear polarization evolution (NPE), which also provides the output port. The isolator ensures unidirectional operation of the laser. The output power is measured after a long-pass filter that cuts on at 1650 nm, to eliminate residual pump light. The lengths of UHNA fibers and the filter bandwidth were varied to study the behavior of the laser. The resulting pulse repetition rate was in the range of 20-30 MHz. Operation with a single pulse in the cavity was verified with an autocorrelator with 150-ps scan range and a detector with 30-ps risetime. The pulse width was obtained from the interferometric autocorrelation based on 2-photon photoconductivity of a silicon detector, and a deconvolution factor of 1.45 was assumed.

The influence of cavity GDD was studied by varying the length of UHNA7. Initial lengths of 2.2 m of UHNA7 and 1.2 m of UHNA4 yield GDD $\sim 0.1\ ps^2$. The dispersion was gradually increased by adding UHNA7 before the gain fiber, without changing other fiber segments. This laser can be mode-locked for dispersion as large as $0.37\ ps^2$. Mode-locking was usually initiated at high pump power through fine adjustment of the wave plates. Typically, the laser started in a multi-pulsing state, and a single-pulsing state was obtained by reducing the pump power.

The output pulse parameters are summarized in Figure 3.3. The pulse chirp, dechirped and transform-limited pulse duration, and the pulse energy all increase

with cavity GDD, while the spectrum narrows. The experimental data and simulation results exhibit similar trends. The output pulse chirp is less than the cavity GDD, as is the case for self-similar lasers [11]. In contrast, for DS lasers without a dispersion map, the pulse chirp is comparable to or larger than the cavity GDD.

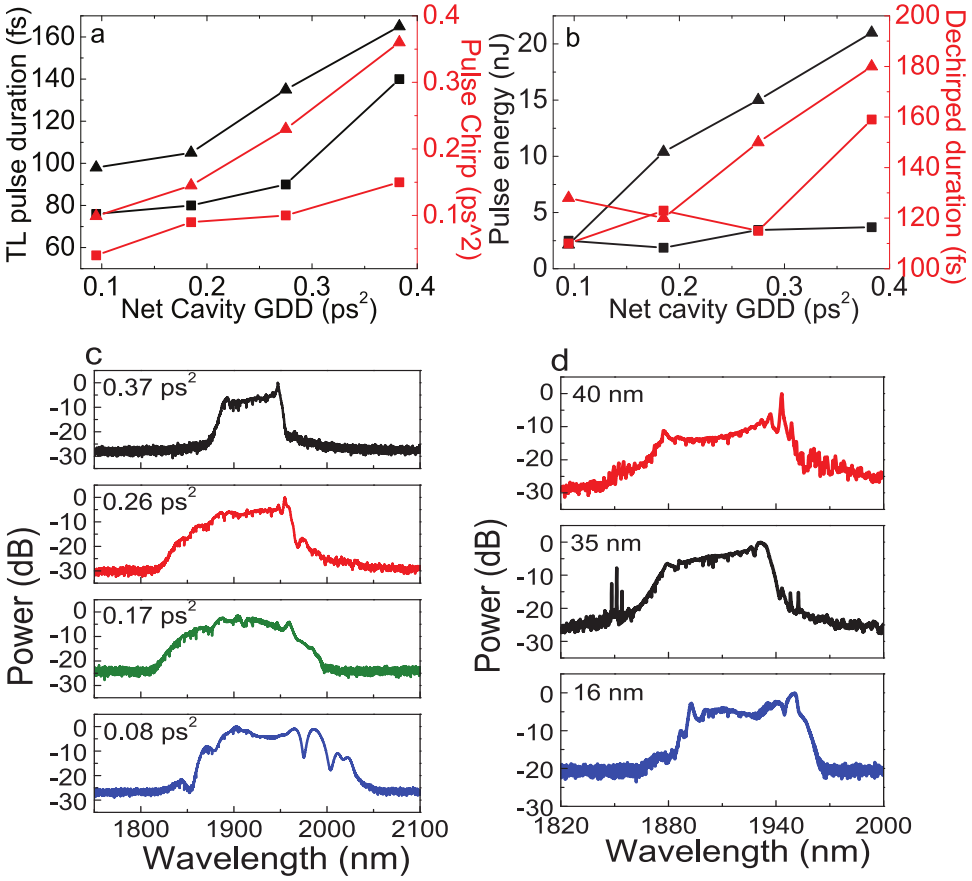

Figure 3.3: (a, b) Comparison between experimental and simulation results (squares: experimental data, triangles: simulation results); (c) mode-locked spectra at various cavity GDD with the 16-nm filter (blue: 0.08 ps^2, green: 0.17 ps^2, red: 0.26 ps^2, black: 0.37 ps^2); (d) mode-locked spectra with varying filter BW at cavity GDD $\sim$ 0.28 ps^2 (blue: 16 nm filter BW, black: 35 nm filter BW, red: 40 nm filter BW).

The length of UHNA4, where most of the NPE occurs, was varied to optimize the performance. We used 4.2 m of UHNA7 and kept all other components fixed. Best performance was obtained with 1.1 m of UHNA4. The laser emitted 7.6-nJ and 3-ps chirped pulses with spectral bandwidth of 80 nm at the -10 dB level,

which could be dechirped to 130 fs (within 10% of the transform limit) *via* a grating pair (Figure 3.4). The minor discrepancy from the transform-limited pulse is probably due to nonlinear phase in the pulse and higher-order dispersion of the grating pair. After dechirping with gratings with overall efficiency of 65% the peak power is $\sim$ 40 kW, which is 4 times the peak power of previous Tm fiber lasers. By minor adjustments of the cavity the pulse energy could be increased to 8.3 nJ, with 150-fs pulse duration. Finally, the radio-frequency spectrum confirms stable mode-locking. The dynamic range of the measurement is limited by the detector and spectrum analyzer, but for frequency offsets in the range of 100 kHz (covering relaxation oscillations), any sidebands are more than 70 dB below the first harmonic.

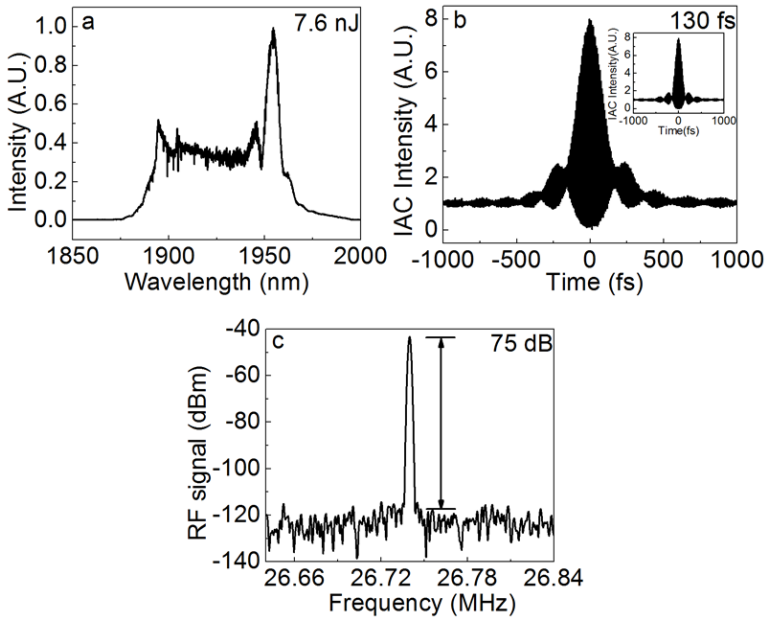

Figure 3.4: Experimental (a) output spectrum, (b) autocorrelation of dechirped pulse (inset: autocorrelation of transform limited pulse), (c) radio-frequency spectrum (span range: 200 kHz, RBW: 1 kHz) corresponding to 7.6 nJ pulse energy.

3.4 Conclusion

Although the numerical simulations indicate that stable pulses should be obtained at energies as high as 15 nJ, we observed experimentally that the pulse energy was limited by multi-pulsing. A low multi-pulsing threshold is often a symptom of too-narrow filter bandwidth in normal-dispersion lasers, so we investigated the influence of filter bandwidth on the performance. A single birefringent filter was first tried for larger bandwidth. However, mode-locking was hard to achieve, and we suspect that this can be attributed to the multiple transmission bands of the filter within the Tm gain spectrum. A Lyot filter (indicated in Figure 3.1) was used to suppress the secondary transmission peaks. With available birefringent plates, this combination can provide a filter bandwidth of 35 nm or 40 nm and free spectral range of 140 or 160 nm respectively, which ensures a single-peaked pass-band within the gain spectrum. The laser was mode-locked with very similar pulse energy and bandwidth using several different filters (Figure 3.3d), with the performance still limited by multi-pulsing. Information about the pulse evolution in the cavity can be inferred from the pulse extracted from the unused port of the WDM. For the 35-nm and 40-nm Lyot filters, the spectral bandwidth after passing through the WDM is 23 nm and 28 nm, respectively. Thus, we tentatively conclude that the WDM contributes to an overall filter in the cavity, and this limits the performance. In simulations, pulse energies larger than 20 nJ are reached with a filter bandwidth of 30 nm. The pulse energy in the current cavity is limited by accumulated nonlinear phase of $\sim 10\ \pi$ before wave-breaking occurs in the simulations. Gain fibers with lower anomalous dispersion, or even normal dispersion, are desirable to ultimately increase the pulse energy by reaching the DS regime. DS-like spectra have been produced by a laser with normal-dispersion gain fiber [14].

In conclusion, we have demonstrated a Tm fiber laser operating at large normal dispersion with hybrid self-similar evolution. Despite technical limitations in realizing suitable intracavity filters, the design reported here achieves 7.6-nJ and 130-fs pulses. These are so far the shortest pulses with highest energy in this dispersion regime, and yield a 4-fold improvement in peak power over previous Tm fiber lasers.

Portions of this work were supported by the National Science Foundation (ECCS-1306035). I want to thank Erin Lamb and Logan Wright for helpful discussions.

BIBLIOGRAPHY

[1] Y. Tang, A. Chong, and F. W. Wise, Opt. Lett. **40**, 2361 (2015).

[2] T. Ehrenreich, R. Leveille, I. Majid, K. Tankala, G. Rines, and P. Moulton, Proc. SPIE **7580**, 758016 (2010).

[3] L. E. Nelson, E. P. Ippen, and H. a. Haus, Appl. Phys. Lett. **67**, 19 (1995).

[4] J. Jiang, C. Mohr, J. Bethge, A. Mills, W. Mefford, I. Hartl, M. E. Fermann, C.-C. Lee, S. Suzuki, T. R. Schibli, N. Leindecker, K. L. Vodopyanov, and P. G. Schunemann, in *Conf. Lasers Electro-Optics 2012* (PUBLISHER, ADDRESS, 2012), p. CTh5D.7.

[5] Y. Nomura and T. Fuji, Opt. Express **22**, 12461 (2014).

[6] F. Haxsen, D. Wandt, U. Morgner, J. Neumann, and D. Kracht, Opt. Express **18**, 18981 (2010).

[7] P. Li, A. Ruehl, U. Grosse-Wortmann, and I. Hartl, Opt. Lett. **39**, 6859 (2014).

[8] W. Renninger, A. Chong, and F. Wise, Phys. Rev. A **77**, 023814 (2008).

[9] F. Ilday, J. Buckley, W. Clark, and F. Wise, Phys. Rev. Lett. **92**, 213902 (2004).

[10] B. Oktem, C. Ülgüdür, and F. Ö. Ilday, Nat. Photonics **4**, 307 (2010).

[11] W. H. Renninger, A. Chong, and F. W. Wise, Phys. Rev. A **82**, 021805 (2010).

[12] F. Haxsen, D. Wandt, U. Morgner, J. Neumann, and D. Kracht, Opt. Lett. **37**, 1014 (2012).

[13] R. Gumenyuk, I. Vartiainen, H. Tuovinen, and O. G. Okhotnikov, Opt. Lett. **36**, 609 (2011).

[14] Q. Wang, J. Geng, T. Luo, and S. Jiang, Proc. SPIE **8237**, 82371N (2012).

[15] G. Agrawal, IEEE Photonics Technol. Lett. **4**, 562 (1992).

[16] R. Gumenyuk and O. G. Okhotnikov, IEEE Photonics Technol. Lett. **25**, 133 (2013).

[17] H. Liu, K. Kieu, S. Lefrancois, W. H. Renninger, A. Chong, and F. W. Wise, CLEO 2011 - Laser Sci. to Photonic Appl. 1 (2011).

[18] R. Kadel and B. R. Washburn, Appl. Opt. **54**, 746 (2015).

CHAPTER 4

GENERATION OF INTENSE 100-FS SOLITONS TUNABLE FROM 2 TO 4.3 μM IN FLUORIDE FIBER[1]

There is great interest in sources of coherent radiation in the mid-wave infrared (3-5 μm), and instruments based on fiber can offer major practical advantages. This range, and much broader, can be covered easily by supercontinuum generation in soft glass fibers, but with low power spectral density. For applications that require intense ultrashort pulses, fiber sources are quite limited. In this letter, we report a fiber-based system that generates 100-fs pulses with 5 nJ energy, continuously wavelength-tunable over 2-4.3 μm through the soliton self-frequency shift (SSFS) in fluoride fibers. The pulse energies are two orders of magnitude higher than those previously achieved by SSFS around 3 μm, and the range of wavelengths is extended by 1000 nm. Peak power ranges from 20 to 75 kW are achieved across the tuning range. Numerical simulations are in good agreement with the experimental results, and indicate the potential for few-cycle soliton generation out to 5.6 μm. Fiber-integrated sources of femtosecond pulses tunable across this region should be valuable for mid-infrared applications.

4.1 Introduction

The mid-infrared (MIR) spectral region is of great importance to both fundamental research and applications. Mid-infrared spectroscopy [2] offers unique capabilities to detect and identify various molecules in different environments, including real-time breath analysis [3], trace gas detection, and early cancer diagnostics [4]. The 3-5 μm region is a transparent window in the atmosphere, and is suitable for

[1]Much of the work presented in this chapter was published in Optica [1].

LIDAR and remote sensing. These technologies can be greatly improved through the development of intense coherent MIR sources, which will also facilitate studies in strong-field physics, high-harmonic generation and attosecond science [5].

New scientific discoveries and practical applications in the MIR region will require versatile light sources with high spectral density and continuous tunability over a wide spectral range. Currently, MIR light sources are mainly based on solid-state laser systems. Quantum cascade lasers [6] emit from 3 to 25 μm. They are usually operated continuous-wave, and reach watt-level powers [7]. Demonstrations of short pulse operation are rare [8]. Kerr-lens mode-locked Cr^{2+}:ZnS lasers cover a broad range around 2.4 μm, with impressive few-cycle pulses [9]. Difference frequency generation (DFG) using near-infrared lasers can provide pulsed sources over a broad MIR range [10]. Microjoule-level pulses, tunable over 3-20 μm, were obtained from a solid-state optical parametric oscillator (OPO) pumped by a Ti:sapphire amplifier system [11]. The output from the DFG process can be boosted to higher pulse energy by optical parametric chirped pulse amplification [12]. However, all these solid-state systems require bulky and complex optical systems.

Fiber-based light sources compete with solid-state systems due to their compactness, low cost, and maintenance-free operation. MIR supercontinuum spanning more than three octaves (1.4-14.3 μm) was generated in a chalcogenide fiber [13]. The power spectral density is naturally low, and many applications would benefit from intense short pulses. Mode-locked erbium (Er) ZBLAN ($ZrF_4BaF_2LaF_3AlF_3NaF$) fiber lasers have recently been demonstrated at 2.8 μm but are not tunable [14, 15]. Fiber-based light sources employed DFG to generate femtosecond pulses with 10-pJ energy tunable over the MIR [16, 17]. MIR

frequency combs serve as increasingly-important tools for massively parallel spectroscopy with unprecedented speed, precision, sensitivity and spectral coverage [18]. They have been realized by degenerate OPO systems with fiber-based seed lasers and bulk crystals [19, 20], which motivates the development of fiber-based high-energy MIR femtosecond pulses.

The soliton self-frequency shift (SSFS) in optical fibers provides high-quality femtosecond pulses with wide spectral tunability [21, 22]. Recently, SSFS has been explored to reach the MIR region [23]. Standard silica fibers are limited to about 2.5 μm, while germanium-doped silica fibers reach almost 3 μm. To obtain soliton shifting further into the MIR, soft-glass fibers with low phonon energies are desirable. Koptev *et al.* achieved spectral coverage up to 2.65 μm in microstructured tellurite fibers with 100-fs soliton pulses [24]. However, sub-50 pJ pulse energies were obtained, limited by the high nonlinearity of the fiber. Impressive results with soliton wavelength up to 3.42 μm were realized in a chalcogenide fiber pumped at 2.8 μm [25]. The picojoule-level energy was limited by the high nonlinearity of the chalcogenide fiber and the low pump pulse energy.

Fluoride glass fibers have drawn attention due to their wide MIR transparency window, relatively high strength, and low background loss [26]. Compared to tellurite and chalcogenide fibers, they have much smaller nonlinear indices and shorter zero-dispersion wavelengths (ZDWs). Based on these properties, 100-fs solitons with roughly 100 times the energy (10-nJ level) or peak power of solitons in tellurite or chalcogenide fibers are expected. Approximately 0.5-nJ pulses of unspecified duration at 2.5 μm were obtained in an early experiment on SSFS in fluoride fiber [27]. Recently, Salem *et al.* demonstrated supercontinuum spanning 1.8 octaves in this kind of fiber, pumped by a thulium (Tm) fiber amplifier which

was in turn seeded by a Raman-shifted erbium fiber laser [28]. In that work, a dispersion-flattened fiber was pumped with 10-nJ and 100-fs pulses at 2.1 μm, which is near the ZDW.

Here we demonstrate a fiber-based system that generates 100-fs, nanojoule-energy soliton pulses *via* SSFS in fluoride fibers. Relative to experiments on continuum generation [28], we enhance Raman soliton formation by pumping the fluoride fiber in a region with strong anomalous dispersion, using shorter pulses with about 15 times higher peak power. The generated Raman solitons are continuously tunable from 2 to 4.3 μm. The pulse energy is a 2-order-of-magnitude improvement over previous Raman solitons at wavelengths beyond 2.5 μm. Numerical simulations of the soliton propagation are in good agreement with the experimental results, and indicate the potential for few-cycle soliton generation above 5 μm. The work reported here demonstrates that SSFS can serve as an important source of coherent ultrashort pulses with broad tunability for applications in the 3-5 μm range.

4.2 Description of fibers

We employed two kinds of fluoride fibers for the study of SSFS (Thorlabs models P3-32F-FC-2 and P3-23Z-FC-1). The indium fluoride (InF_3) fiber has a core diameter of 9 μm and numerical aperture of 0.26. The single-mode cutoff wavelength is 3.2 μm, and the propagation loss is specified as lower than 0.5 dB/m over 2.0-4.5 μm. The ZDW for the InF_3 fiber is $\sim$ 1.71 μm. The zirconium fluoride (ZrF_4) fiber has a core diameter of 9 μm and NA of 0.19. The single-mode cutoff wavelength is 2.3 μm, and the propagation loss is specified as lower than 0.2 dB/m over

2.0-3.7 μm. The zero-dispersion wavelength for the ZrF_4 fiber is $\sim$ 1.62 μm. The parameters of the fluoride fibers used in the experiments are plotted in Figure 4.1. The InF_3 fibers have benefits over the ZrF_4 fibers in their capability to transmit wavelengths beyond 5.4 μm [29]. The fibers are protected in patch cables, with both ends terminated by angled ferrule connectors to reduce reflections.

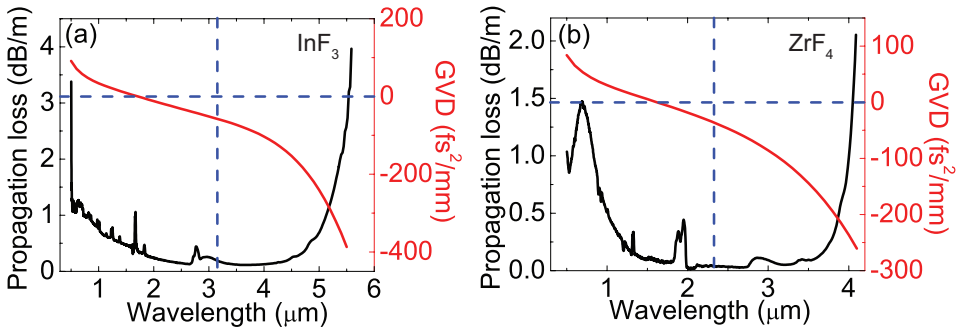

Figure 4.1: The parameters of the fluoride fibers used in the experiments. The group velocity dispersion (GVD) of the fundamental mode and the propagation loss for the (a) InF_3 fiber; (b) ZrF_4 fiber. The horizontal blue dashed line indicates the position of the zero GVD value. The vertical blue dashed line indicates the single mode cutoff wavelength.

To achieve a tunable light source with a spectrally-separated shifted soliton, pumping deep in the anomalous dispersion regime of fiber with low nonlinearity is desirable. In this way, a smaller number of fundamental solitons is excited, and energy conversion to the most-redshifted soliton is maximized [22]. Our experiments are based on pumping at 1.9 μm, which is the longest wavelength we can reach with stable pulses.

4.3 Numerical simulations

Numerical simulations were performed to assess the feasibility of reaching the MIR region through SSFS in these fibers.

Considering the single-mode cutoff wavelength of the fibers and our focus on the 3-5 μm region, simulations were conducted assuming only fundamental-mode propagation. We employed the generalized nonlinear Schrödinger equation, including dispersion terms up to the 8th order, stimulated Raman scattering, self-steepening, and propagation loss increasing exponentially with wavelength beyond 4 μm [30]. Due to the large variation of the effective area of the mode over this wide wavelength range, the frequency-dependence of the effective area is accounted for by introducing a first-order correction to the timescale τ_{shock} associated with self-steepening and optical shock formation at the pump wavelength [31].

$$\frac{\partial A}{\partial z} + \frac{\alpha}{2}A - \sum_{n\geq 2}^{8} \frac{i^{n+1}}{n!}\beta_n \frac{\partial^n A}{\partial T^n} = i\gamma \left(1 + i\tau_{shock}\frac{\partial}{\partial T}\right) \left(A(z,T)\int_{-\infty}^{\infty} R(T') \times |A(z,T-T')|^2)dT' + i\Gamma_R(z,T)\right) \quad (4.1)$$

The equation is solved with the standard split-step technique, with a 4th order Runge-Kutta integration for the nonlinear step. A temporal resolution of 0.44 fs and spectral resolution of 8.6 GHz are used. The frequency range extends over 1200 THz. A time window of 120 ps and step size of 1 μm in propagation are employed. The convergence of the simulation results is confirmed by comparing with those obtained using higher resolution.

The β_n terms up to the 8th order are the dispersion values for the fundamental mode in the fluoride fibers, calculated based on the Sellmeier equations with their refractive indices and numerical aperture, measured by the manufacturer. The linear propagation loss α is set to be 0.2 dB/m for the wavelengths shorter than the pump wavelength and increases exponentially into the deep MIR region. The frequency dependence of the loss is modeled as:

$$\alpha(f) = a \times e^{-\frac{f-f_0}{b}} + c \tag{4.2}$$

where f is the frequency in the unit of PHz and f_0 is the frequency at pump wavelength. The coefficients for the InF_3 fiber at pump wavelength of 1.9 μm are $a = 1.13 \times 10^{-10}$ dB/m, b=0.00434 PHz, c=0.0997 dB/m. The coefficients for the ZrF_4 fiber at pump wavelength of 1.9 μm are $a = 1.12 \times 10^{-11}$ dB/m, b=0.00328 PHz, c=0.0423 dB/m.

The nonlinear coefficient γ is evaluated at the pump frequency ω_0 and the generally accepted value of nonlinear refractive index is $n_2 = 2.1 \times 10^{-20}$ m^2/W [26], which is used in the simulations. Due to the large variation of the effective area of the mode over this wide wavelength range, the frequency-dependence of the effective area is accounted for by introducing a first-order correction to the timescale τ_{shock} at the pump wavelength. The variation of the nonlinear refractive index is negligible.

$$\tau_{shock} = \frac{1}{\omega_0} - \left[\frac{1}{A_{eff}(\omega)}\frac{dA_{eff}(\omega)}{d\omega}\right]_{\omega_0} \tag{4.3}$$

The response function $R(t)$ includes both instantaneous electronic and delayed Raman contributions. The Raman response is modeled as a simple damped oscillation in the temporal domain with two time constants τ_1=16.67 fs and τ_2=20.32 fs [32]. The fraction of Raman contribution in the nonlinearity is taken to be f_R=0.20 [33]. The effects of spontaneous Raman noise are introduced through $\Gamma_R(z,T)$.

Numerical results of launching 40-nJ and 70-fs $sech^2$-shaped pulses at 1.9 μm into the fundamental mode of a 2-m long InF_3 fiber are shown in Figure 4.2. The soliton number N for the input pulse is ~ 11. The spectral and temporal evolution

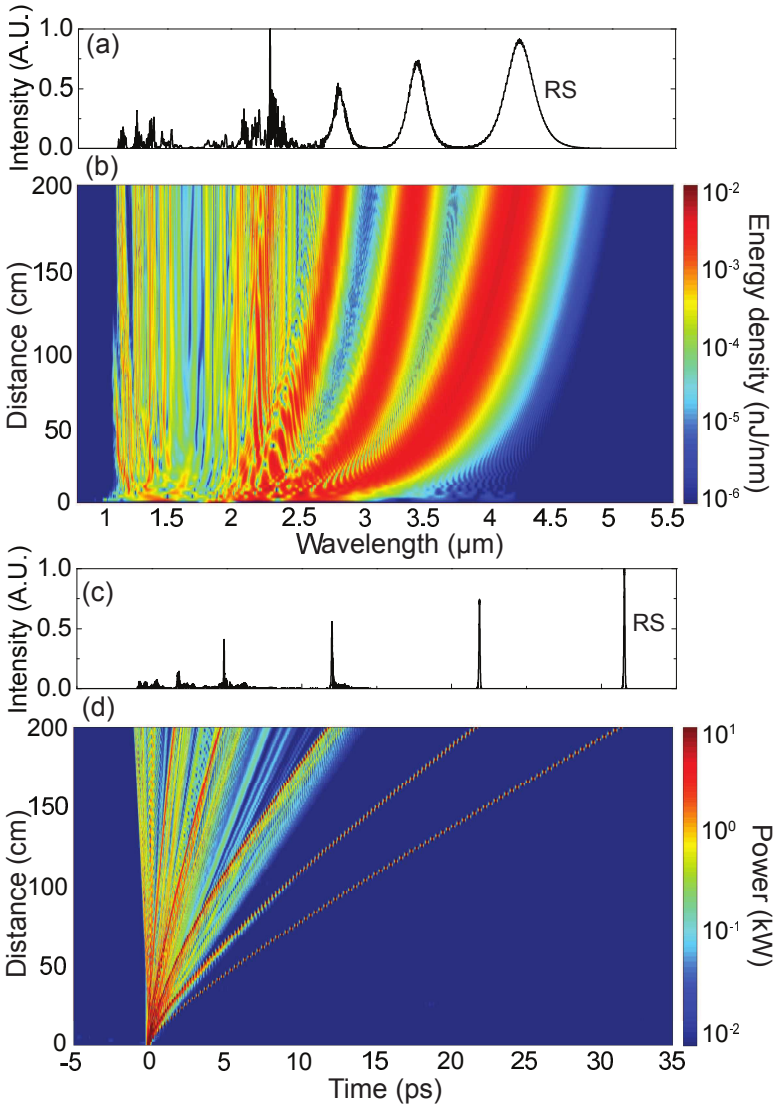

Figure 4.2: Simulation results for the (a) spectral output, (b) spectral evolution, (c) temporal output and (d) temporal evolution in a 2-m long InF_3 fiber with 40-nJ and 70-fs pulses coupled into the fundamental mode. RS: Raman soliton of interest at the longest wavelength.

of the pulses along the fiber exhibit the main features expected for fiber pumped in the anomalous dispersion regime with femtosecond pulses. Higher-order temporal solitons are initially formed, which then undergo fission under the perturbation of the higher-order dispersion and Raman scattering to break up into a series of constituent fundamental solitons. These experience frequency shifts, shed energy

into dispersive waves in the normal dispersion regime, and eventually separate spectrally and temporally. The most-shifted soliton (labeled RS in Figure 4.2) is at 4.3 μm and has 80-fs duration and 5-nJ energy.

4.4 Experiments

The experimental setup is shown in Figure 4.3. An Er fiber chirped pulse amplification system delivers 550-fs pulses with 1.3 μJ energy at 1.55 μm and 1.5 MHz repetition rate. These are shifted to longer wavelengths by SSFS in a polarization-maintaining rod-type photonic crystal fiber (PCF) [34] with a mode-field diameter of 55 μm. The output pulses are collimated by a lens with a focal length of 50 mm, and a long-pass filter (LPF) that cuts on at 1.8 μm is used to select the most-redshifted soliton centered at 1.9 μm, which has 120-nJ pulse energy and 70-fs duration (Figure 4.4). The fringes on the spectrum are due to interference with residual light left from a second soliton centered at 1.7 μm. The pulse duration is measured using an interferometric autocorrelator based on two-photon absorption in a silicon photodetector. A deconvolution factor of 1.54 is assumed.

A half-wave plate is used to suppress residual unshifted light and other shifted solitons due to the polarization dependence of the blocking range of the LPF. These pulses are coupled into the fluoride fiber using an aspheric lens and collimated at the output using a protected silver reflective collimator with a 7 mm focal length. They then pass through a LPF which cuts on at 2.85 μm or 3.75 μm for selecting the most-redshifted soliton. Several Fourier-transform optical spectrum analyzers (OSAs), each covering a different wavelength range, are required to measure the output spectra. The pulse duration is measured using an interferometric

autocorrelator based on two-photon absorption in an InGaAs photodetector.

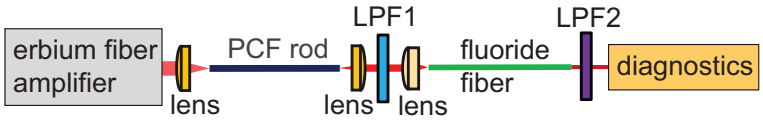

Figure 4.3: Schematic of the experimental setup for SSFS in fluoride fibers: LPF: long pass filter. LPF1 cuts on at 1.8 μm. LPF2 cuts on at 2.85 μm or 3.75 μm.

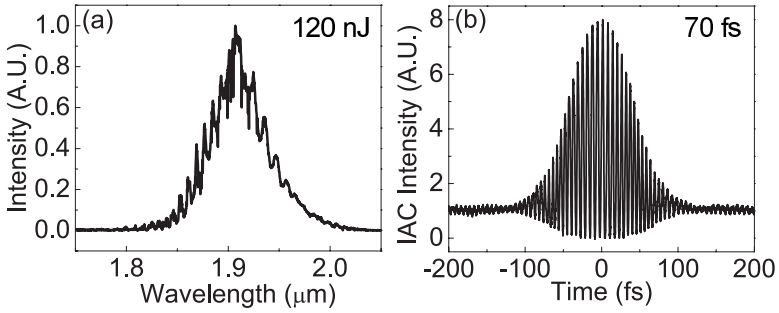

Figure 4.4: (a) The spectra and (b) the interferometric autocorrelation of the input light source at 1.9 μm.

Experiments were conducted with a 2-m InF_3 fiber. A 6-mm focal length lens was used to couple light into the fiber. By varying the incident pulse energy from 3 to 120 nJ using neutral density filters, we are able to continuously tune the center wavelength of the output pulses from 2 to 4.3 μm. The fiber is specified to be single-mode for wavelengths beyond 3.2 μm. The excitation of higher-order modes at the pump wavelength does not prevent the generation of Raman solitons in the fundamental mode. Any shifted energy in the higher-order modes experiences high loss upon passing the cutoff wavelength. This ensures a single-mode output beam after the LPF (for wavelengths beyond 3.2 μm). Soliton pulses with few-nanojoule energies and $\sim$ 100-fs durations are obtained at each wavelength. The representative examples shown in Figure 4.5 correspond to peak powers between 45 and 75 kW. The LPF introduces some chirp on the pulses, which leads to a 10% deviation from the transform limit. Further shifting to longer wavelengths should be possible with higher pump energy. However, at higher pulse energy we observe

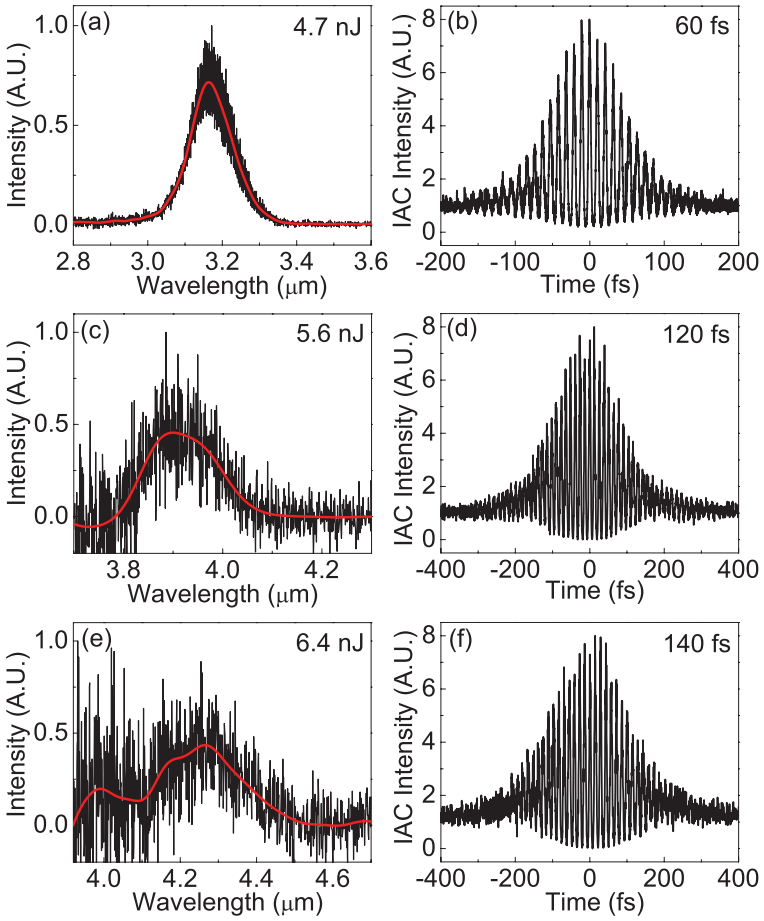

Figure 4.5: Measured spectra and the interferometric autocorrelations of the most-redshifted solitons at (a,b) 3.2 μm; (c,d) 3.9 μm; (e,f) 4.3 μm in the InF_3 fiber. The red lines indicate the spectra after noise reduction. A deconvolution factor of 1.54 was assumed to obtain the indicated pulse durations.

damage to the end face connector.

It is worth mentioning that even with the excitation conditions chosen to enhance Raman-soliton formation, broad supercontinuua are generated, as expected from the numerical results above. When the most-shifted soliton is near 4 μm, a continuum that spans more than two octaves is produced, with the short-wavelength edge $\sim$ 0.8 μm. The complete output spectra were recorded using three optical spectrum analyzers (ANDO AQ6315E: 0.35-1.7 μm, noise floor of -70 dBm/nm; Thorlabs OSA203: 1.0-2.5 μm, noise floor of -70 dBm/nm; and Thor-

labs OSA206: 3.3-8.0 μm, noise floor of -45 dBm/nm). The measured full spectra of the supercontinuum for a 2-m long InF_3 fiber with shifted solitons at 3.9 μm is shown in Figure 4.6. The spectra data measured by AQ6315E and OSA203 are stitched together at 1.67 μm. The gap from 2.5 μm to 3.3 μm could not be covered by available spectrum analyzers, since the instrument that covers 1-5.6 μm was not available when we did the experiments in the 2.5-3.3 μm range.

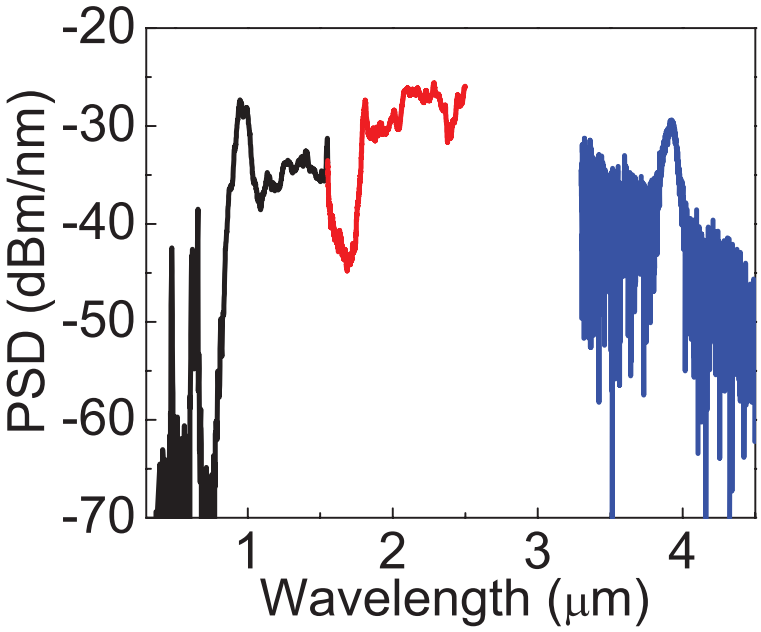

Figure 4.6: Measured full spectra in a 2-m long InF_3 fiber with shifted solitons at 3.9 μm. PSD: power spectral density.

We estimate that about 35% of the incident light is coupled into the fundamental mode. Over the range of wavelengths generated, 10-20% of the energy coupled into the fundamental mode of the fiber is converted to the most-shifted soliton. The overall practical energy conversion efficiency is therefore 3.5-7%.

The experimental results agree well with the numerical simulations that assume the measured coupling efficiency, for both the soliton wavelengths and energies. The comparison for the most redshifted solitons is shown in Figure 4.7. The nonlinear coefficient of the fiber exhibits strong wavelength dependence because the

mode area of the fiber increases with wavelength. Incorporating this dependence into the simulation is crucial to accurate modeling of the long-wavelength edges of the spectra.

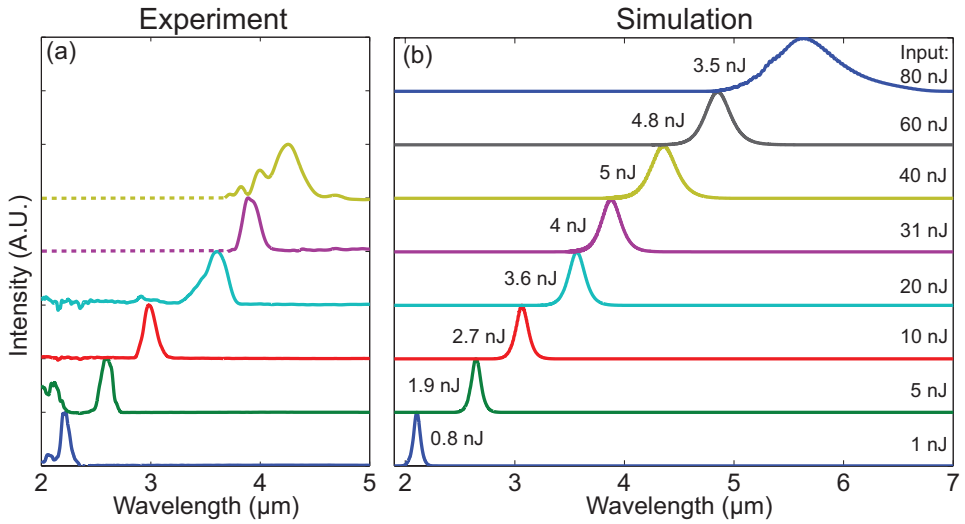

Figure 4.7: Spectra of the most redshifted soliton in the 2-m long InF_3 fiber at different wavelengths in (a) experiments; (b) numerical simulations. The dotted lines show the range which could not be covered by available spectrum analyzers. The soliton and input-pulse energies are indicated.

For wavelengths below 3.2 μm, the output is not specified to be single-mode. For the InF_3 fiber, the V number is 3.6 at 2 μm and there are 3 guided modes. The resulting $M^2 \sim 2$ might be adequate for many applications. To obtain a strictly single-mode beam below 3.2 μm, which is the cutoff wavelength of the InF_3 fiber, experiments were conducted using a 1-m long ZrF_4 fiber. The ZrF_4 fiber provides similar pulse performance as the InF_3 fiber for wavelengths around 3 μm, but it extends the wavelength region with single-mode output down to 2.3 μm. Numerical simulations of soliton self-frequency shift (SSFS) in a 1-m long ZrF_4 fiber with the same input pulse parameters in the paper exhibit similar results, with the soliton shifting out to 3.4 μm. Experimentally, output solitons up to 3.4 μm are obtained with estimated pulse duration of 70 fs, as predicted by the simulation. The use of the two fluoride fibers allows the generation of $\sim$ 100-fs pulses with spectral

coverage over 2-4.3 μm and diffraction-limited output beam for wavelengths above 2.3 μm.

4.5 Stability measurement

We performed a long-term (taken to be one hour) stability measurement of the pump pulses, the seed pulses and the output soliton pulses in terms of the center wavelengths and pulse powers (Figure 4.8).

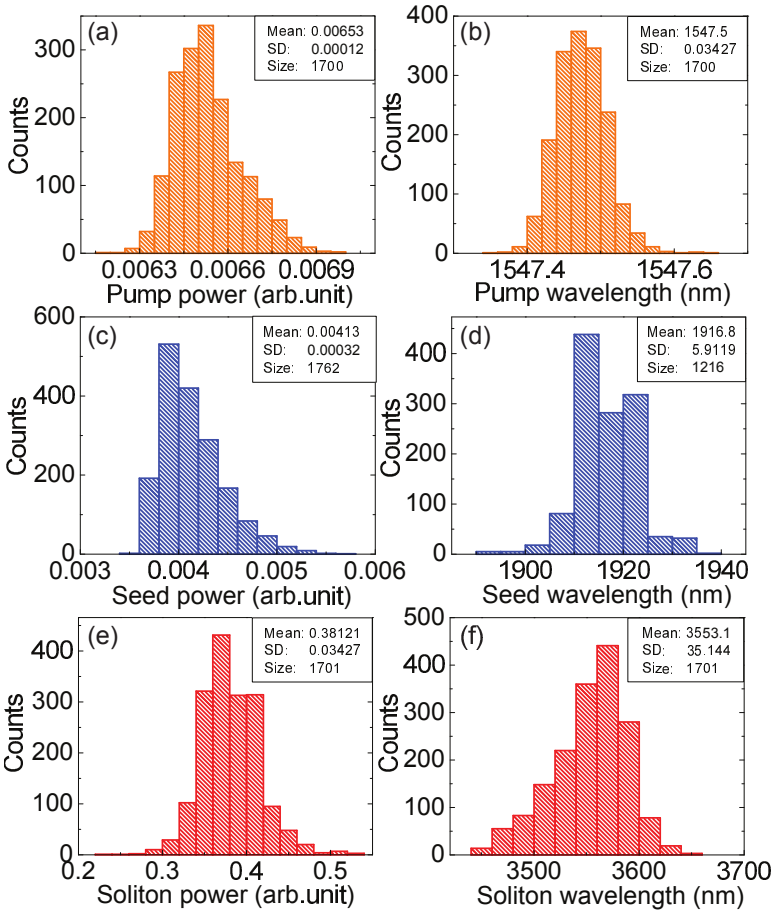

Figure 4.8: The stability measurement of the power and center wavelength variation of (a,b) the pump pulse; (c,d) the seed pulse; (e,f) the output soliton at 3.6 μm. SD: standard deviation.

For the pump pulses near 1550 nm, the coefficient of variation (standard deviation/mean) of the power is 1.8 %. The coefficient of variation of the pump wavelength is 0.002 %. Comparing the seed and output solitons, the coefficients of variation of the power are on the same levels (8 % vs. 9 %). The coefficients of variation of the wavelengths for the output soliton (1%) is 3 times larger than that of the seed pulses (0.31%), sharing the same order of magnitude.

We dont observe much amplification of the instability during the SSFS process in the fluoride fibers. We attribute this to the short pulse duration (70 fs) we used for pumping, since for short pulse excitation, the SSFS process is known to remain coherent even during the propagation in the anomalous dispersion regime [22]. Based on these measurements, this light source based on SSFS has the potential of being useful provided stable and short input pulses are available.

4.6 Discussion

It should be possible to achieve significantly better performance than the results reported here, by optimizing the conditions of the SSFS. For example, simulations show that launching 40 nJ in the fundamental mode of a 5-m long InF_3 fiber yields solitons that reach 5 μm. This would correspond to 120 nJ incident on the fiber. In the experiments described above, only 40 nJ out of the total 120 nJ pulse energy is effectively utilized. With better coupling design and the use of bare fibers to avoid damage, it should be possible to couple 80 nJ in the fiber. With that energy coupled into a 2-m long InF_3 fiber, simulations predict shifting out to 5.6 μm (Figure 4.7). Shifting to even longer wavelengths will be limited by the large anomalous dispersion and high loss of the InF_3 fiber.

While the source described here is an important step towards a practical, high-performance instrument, several improvements should be considered. Our approach uses cascaded SSFS stages, so it is reasonable to expect high noise due to nonlinear noise amplification and the coupling of spectral, temporal and intensity fluctuations in the SSFS process. Our measurements show that the long-term stability of the source is similar to that of the 1.9 μm source. This implies that a stable MIR source can be obtained provided the pump source is stable. The short input pulses used here ensure that noise has a minimal influence on the soliton fission and spectral-shifting processes. Further optimization of the SSFS process for high-power pulses, for shifts to greater wavelengths, and for better noise performance should be possible. As is well known, the soliton frequency shift is inversely proportional to the fourth power of the pulse duration [35]. A source of even shorter pulses at 2 μm will improve the performance in all respects. More studies will be needed to optimize the design for specific parameters, but there is considerable room for improvement from our current results: in the same InF_3 fiber used here, 50-fs, $\sim$ 100 nJ solitons at 5 μm are consistent with the soliton area theorem.

4.7 Conclusion

In summary, 100-fs pulses with nanojoule energies, wavelength-tunable from 2-4.3 μm, are generated by the SSFS in fluoride fibers. With peak powers around 50 kW, these are the most-intense mid-infrared pulses generated by a fiber source to date. A fiber-based, broadly-tunable source of short pulses should facilitate numerous applications in the important 3-5 μm region.

BIBLIOGRAPHY

[1] Y. Tang, L. G. Wright, K. Charan, T. Wang, C. Xu, and F. W. Wise, Optica **3**, 948 (2016).

[2] F. Tittel, D. Richter, and A. Fried, Top. Appl. Phys **89**, 458 (2003).

[3] M. R. McCurdy, Y. Bakhirkin, G. Wysocki, R. Lewicki, and F. K. Tittel, J. Breath Res. **1**, 014001 (2007).

[4] A. B. Seddon, Phys. Status Solidi B **250**, 1020 (2013).

[5] P. Agostini and L. F. DiMauro, Rep. Prog. Phys **67**, 813 (2004).

[6] Y. Yao, A. J. Hoffman, and C. F. Gmachl, Nat. Photonics **6**, 432 (2012).

[7] Y. Bai, N. Bandyopadhyay, S. Tsao, S. Slivken, and M. Razeghi, Appl. Phys. Lett. **98**, 82 (2011).

[8] C. Y. Wang, L. Kuznetsova, V. M. Gkortsas, L. Diehl, F. X. Kärtner, M. a. Belkin, A. Belyanin, X. Li, D. Ham, H. Schneider, P. Grant, C. Y. Song, S. Haffouz, Z. R. Wasilewski, H. C. Liu, and F. Capasso, Opt. Express **17**, 12929 (2009).

[9] S. Vasilyev, I. Moskalev, M. Mirov, S. Mirov, and V. Gapontsev, Opt. Lett. **40**, 5054 (2015).

[10] V. Petrov, Prog. Quantum Electron. **42**, 1 (2015).

[11] R. a. Kaindl, M. Wurm, K. Reimann, P. Hamm, A. M. Weiner, and M. Woerner, J. Opt. Soc. Am. B **17**, 2086 (2000).

[12] O. Chalus, P. K. Bates, M. Smolarski, and J. Biegert, Opt. Express **17**, 3587 (2009).

[13] C. R. Petersen, U. Møller, I. Kubat, B. Zhou, S. Dupont, J. Ramsay, T. Benson, S. Sujecki, N. Abdel-Moneim, Z. Tang, D. Furniss, A. Seddon, and O. Bang, Nat. Photonics **8**, 830 (2014).

[14] S. Duval, M. Olivier, V. Fortin, M. Bernier, M. Piche, and R. Vallée, SPIE Fiber Lasers XIII Technol. Syst. Appl. **9728**, 2 (2016).

[15] T. Hu, S. D. Jackson, and D. D. Hudson, Opt. Lett. **40**, 4226 (2015).

[16] C. Erny, K. Moutzouris, J. Biegert, D. Kühlke, F. Adler, A. Leitenstorfer, and U. Keller, Opt. Lett. **32**, 1138 (2007).

[17] Y. Yao and W. H. Knox, Opt. Express **21**, 26612 (2013).

[18] A. Schliesser, N. Picqué, and T. W. Hänsch, Nat. Photonics **6**, 440 (2012).

[19] N. Leindecker, A. Marandi, R. L. Byer, and K. L. Vodopyanov, Opt. Express **19**, 6296 (2011).

[20] A. Schliesser, N. Picqué, and T. W. Hänsch, Nat. Photonics **6**, 440 (2012).

[21] F. M. Mitschke and L. F. Mollenauer, Opt. Lett. **11**, 659 (1986).

[22] J. M. Dudley, G. Genty, and S. Coen, Rev. Mod. Phys. **78**, 1135 (2006).

[23] E. A. Anashkina, A. V. Andrianov, M. Yu. Koptev, S. V. Muravyev, and A. V. Kim, Opt. Lett. **39**, 2963 (2014).

[24] M. Y. Koptev, E. A. Anashkina, A. V. Andrianov, V. V. Dorofeev, A. F. Kosolapov, S. V. Muravyev, and A. V. Kim, Opt. Lett. **40**, 4094 (2015).

[25] T. Cheng, Y. Kanou, K. Asano, D. Deng, M. Liao, M. Matsumoto, T. Misumi, T. Suzuki, and Y. Ohishi, Appl. Phys. Lett. **104**, 121911 (2014).

[26] J. M. Parker, Annu. Rev. Mater. Sci. **19**, 21 (1989).

[27] C. R. Phillips, J. Jiang, C. Mohr, A. C. Lin, C. Langrock, M. Snure, D. Bliss, M. Zhu, I. Hartl, J. S. Harris, M. E. Fermann, and M. M. Fejer, Opt. Lett. **37**, 2928 (2012).

[28] R. Salem, Z. Jiang, D. Liu, R. Pafchek, D. Gardner, P. Foy, M. Saad, D. Jenkins, A. Cable, and P. Fendel, Opt. Express **23**, 30592 (2015).

[29] J.-C. GAUTHIER, S. P. VINCENT FORTIN, JEAN-YVES CARRÉE, M. POULAIN, R. VALLÉE, BERNIER, and MARTIN, Opt. Lett. **41**, 1756 (2016).

[30] D. C. Tran, G. H. Sigel, and B. Bendow, J. Light. Technol. **2**, 566 (1984).

[31] B. Kibler, J. M. Dudley, and S. Coen, Appl. Phys. B **81**, 337 (2005).

[32] X. Yan, C. Kito, S. Miyoshi, M. Liao, T. Suzuki, and Y. Ohishi, J. Opt. Soc. Am. B **29**, 238 (2012).

[33] Z. Chen, A. J. Taylor, and A. Efimov, Opt. Express **17**, 5852 (2009).

[34] N. G. Horton, K. Wang, D. Kobat, C. G. Clark, F. W. Wise, C. B. Schaffer and C. Xu, Nat. Photonics **7**, 205 (2013).

[35] G. P. Agrawal, *Nonlinear fiber optics* (Academic press, ADDRESS, 2007).

CHAPTER 5

HIGH ENERGY PULSES FROM ERBIUM ZBLAN FIBER LASERS

5.1 Introduction

There are strong interests in developing ultrafast fiber lasers working at increasingly longer wavelengths in the mid-infrared region above 2 μm. The reasons lie not only in the practical advantages of fiber-format laser sources, but also in the fact that ultrafast laser sources with new color capabilities open up doors for numerous applications. The molecular fingerprint region covering 2-13 μm enables the study of molecular structures and the dynamics in chemical reactions, as well as the precision molecular spectroscopy using frequency combs. Applications requiring pulses with high peak power, such as strong field physics, high-harmonic generation, also benefit from the development of ultrafast fiber lasers at these wavelengths.

This range can be partially covered by quantum cascade lasers (QCL) with mostly continuous-wave operations, but only rare demonstrations for picosecond pulse generations [1, 2]. The gain recovery time of QCL is on the order of a few picoseconds, while the cavity time is $\sim$ 40-60 ps. This fast gain dynamics is the main obstacle for stable passive mode-locking and impedes the formation of ultrashort pulses. Other solid-state light sources based on different parametric processes provide outstanding performances at these new colors, however, they are bulky and require complex optical systems [3].

Fiber lasers that employ erbium (Er) doped ZBLAN ($ZrF_4BaF_2LaF_3AlF_3NaF$) fibers stand out for covering the range from 2.7 μm to 2.9 μm, which supports

generation of sub-100 fs pulses. Continuous-wave power as high as 30 W [4] and slope efficiency up to 50% [5] have been obtained by researchers from Laval University and Macquarie University. Recently there has been a surge in studies and demonstrations of femtosecond fiber lasers centered around 2.8 μm. Sub-500 fs pulses with peak power of 6.4 kW were realized in a mode-locked Er ZBLAN soliton fiber laser [6] by nonlinear polarization evolution (NPE). Almost around the same time, a soliton laser with similar design delivering 207-fs pulses with 3.5 kW was obtained by the group in Laval University [7]. With further optimization of the cavity in terms of the output coupling ratio and the length of the gain fiber, they were able to obtain 270-fs pulses with 23-kW peak power [8]. To avoid the influence of the strong water absorbtion lines near 2.8 μm, soliton lasers with holmium as the gain medium working at 2.9 μm were also demonstrated [9]. These initial reports have already shown great results and people are continuing to explore better performance for these fiber lasers at new colors.

It has become well-known wisdom that operating lasers at large normal dispersion allows the best combination of high energies and short pulse durations employing pulse evolutions like dissipative soliton or self-similar pulse evolutions [10, 11]. Up to now, demonstrated mode-locked fiber lasers at 2.8 μm are all soliton lasers, with only anomalous dispersion gain fibers in the cavity. It is interesting and attractive to see how the performance scales if we introduce dispersion management elements and shift the net cavity dispersion to the normal regime. New pulse evolutions may as well be discovered along the road.

Here I investigate the pulse evolution and output performance of mode-locked Er ZBLAN fiber lasers with net normal dispersion. As is similar to the case of Tm doped fiber lasers [12], fiber-format dispersion compensation is used due to

its flexibility to tune and practical advantages. The behavior and performance with varying net cavity group delay dispersions (GDD) and filter bandwidths are presented. Some initial experimental results will be presented.

5.2 Laser design and numerical simulations

5.2.1 Chalcogenide fiber

Single mode Er-doped ZBLAN fibers have anomalous dispersion. To shift the cavity dispersion to the normal regime, chalcogenide fibers are used as normal dispersion fibers at 2.8 μm for dispersion compensation.

Chalcogenide glasses have low phonon energies, transmit light in the mid-infrared region from 2-10 μm. They normally exhibit 100 $\sim$ 1000 times higher nonlinear refractive indices compared with silica glasses. Chalcogenide fibers drawn from these glasses serve as great waveguides at this wavelength range. Single mode chalcogenide fiber used in this experiment is made from As_2S_3 glasses with a transmission range of 1.5-6 μm and single-mode cutoff wavelength at 2.46 μm. This fiber is IRF-S-6.5 from IRflex with a core/cladding size of 6.5 μm/125 μm and NA of 0.28. The dispersion profile kindly provided by the fiber supplier is shown in Figure 5.1.

Characterization of the nonlinear refractive index n_2 in this As_2S_3 fiber was conducted using peak power test and calibrated by the simulation of the spectral broadening in the same fiber. Pulses with 250-fs durations at 1.92 μm were free-space coupled into the 4.4-m long chalcogenide fiber, with both fiber ends angle

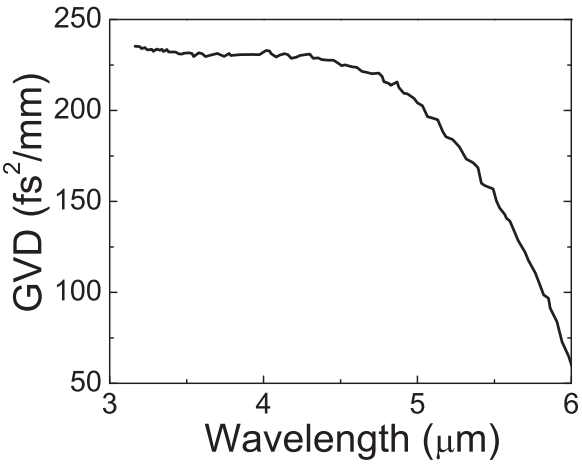

Figure 5.1: Group velocity dispersion of the chalcogenide fiber IRF-S-6.5.

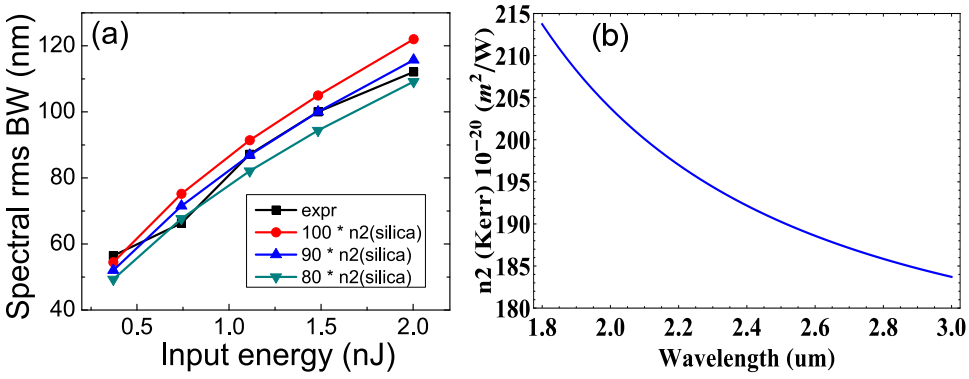

Figure 5.2: (a) Measurement of n_2 of the chalcogenide fiber IRF-S-6.5 using peak power test; (b) Extrapolation of n_2 at longer wavelengths using Miller's formula.

cleaved. Output spectra from the other end of the fiber at different power level were recorded, and their root-mean-squared bandwidths are calculated. In the meanwhile, simulations were conducted to model the same experimental conditions, assuming different levels of n_2 compared to that of silica fibers. From the comparison of spectral broadening results in Figure 5.2(a) assuming multiple levels of n_2, it can be inferred that n_2 of the As_2S_3 fiber at 1920 nm is $\sim$ 90 times that of silica fibers, with value of 207 $\times 10^{-20} m^2/W$.

With the information of the material dispersion, values of n_2 at other wavelengths can be extrapolated using Miller's formula [13], as shown in Figure 5.2(b).

Considering that the band gap energy of As_2S_3 corresponds to the wavelength of 560 nm and n_2 sharply decreases at multi-photon absorbtion wavelengths, the true value of n_2 in As_2S_3 fiber is expected to be less than 90 times that of silica fibers at 2.8 μm. Further assessment can be done once a mode-locked fiber laser at 2.8 μm is available.

Another critical parameter of the chalcogenide fibers is the Raman coefficient. Since the Raman peak gain scales with the third order nonlinear coefficient, a roughly 100-times stronger Raman effect would be expected based on the high nonlinearity of the material. The Raman coefficient in the simulations is calibrated using the existing experimental data in [14]. The Raman gain coefficient at 1550 nm is verified to be 4.3 $\times 10^{-12}$ m/W. The Raman response function of the As_2S_3 fiber in simulations is modeled using the single Lorentzian Raman response model:

$$R(t) = f_R h_R(t) + (1 - f_R)\delta(t - t_e) \tag{5.1}$$

$$h_R(t) = \frac{\tau_1^2 + \tau_2^2}{\tau_1 \tau_2^2} exp(-t/\tau_2) sin(t/\tau_1) \tag{5.2}$$

where values of $\tau_1 = 15.5fs$, $\tau_2 = 230.5fs$ are used [15]. The contribution of Raman part modeled by f_R is 0.1.

5.2.2 Laser design and simulation setup

The schematic of the laser design with dispersion compensation is shown in Figure 5.3. Cavity is mainly formed by two segments of fibers: an Er-doped double-cladding ZBLAN fiber, and a piece of chalcogeinde fiber (IRF-S-6.5). The Er-doped

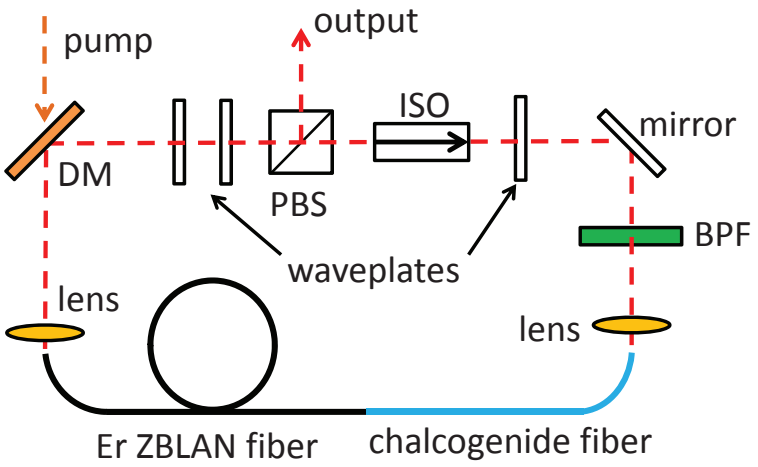

Figure 5.3: Schematic of the Er ZBLAN laser with dispersion compensation: PBS: polarizing beam splitter; ISO: isolator; BPF: bandpass filter; M: mirror; DM: dichroic mirror.

ZBLAN fiber from Le Verre Fluoré has a core/cladding diameter of 15.4/260 μm and NA of 0.12. It provides multimode pump guiding in the cladding with NA $>$ 0.46 and ensures single mode operation above 2.5 μm. The pump absorption in the cladding is 2.5$\sim$3 dB/m at 976 nm. Splicing between the ZBLAN gain fiber and chalcogenide fiber is non-trivial, so free-space coupling is used in between. Pump light at 976 nm is provided by a multi-mode diode and free space coupled into the gain fiber using a lens after passing through a dichroic mirror. Light coming out of the chalcogenide fiber is collimated by another lens. The wave plates and polarizing beam splitter (PBS) implement NPE for mode-locking, and PBS serves as the output port. The isolator ensures unidirectional operation of the laser. A bandpass filter is introduced for stabilization of the large normal dispersion operation.

Numerical simulations were conducted based on the laser design in Figure 5.3 for different fiber lengths and filter bandwidths. The parameters for fibers are listed in the Table 5.1. The gain fiber is modeled with 30 dB small-signal gain, 100-nm Gaussian gain bandwidth centered at 2.8 μm. The free-space coupling

ratio of the signal light into the chalcogenide fiber and the gain fiber are 60% and 65% respectively. The output coupling ratio and cavity loss are both assumed to be 70%. A lumped saturable absorber with 100% modulation depth and a saturation power of 4 kW is used. The transmission curve of the SA is ideal and monotonically increasing.

Table 5.1: Values of parameters used in the Er ZBLAN laser simulations

Fiber	Aeff	GVD	TOD	n_2
	(μm^2)	(fs^2/mm)	(fs^3/mm)	$(10^{-20}m^2/W)$
Er ZBLAN	224	-86	0	2.3
As_2S_3 fiber	45	208	-335	230

5.2.3 Simulation results for dispersion-managed soliton lasers

First, we simulate the cavity with 1.2-m long chalcogenide fiber and 3-m long Er ZBLAN fiber, resulting a net cavity dispersion of -0.0084 ps^2. The gain saturation energy is set to 0.45 nJ, which controls the pump power level. No filter is used in this cavity.

A typical converged solution is shown in Figure 5.4. The spectral bandwidth variation along the cavity is minimal, while the pulse duration varies significantly between the normal and anomalous dispersion fibers. The pulses are up-chirped and down-chirped at the end of the chalcogenide fiber and the gain fiber respectively. Output pulses are slightly down-chirped with 220-fs duration close to the transform limited. The pulse energy is limited to 0.5 nJ with accumulated nonlinear phase of 0.5 π. Further increase in pump power leads to pulse breaking. The above features are consistent with those of a dispersion-managed soliton laser.

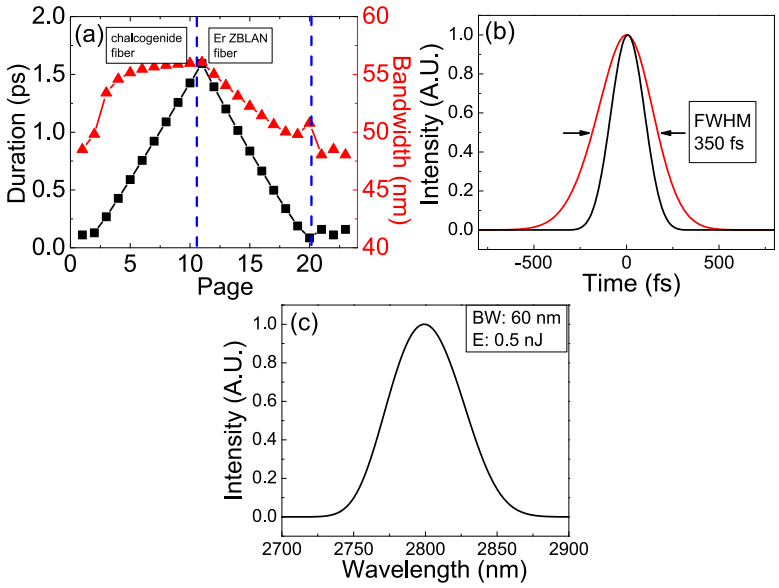

Figure 5.4: (a) Simulated variation of pulse duration and spectral bandwidth with net cavity dispersion of -0.0084 ps^2 (Page 22: spectral filter, Page 23: output port); (b) comparison between the output pulse and transform-limit pulse; (c) output spectrum with FWHM bandwidth of 60 nm.

Introducing more chalcogenide fiber can shift the cavity dispersion from slightly anomalous to the normal side. With 1.3-m long As_2S_3 fiber, the cavity dispersion is now 0.012 ps^2 and has converged solutions shown in Figure 5.5. The pulse evolution changes drastically from the previous one. Pulse shaping is defined by the strong dispersion map and the 100-nm wide gain filter together. Pulses get stretched in the As_2S_3 fiber and compressed in the Er ZBLAN gain fiber with a breathing ratio over 10. Pulses are always up-chirped throughout the whole cavity. However, in contrast with the nearly static spectral evolution in the previous design, significant spectral broadening happens in the As_2S_3 fiber, and then the bandwidth shrinks down to $\sim$ 100-nm bandwidth, with a breathing ratio of $\sim$ 3. The spectral shrinking in the gain segment is due to the intrinsic gain narrowing effect. The output pulses can be de-chirped to 120 fs, within 15% of the transform limited duration. The maximum pulse energy is limited to 3.6 nJ with an accumulated nonlinear phase $\sim 3\ \pi$.

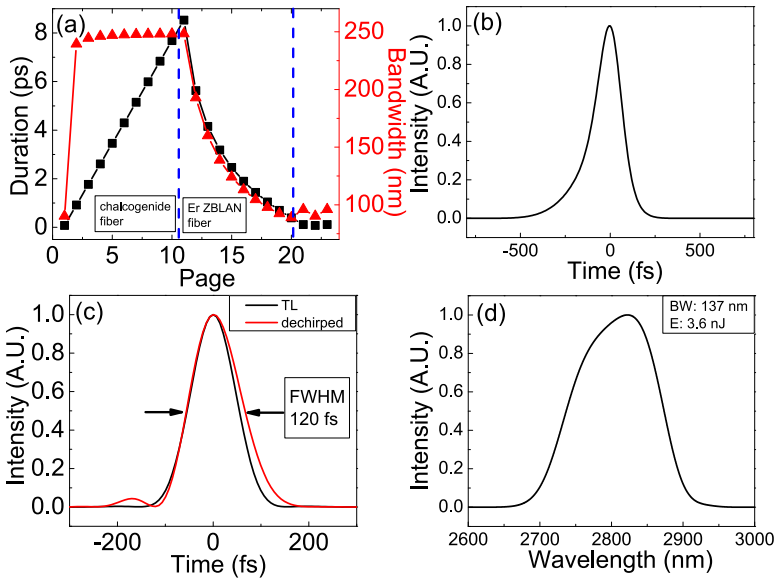

Figure 5.5: (a) Simulated variation of pulse duration and spectral bandwidth with net cavity dispersion of 0.012 ps^2 (Page 22: spectral filter, Page 23: output port); (b) output chirped pulse with duration of 177 fs; (c) comparison between the de-chirped pulse and transform-limit pulse; (d) output spectrum with FWHM bandwidth of 137 nm, corresponding to 106 fs.

This is a new kind of pulse evolution, different from all the previous evolutions. It is the result of the interplay of the strong dispersion map, the pulse shaping in the highly nonlinear passive fiber and the filter effect in the gain fiber. Pulses are first shaped towards the asymptotic solutions of the NLSE with nonlinearity and normal GVD, and become parabolic and get compressed in the gain fiber. A large breathing ratio makes it different from the static dissipative solitons [16]. The gain filter contributes to returning the pulse spectra back to the original state after a round trip, which is different from the passive self-similar evolution [17]. Amplifier similariton cannot exist in such a cavity with anomalous dispersion gain fiber. But one thing to keep in mind is that the shape of the gain spectra is Gaussian in the simulation, which is hardly the case in real fibers. These approximations, to some extent, can help us understand the potential pulse evolutions.

5.2.4 Simulation results for hybrid self-similar lasers

We further move on to study the lasers with larger normal cavity dispersion and introduce filters to stabilize the highly chirped pulses. Simulations converge for cavity GDD up to 1 ps^2.

Here we show an example of a typical converged solution with net cavity dispersion $\sim 0.1\ ps^2$ in Figure 5.6. The fiber segment consists of a 1.2-m long As_2S_3 fiber and a 1.6-m long Er ZBLAN gain fiber. A 30-nm Gaussian filter with peak transmission of 70% is used to achieve the broadest spectra for initial demonstrations. The gain saturation energy of 240 nJ is employed. The maximum output pulse energy can reach 188 nJ with transform limited duration of 120 fs. Chirped pulses can be de-chirped within 15% of the transform limited duration, indicating the linear chirp. Nonlinear phase accumulation is 35 π at this energy level.

It is shown in Figure 5.6(a) that the pulse evolution is strongly defined by the dispersion map and the filter effects, resulting from both the gain bandwidth and the introduced Gaussian filter. The breathing ratio is around 10 in both spectral and temporal domains as the pulse traverses the cavity, which is distinct from dissipative soliton or self-similar lasers. The pulses broaden significantly in the normal-dispersion parts and compress in the anomalous-dispersion sections, and are positively-chirped and far from the transform limited in the cavity.

These features are similar to those of the Tm laser at 2 μm [12]. Both of the lasers consist of the highly nonlinear fibers with normal dispersion, where the pulse is passively shaped towards a parabolic shape, as shown in Figure 5.6(c). On the other hand, there also remains important differences between them. The misfit parameter, which is the root-mean-square deviation of the pulse shape from

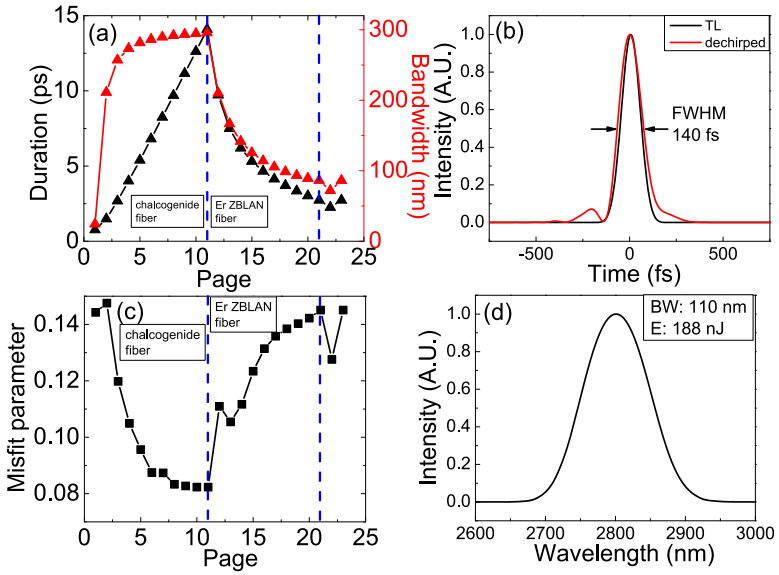

Figure 5.6: (a) Simulated pulse duration and spectral bandwidth with net cavity dispersion of 0.1 ps^2 (Page 22: spectral filter, Page 23: output port); (b) comparison between the de-chirped pulse and transform-limit pulse; (c) misfit parameter evolution compared with a parabolic pulse; (d) the output spectrum with FWHM bandwidth of 110 nm and pulse energy of 188 nJ.

a parabolic pulse, drops close to 0.08 in the chalcogenide fiber, and then deviates quickly from parabola when the pulse enters the anomalous gain fiber. While in the Tm laser, the pulses can maintain the parabolic shape in the gain fiber due to its minimal contributions to the pulse shaping. In the Tm laser, the spectra gets back to the original point mainly due to the filter introduced. However, in this laser, the spectra shrinking is the result of the joint actions of the gain narrowing and the filter.

Compared with the pulse evolution in the cavity with GDD of 0.012 ps^2 in Figure 5.5, this laser shares some common features. The main difference of design lies in the introduction of the extra narrow filter, which can accommodate much higher intra-cavity energy. Further increase in the length of the chalcogenide fiber pushes the cavity dispersion to a even larger value. Similar to the concept of giant chirp oscillator [18], the pulse energy is scaled almost linearly with the cavity

dispersion. But the advantages of this laser is that the chirped pulses can always be dechirped within 15% of the transform limited duration of 120 fs, which is ultimately determined by the Er gain bandwidth at 2.8 μm. This is not true for giant chirp oscillators.

5.3 Experiments

As a starting point to test the laser components and gain some understanding of the fiber parameters, a soliton Er ZBLAN laser similar to that in [7] was built. Then the chalcogenide fiber will be introduced in the cavity to change the cavity dispersion to the normal regime. Since the light is free-space coupled into the fibers in the cavity, the first step is to angle cleave the gain fiber to eliminate back reflections.

5.3.1 Fiber cleaving

Both ends of the gain fiber are angle cleaved at 8° to avoid the parasitic lasing, which can be detrimental to mode-locking. Some examples of bad and good angle cleaves are shown in Figure 5.7. Due to different material properties, a fiber cleaver with the capability of tuning the cleaving parameters is needed for Er ZBLAN fibers. Vytran cleaver (LDC-400) is employed for this task in this thesis. With too much tension applied along the fiber, the fiber end surface shows tension striations, which cause damage when the fiber end is pumped with high power. Tension needs to be set much lower compared to that used with silica fiber and the scribe delay should be set to a high value to allow time for the scribe to propagate. The tension

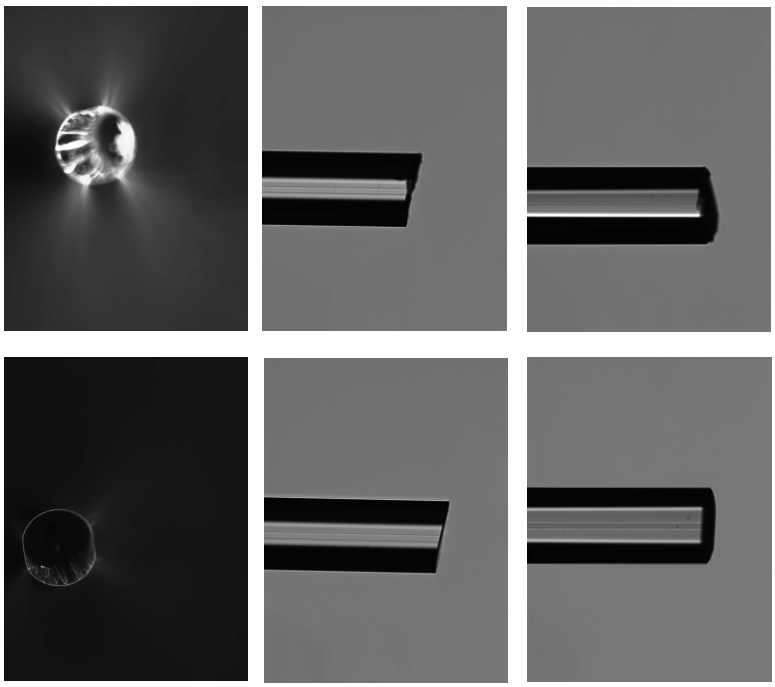

Figure 5.7: The end view, front view and back view of the bad angle cleave (top row) and good angle cleaves (bottom row).

used for Er ZBLAN fiber is 270 g and scribe delay is set to 1000 ms. Under these settings, angle cleaves in the bottom row of Figure 5.7 can be obtained consistently, and exhibit high threshold for self-lasing issues.

5.3.2 Soliton laser

We constructed the laser following the schematic in Figure 5.8 and the picture of the setup is in Figure 5.9. Pump light at 976 nm is first collimated by a B-coated lens (Thorlabs AC127-019-B-ML) and then focused into the Er ZBLAN fiber using lens with focal length of 15 mm (Thorlabs LB5766). This CaF_2 lens is uncoated to ensure the high transmission (95%) at both the pump wavelength and the signal wavelength (2.8 μm). The output power is measured after a long-pass filter that cuts on at 1650 nm, to eliminate unabsorbed pump light. Spectral measurements

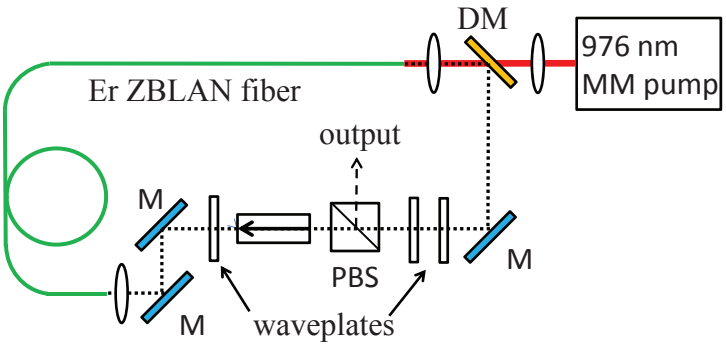

Figure 5.8: Schematic of the Er ZBLAN soliton laser: PBS: polarizing beam splitter; ISO: isolator; BPF: bandpass filter; M: mirror; DM: dichroic mirror.

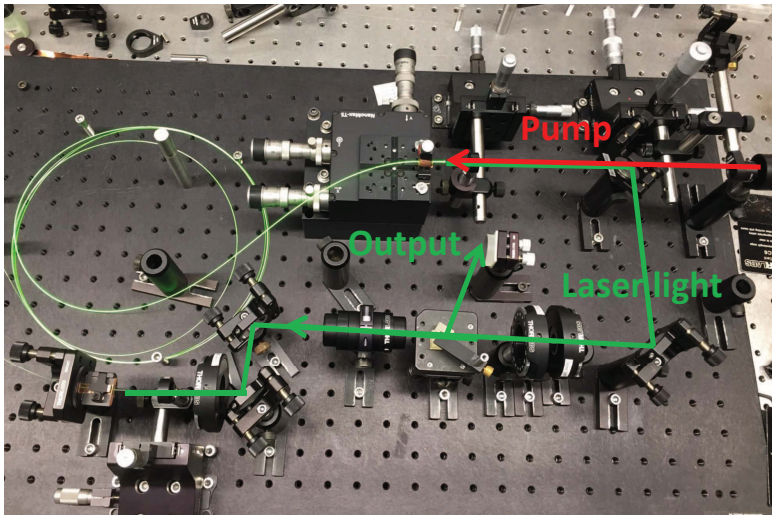

Figure 5.9: Picture of the Er ZBLAN soliton laser.Line with red color indicates the pump beam and the green one is the signal light.

were made using a Fourier-transform optical spectrum analyzer (OSA205), and temporal measurements were made using a mercury cadmium telluride (MCT) detector and electronic amplifier with a bandwidth of 1 GHz.

Slope efficiency of 17% is achieved with CW power of 400 mW obtained under 3-W incident pump power, shown in Figure 5.10. To operate the laser with CW power level of 10∼30 W, end cap protection is then required, which is done by splicing a short piece of AlF_3 fiber to both gain fiber ends.

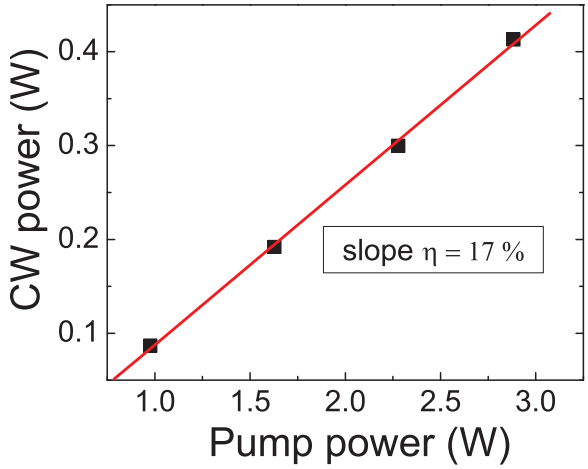

Figure 5.10: Slope efficiency of the Er ZBLAN soliton laser.

Currently the laser is prone to Q-switching due to large losses in the cavity, including the coupling loss and the loss at the isolator. Due to the mismatch of beam sizes at the entrance port of the isolator, a 50% loss is introduced. Further optimization of the efficiency is desirable to minimize the losses and reach mode-locking states of this laser.

5.4 Conclusion

In conclusion, the performance and behavior of the Er-doped ZBLAN fiber lasers are studied at net normal dispersion regime in simulations, including both the near-zero dispersion case and large normal dispersion case. A new kind of pulse evolution distinct from the previous evolutions is presented. It shares some common features of the passive self-similar lasers, but not the same. This pulse evolution can push the laser to operate at very large normal dispersion regime, like a GCO laser, but without loss of the capability to dechirp the output pulses within 15% of the transform limited duration. With promising simulation results of 188-nJ pulse energy and 140-fs de-chirped durations shown in this chapter, this hybrid self-

similar evolution awaits to be studied with further experimental evidence.

I want to thank Simon Duval and Vincent Fortin from Laval University for their helpful guidance on fiber cleaving. I also want to thank Prof. Liejia Qian from Shanghai Jiao Tong University for providing the dichroic mirror used in the experiments.

BIBLIOGRAPHY

[1] Y. Yao, A. J. Hoffman, and C. F. Gmachl, Nat. Photonics **6**, 432 (2012).

[2] C. Y. Wang, L. Kuznetsova, V. M. Gkortsas, L. Diehl, F. X. Kärtner, M. a. Belkin, A. Belyanin, X. Li, D. Ham, H. Schneider, P. Grant, C. Y. Song, S. Haffouz, Z. R. Wasilewski, H. C. Liu, and F. Capasso, Opt. Express **17**, 12929 (2009).

[3] O. Chalus, P. K. Bates, M. Smolarski, and J. Biegert, Opt. Express **17**, 3587 (2009).

[4] V. Fortin, M. Bernier, S. T. Bah, and R. Vallée, Opt. Lett. **40**, 2882 (2015).

[5] Y. O. Aydin, V. Fortin, F. Maes, F. Jobin, S. D. Jackson, R. Vallée, and M. Bernier, Optica **4**, 6 (2017).

[6] T. Hu, S. D. Jackson, and D. D. Hudson, Opt. Lett. **40**, 4226 (2015).

[7] S. Duval, M. Bernier, V. Fortin, J. Genest, M. Piche, and R. Vallee, Optica **2**, 623 (2015).

[8] S. Duval, M. Olivier, V. Fortin, M. Bernier, M. Piche, and R. Vallée, SPIE Fiber Lasers XIII Technol. Syst. Appl. **9728**, 2 (2016).

[9] S. Antipov, D. D. Hudson, A. Fuerbach, and S. D. Jackson, Optica **3**, 1373 (2016).

[10] A. Chong, J. Buckley, W. Renninger, and F. Wise, Opt. Express **14**, 10095 (2006).

[11] W. H. Renninger, A. Chong, and F. W. Wise, Phys. Rev. A **82**, 021805 (2010).

[12] Y. Tang, A. Chong, and F. W. Wise, Opt. Lett. **40**, 2361 (2015).

[13] W. Ettoumi, Y. Petit, J. Kasparian, and J.-P. Wolf, Opt. Express **18**, 6613 (2010).

[14] R. T. White and T. M. Monro, Opt. Lett. **36**, 2351 (2011).

[15] C. Xiong, E. Magi, F. Luan, A. Tuniz, S. Dekker, J. S. Sanghera, L. B. Shaw, I. D. Aggarwal, and B. J. Eggleton, Appl. Opt. **48**, 5467 (2009).

[16] W. Renninger, A. Chong, and F. Wise, Phys. Rev. A **77**, 023814 (2008).

[17] F. Ilday, J. Buckley, W. Clark, and F. Wise, Phys. Rev. Lett. **92**, 213902 (2004).

[18] W. H. Renninger, A. Chong, and F. W. Wise, Opt. Lett. **33**, 3025 (2008).

CHAPTER 6

FUTURE DIRECTIONS

6.1 Thulium fiber lasers with all normal-dispersion cavity

6.1.1 Modulation instability in Tm fiber laser

The operation of fiber lasers in the normal dispersion regime is well-known to produce high-energy short pulses with dissipative soliton or self-similar evolutions. This is one of the motivations to develop high energy fiber lasers at 2 μm, where the benefits of normal-dispersion operation hasn't been fully exploited. In the previous chapter, a Tm fiber laser operating at large normal dispersion with hybrid self-similar evolution has been demonstrated, with a 4-fold improvement in peak power. But these performances are still not even close to the full potential of generating femtosecond pulses in Tm fiber lasers.

As a follow-up study of the Tm fiber laser in Chapter 3 to further improve the performance, efforts have been devoted to understand the role of the anomalous dispersion in both the Tm gain fiber and the passive fibers. It's already shown that the modulation instability (MI) in optical fiber amplifiers and fiber lasers with anomalous dispersion leads to continuous wave radiation breakup [1]. This is a detrimental effect limiting the performance with the growth rate of the perturbations in the anomalous amplifiers being superexpressive. The anomalous dispersion significantly lowers the threshold for pulse break-up compared to those where the gain dispersion is normal.

Even when the gain dispersion is normal, but with anomalous-dispersion seg-

ment after the gain, the performance of the Tm laser is still greatly limited. In simulations, it shows a clear trend that with shorter and shorter passive fiber (SMF28e) after the Tm gain fiber, the output pulse energy can be increased significantly. Pulses with 100 nJ and transform limited duration of 100 fs can be obtained solely by removing the passive fiber after the gain.

Some initial experiments were done to test this finding by cutting down the SMF28e after the gain from 40 cm to 30 cm long. However, similar results were obtained compared to the previous ones. Further cutting down was limited by the practical issues, such as the minimum fiber pigtail length required by the collimator. The nonlinear length in SMF28e for the pulses right after the gain fiber (4-ps, 12-nJ) is $\sim$ 20 cm, which is at the same level where the fiber was cut down to. So this initial test couldn't help to prove the simulation results. In the future, a customized collimator with normal dispersion fiber pigtail, such as UNHA4 fiber, can be implemented to eliminate the anomalous passive fiber and test this concern.

Another signature of MI happening inside the cavity is based on the fringes sitting on the mode-locked spectrum in Figure 6.1. It is studied in [2] that the positions of the adjacent fringes on the spectrum contains information of the net cavity dispersion.

These fringes are different from the Kelly sidebands [3] we would observe in a typical soliton laser. They have different mechanism and these sidebands can cause long pedestals in the time domain. The relationship between the positions of the sidebands and the net cavity dispersion can be modeled through Eq. 6.1 and Eq. 6.2, where f_c is the center frequency in THz and f_k is the k-th sideband frequency from the center, and their distance is defined as Δf_k.

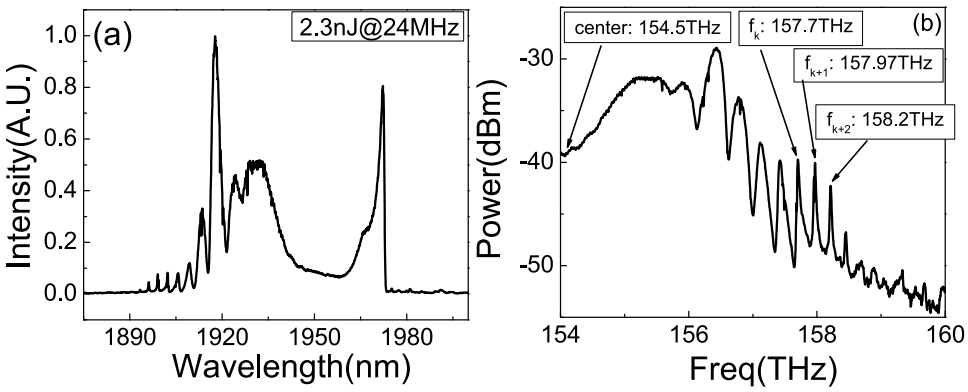

Figure 6.1: (a) Mode-locked spectrum from the Tm fiber laser in Figure 3.1; (b) Zoomed-in spectrum in THz unit with multiple peaks indicated.

$$\Delta f_k = f_k - f_c \tag{6.1}$$

$$2\pi^2 \beta_2 L({\Delta f_{k+1}}^2 - {\Delta f_k}^2) = 2\pi \tag{6.2}$$

From the relationship above, the net cavity dispersion of the laser in Figure 3.1 is calculated to be $GDD = \beta_2 L = 0.18 ps^2$. Compared with the dispersion value ($0.34\ ps^2$) calculated using the simulation parameters, this number is only half of that. But it's close to the pulse chirp of $0.22\ ps^2$ inferred from the de-chirping process. So this method may provide some useful information to understand the pulse evolution, since the comparable pulse chirp with the cavity GDD is a feature of self-similar evolution.

6.1.2 Dissipative soliton Tm fiber laser

It's desirable to set up the Tm laser with all normal-dispersion fibers in the cavity. Due to the intrinsic anomalous material dispersion of silica fiber at 2 μm, the

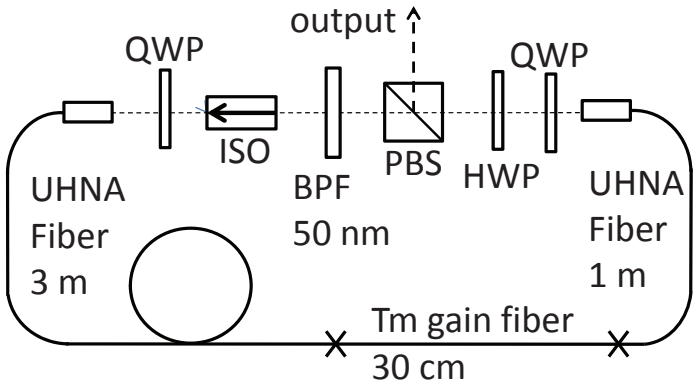

Figure 6.2: The schematic of the all normal-dispersion Tm laser design with filter bandwidth of 50 nm.

way to obtain normal dispersion fibers is either through the small core design of the fiber or doping the ions in different glass materials, such as the silicate glass. Experimentally, a 30-cm long Tm gain fiber with normal dispersion was demonstrated with a gain per unit length of 2 dB/cm [4]. Simulations of cavities employing this 30-cm long gain fiber were conducted to assess the advantages. The laser design is shown in Figure 6.2 with 3-m and 1-m long passive fiber (UHNA4) on two sides of the gain fiber. The parameters used in the simulation are listed in Table 6.1. A 50-nm bandwidth bandpass filter is used in the cavity.

Table 6.1: Values of fiber parameters used in the Tm ANDi laser

Fiber	Aeff	GVD	TOD	Length
	(μm^2)	(fs^2/mm)	(fs^3/mm)	(m)
UHNA4	23	93	154	4
Tm	21	17	0	0.3

An example of a typical converged solution is shown in Figure 6.3 with GDD $\sim$ 0.28 ps^2. The features of the characteristic steep edges and bat-man ear spectra indicate the operation regime of the laser to be dissipative soliton [5]. The maximum pulse energy can reach 280 nJ with output spectra to support 70-fs pulses. The pulses can be de-chirped using only second order dispersion compensation to 90

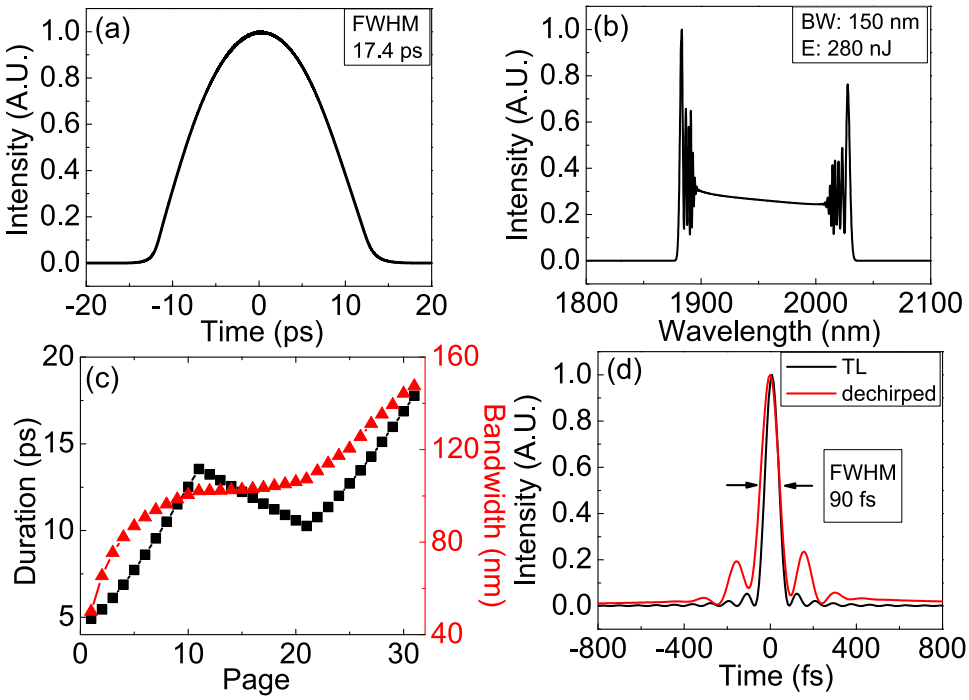

Figure 6.3: (a) Simulated output chirped pulse; (b) output spectrum with 150-nm bandwidth and 280-nJ pulse energy; (c) spectral and temporal evolution along the cavity; (d) comparison between the de-chirped pulse (90 fs) and the transform-limit pulse (70 fs).

fs. These results are way beyond the performance of the Tm lasers demonstrated with anomalous gain fiber and passive fibers inside the cavity.

6.1.3 Amplifier similariton Tm fiber laser

Another benefit of having normal dispersion Tm gain fiber is to enable the design the amplifier similariton laser near 2 μm. The wisdom here is to employ lower doped and longer gain fiber, and the cavity is stabilized by a narrow filter [6]. The laser design is similar to that in Figure 6.2, but with a 2-m long gain fiber and 30-cm, 20-cm long passive fiber (UHNA3) on two sides of the gain fiber. The parameters are listed in the Table 6.2. A 20-nm bandwidth bandpass filter is used

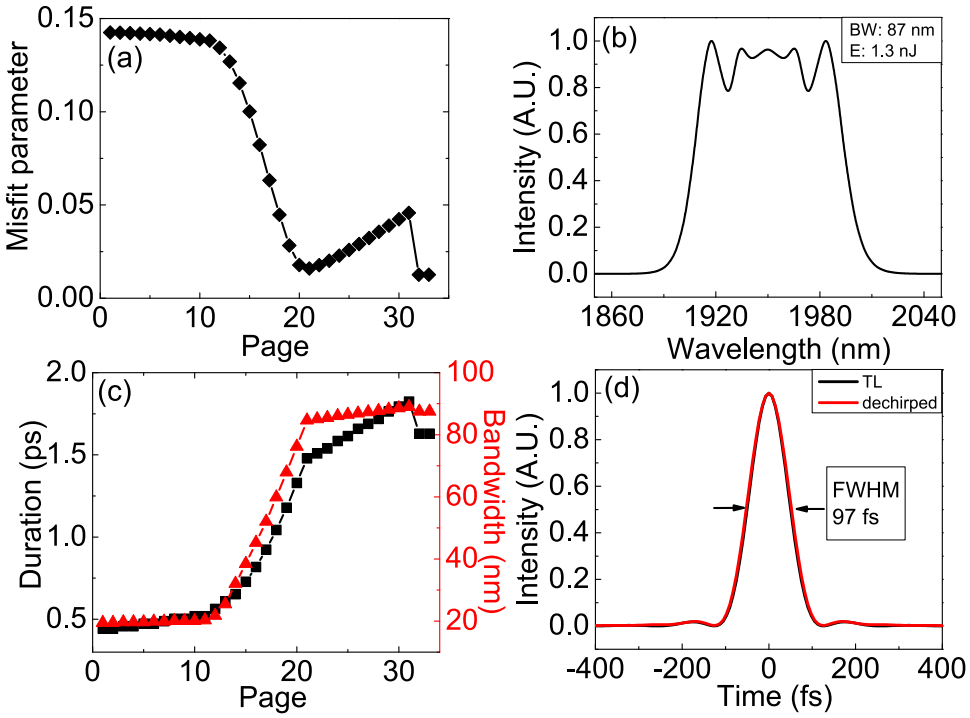

Figure 6.4: (a) Evolution of the misfit parameter comparing the pulse profile to a parabola; (b) output spectrum with 87-nm bandwidth; (c) spectral and temporal evolution inside the cavity; (d) comparison between the de-chirped pulse (97 fs) and the transform-limit pulse.

in the cavity.

Table 6.2: Values of fiber parameters used in the Tm amplifier similariton laser

Fiber	Aeff	GVD	TOD	Length
	(μm^2)	(fs^2/mm)	(fs^3/mm)	(m)
UHNA3	39	30.5	154	0.5
Tm	21	17	0	2

The converged solution with GDD $\sim 0.05\ ps^2$ is shown in Figure 6.4. Figure 6.4(a) describes the evolution of the misfit parameter M, which is the root-mean-square deviation of the pulse shape from a parabolic pulse with the same energy. With M being close to 0, the pulse shape is more like a parabola. We can see that the pulses start with Gaussian shape (M $\sim$ 0.14) propagate in the first segment of passive fiber without too much changes in shapes, then get attracted to

the asymptotic solution in the gain fiber and obtain the parabolic shape. In Figure 6.4(c), the pulse duration and spectral bandwidth breathe by a factor of 4 and 8 respectively as the pulse traverses the cavity. The pulses can be de-chirped almost as same as the transform limited pulses, due to the linear chirp. The amount of pulse chirp inferred from the de-chirping process is $\sim 0.038\ ps^2$, lower than the net cavity dispersion, which is also a feature of amplifier similariton evolution. Further improvement in the laser design is needed to optimize the laser performance. This laser can also serve as the basis for obtaining high-energy short pulse generation using the idea of extended self-similar evolution.

6.2 Divided-pulse Tm laser

It's been demonstrated by Erin Lamb and coworkers in [7] that the soliton energy can be increased by an order of magnitude employing the idea of divided pulse amplification in a fiber laser. Other interesting pulse evolutions, especially those in the normal dispersion regime, have also been demonstrated in her thesis. It would be very interesting to see how this idea can be applied in Tm fiber lasers. Theoretically, this idea can be applied to lasers at any wavelengths, as long as the pulse dividing and combining can be done in the right way, which motives my initial work towards this direction.

The working principle of this laser is to divide the input linearly-polarized pulses using the birefringent crystals into multiple copies of subpulses with equal energies, but perpendicular polarizations. After being amplified in the gain fiber, these pulses are recombined together to form a single pulse with high intensity. In this way, the soliton area theorem can be broken through and nonlinear phase

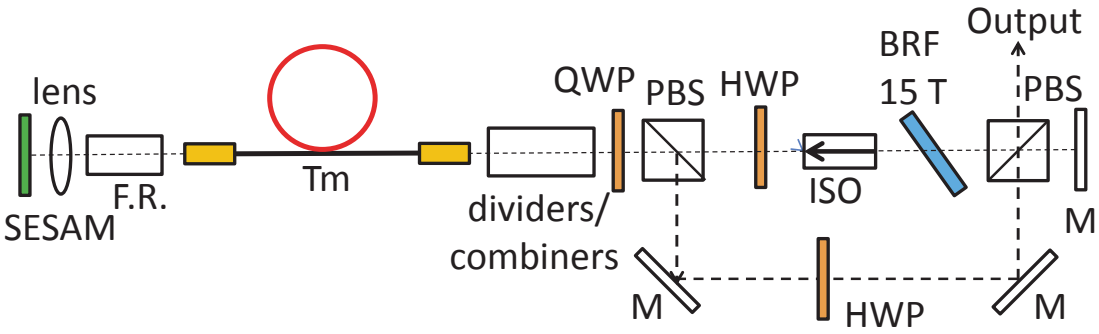

Figure 6.5: Schematic for the divided-pulse Tm fiber laser: BRP: birefringent plate; PBS: polarizing beam splitter; ISO: isolator; F.R: Faraday Rotator; M: mirror.

accumulation can be reduced by 16 times, provided 4 crystals are used.

The cavity design in Figure 6.5 for the divided-pulse Tm fiber laser is similar to that in [7]. The divider/combiner part in the cavity is formed with the same set of YVO_4 crystals. After the pulses pass through the Faraday rotator twice, the polarizations of the pulses are rotated 90 degree and they will be recombined on their way back.

As a first step, the cavity is built up without the divider/combiner inside the cavity. With no dispersion compensation, this laser has a cavity dispersion of -0.4 ps^2 and should mode-lock as a soliton laser. The birefringent plate with thickness of 15 T serves as a 30 nm bandwidth filter to facilitate the mode-locking process, since the Tm laser has a broad bandwidth and have multiple lasing peaks. After aligning the laser without any self-lasing issue, the mode-locking can self start once the pump power is turned up. The mode-locked spectrum is shown in Figure 6.6(a). Distinctions from a regular soliton behavior are reduced spectrum bandwidth, suppressed large-width soliton sidebands in Figure 6.6(b).

An important feature of the autocorrelation trace is that it always contains

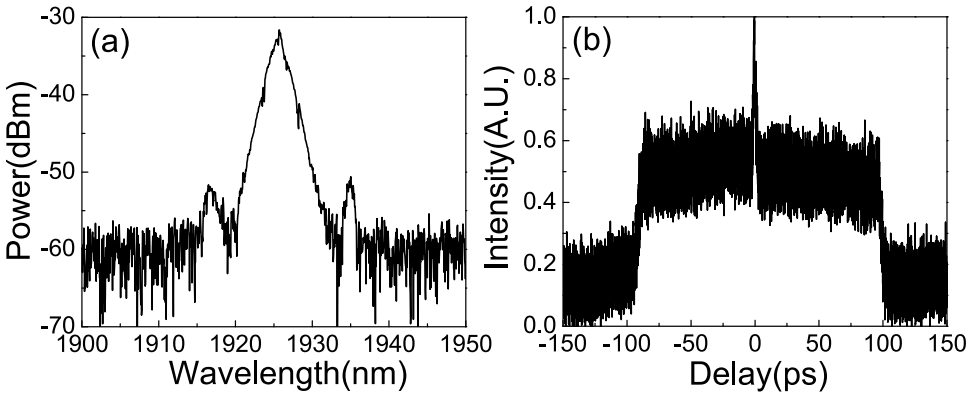

Figure 6.6: (a) Modelocked spectrum; (b) autocorrelation of the Tm soliton laser in divided-pulse configuration.

a remarkable pedestal which cannot be eliminated. Efforts have been made to slowly decrease the pump power with different NPE settings, but the background is consistently happening. From a paper on the impact of gain fiber dispersion on the stability of soliton bound states [8, 9], this pedestal is the result of averaging several irregular bunching solitons. This happens mainly due to the combination of the slow response from SESAM and the anomalous dispersion from the gain fiber. The slow response component of SESAM ($\sim$ 10 ps) provides the attraction force for the soliton bunching. But if a fast SA were used in the same cavity, bunching is not observed for all pump power level. So in the case of anomalous Tm gain fiber, NPE is the ideal option as SA to avoid this bunching effect.

To assess the idea of adding NPE segment into the cavity as a fast saturable absorber, the laser is redesigned with an extra NPE-arm formed by a 7-m long SMF28e fiber. The mode-locking is achieved by the combination of the SESAM and NPE in this case. It is very clear from Figure 6.8 that the spectra is now a typical soliton spectrum with sharp peaks at the position of the Kelly sidebands. And the autocorrelation trace indicates there're just discrete pulses without any bunching effect. Single-pulsing state is hard to obtain with decreasing pump power.

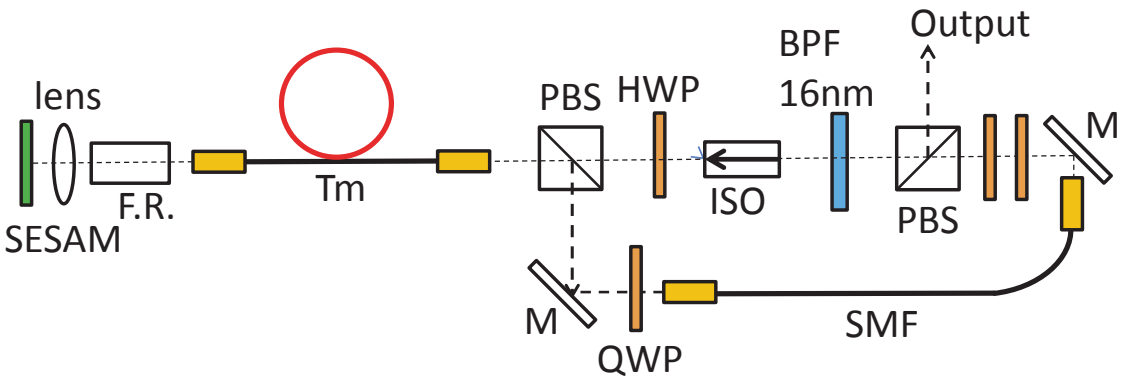

Figure 6.7: Schematic for the divided-pulse Tm fiber laser with NPE for mode-locking.

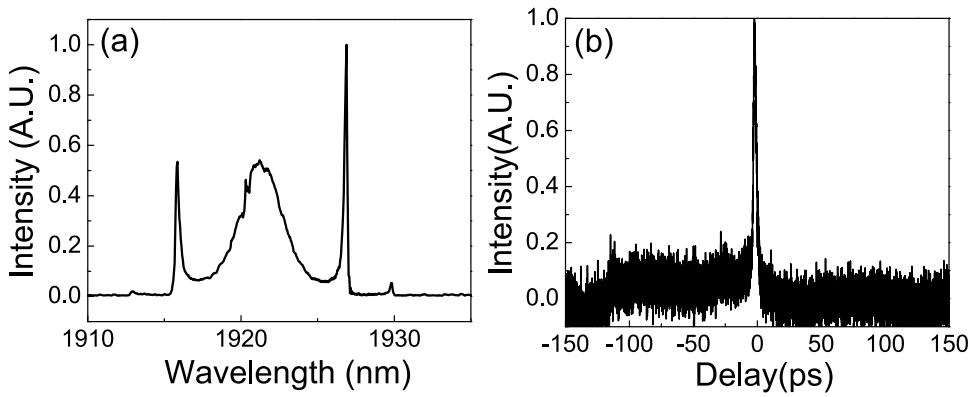

Figure 6.8: Mode-locked spectrum (a) and autocorrelation (b) of the Tm soliton laser in divided-pulse configuration, without SESAM.

The continuous-wave lasing threshold is always reached first before the level for the single pulse is reached. More efforts are needed to optimize the cavity to solve this issue.

If the Tm gain fiber with normal dispersion is available, the NPE segment is not necessary. The discrete pulsing states are still achievable even with slow SESAMs. Further pursing the divided-pulse Tm laser is stopped at this stage, and more work needs to be done to redesign the cavity dispersion and obtain the single pulsing state. In this sense, the normal dispersion gain fiber is relevant, since it's

the solution to avoid soliton bunching, provided fast SESAMs are not available.

6.3 Modelocked praseodymium fiber laser at 5 μm and its application

Mid-infrared region has intrigued lots of interest in optical communities to develop new kinds of ultrafast light sources for various applications. These can be focused on generating femtosecond or picosecond pulses with new colors at different energy levels. One of the important applications of mid-infrared lasers is supercontinuum generation for molecular detection and identification. This leads us to think about a more important question: what kind of fiber lasers are the most helpful for an all-fiber version mid-infrared supercontinuum light source?

As is well known, to generate a flat and broad supercontinuum, it's optimal to launch the input pulses near the fiber's zero dispersion wavelength (ZDW) at the anomalous dispersion side, making use of the soliton fission and Raman effect [10]. Among the mid-infrared materials with low loss over 3-12 μm region are chalcogenide, silicon, silicon nitride, which all share the ZDW in the range of 4 $\sim$ 5 μm. Aside from the advantages of fiber lasers in terms of compactness, minimal maintenance, no requirement for water cooling, it will have huge impact if a pulsed fiber laser operating at 5 μm is available. This is the key to realize an all-fiber mid-IR supercontinuum light source.

People have already been thinking along this direction to build fiber lasers at increasingly longer wavelengths, such as 2 μm [11, 12, 13] and 2.8 μm [14, 15]. Based on the study of pulse evolutions in modelocked 1 μm fiber lasers and the fact

that the nonlinear effect scales inversely with the third power of the wavelength, it is advantageous and natural to develop fiber lasers with much higher energies at longer wavelengths.

With fiber lasers developed at a few mid-infrared wavelength points, the most direct way to obtain other colors is through soliton self-frequency shift (SSFS) [16]. Recently, the mW-level average power of the shifted soliton has been improved up to watt level [17], covering $2.8 \sim 3.6\ \mu m$. These results have shown some promising aspects of an all-fiber version source, but still need more wavelength shifting to reach broader region. A mode-locked fiber laser emitting femtosecond pulses near $5\ \mu m$ would be a great replacement of the first stage of SSFS process, reducing the intensity fluctuation and noises.

One of the appropriate host materials for the mid-infrared fiber lasers is chalcogenide glass. Doping chalcogenide fibers with Pr^{3+} ions can have emission peaks centered at $5\ \mu m$, when pumped at $2.04\ \mu m$ [18, 19]. The gain bandwidth at $5\ \mu m$ is around 600 nm wide in Figure 6.9 [19], which supports pulse duration of sub-50 fs.

Although there have been a few theoretical and computational studies of Pr^{3+} doped chalcogenide fiber emission at $5\ \mu m$ [15], no mid-infrared fiber lasers have been demonstrated over $4\ \mu m$ wavelength for two main reasons. First, the fabrication of these fibers can be challenging [20, 21] and a fast growth in developing fiber lasers at $5\ \mu m$ wouldn't be easy until all the components are well established. Another reason is that both the upper and lower laser manifolds possess long lifetimes compared to that of the ground state [21] and resonant pumping by quantum cascade laser may be needed. Despite the difficulties currently we have in working with Pr-doped fibers, the idea of developing such a source at $5\ \mu m$ is still valuable

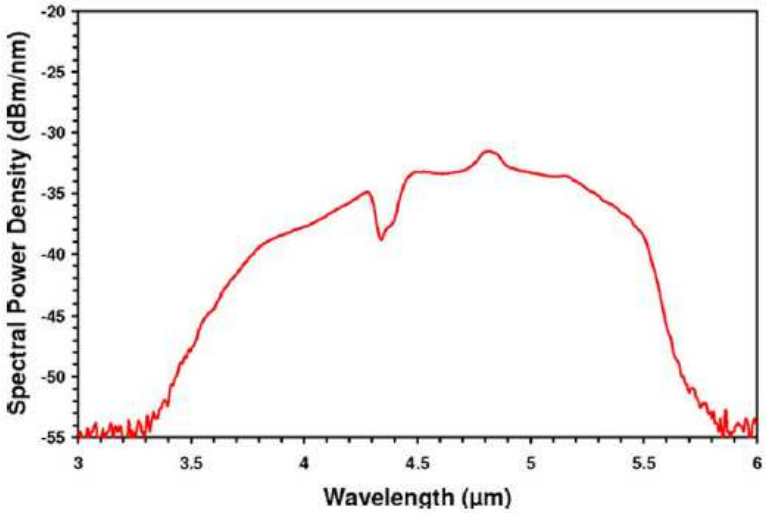

Figure 6.9: Broadband emission in the 3∼5 μm wavelength region from a diode-pumped Pr^{3+} doped chalcogenide fiber source.

and should be kept in mind, in case the components are available in the future.

If we come back to the discussion about the light sources we want, intense ultrashort pulses at 2.5-6 μm can be used for multi-photon MIR spectroscopy. This is in line with the work on developing high-energy fiber lasers at 2.8 μm and making use of the SSFS to get access to other color regions. Supercontinnum generation at watt-level average power covering up to 13 μm in an all-fiber format would be ideal for molecular detection, breath analysis and environmental monitoring, etc.

BIBLIOGRAPHY

[1] A. Rubenchik, S. Turitsyn, and M. Fedoruk, Proc. SPIE - Int. Soc. Opt. Eng. **7914**, 2684 (2011).

[2] J. Peng, L. Zhan, Z. Gu, J. Liu, S. Luo, X. Shen, and Q. Shen, J. Light. Technol. **30**, 2707 (2012).

[3] S. Kelly, Electron. Lett. **28**, 806 (1992).

[4] Q. Wang, J. Geng, T. Luo, and S. Jiang, Opt. Lett. **34**, 3616 (2009).

[5] A. Chong, W. H. Renninger, and F. W. Wise, Opt. Lett. **32**, 2408 (2007).

[6] W. H. Renninger, A. Chong, and F. W. Wise, Phys. Rev. A **82**, 021805 (2010).

[7] E. S. Lamb, L. G. Wright, and F. W. Wise, Opt. Lett. **39**, 2775 (2014).

[8] R. Gumenyuk and O. G. Okhotnikov, IEEE Photonics Technol. Lett. **25**, 133 (2013).

[9] R. Gumenyuk, M. S. Gaponenko, K. V. Yumashev, A. A. Onushchenko, and O. G. Okhotnikov, IEEE J. Quantum Electron. **48**, 903 (2012).

[10] I. Kubat, C. S. Agger, U. Møller, A. B. Seddon, Z. Tang, S. Sujecki, T. M. Benson, D. Furniss, S. Lamrini, K. Scholle, P. Fuhrberg, B. Napier, M. Farries, J. Ward, P. M. Moselund, O. Bang, L. Laser, P. Ohg, T. Max-planck str, and K.-l. Germany, Opt. Express **22**, 4887 (2014).

[11] L. E. Nelson, E. P. Ippen, and H. a. Haus, Appl. Phys. Lett. **67**, 19 (1995).

[12] F. Haxsen, D. Wandt, U. Morgner, J. Neumann, and D. Kracht, Opt. Express **18**, 18981 (2010).

[13] Y. Tang, A. Chong, and F. W. Wise, Opt. Lett. **40**, 2361 (2015).

[14] S. Duval, M. Olivier, V. Fortin, M. Bernier, M. Piche, and R. Vallée, SPIE Fiber Lasers XIII Technol. Syst. Appl. **9728**, 2 (2016).

[15] T. Hu, S. D. Jackson, and D. D. Hudson, Opt. Lett. **40**, 4226 (2015).

[16] Y. Tang, L. G. Wright, K. Charan, T. Wang, C. Xu, and F. W. Wise, Optica **3**, 948 (2016).

[17] S. Duval, J.-C. Gauthier, L.-R. Robichaud, P. Paradis, M. Olivier, V. Fortin, M. Bernier, M. Piché, and R. Vallée, Opt. Lett. **41**, 5294 (2016).

[18] Ł. Sójka, Z. Tang, H. Zhu, E. Bereś-Pawlik, D. Furniss, A. B. Seddon, T. M. Benson, and S. Sujecki, Opt. Mater. Express **2**, 1632 (2012).

[19] J. S. Sanghera, L. B. Shaw, and I. D. Aggarwal, IEEE J. Sel. Top. QUANTUM Electron. J. Sel. Top. QUANTUM Electron. **15**, 114 (2009).

[20] Z. Tang, D. Furniss, M. Fay, H. Sakr, L. Sójka, N. Weston, S. Sujecki, T. M. Benson, A. B. Seddon, N. Nanoscience, N. Centre, N. Ng, L. Sjka, N. Neate, N. Weston, S. Sujecki, T. M. Benson, and A. B. Seddon, Opt. Mater. Express **5**, 870 (2015).

[21] L. Sójka, Z. Tang, D. Furniss, H. Sakr, E. Bereś-Pawlik, A. B. Seddon, T. M. Benson, and S. Sujecki, Opt. Quantum Electron. **49**, 21 (2017).

APPENDIX A: FIBER PARAMETERS

A.1 Mathematica code for calculating the fiber parameters

This thesis involves simulations of single-mode fiber lasers using relevant fiber parameters, such as dispersion and effective area. It's helpful to show how to implement these calculations using Mathematica. This section provides the code used to calculate the parameters for single mode fibers.

Usually we obtain the fiber parameters such as the NA and core sizes from manufacturers. These can help us calculate the waveguide dispersion. Most of the fibers used in this thesis are silica fibers and we can calculate the material dispersion using the refractive index information for silica glass. These two dispersion functions combined can yield the total dispersion at different wavelengths.

An illustration of using the code to calculate the dispersion of the fiber Hi1060 at 1 μm is shown below. The fiber Hi1060 has $NA = 0.14$ and core diameter of 5.3 μm, and it's often used in the Yb fiber lasers. In the code, all the wavelength terms are in the unit of μm and the effective area is in the unit of μm^2.

cutoff:=0.97

NA:=0.14

***c*:=0.3**

delta = 0.5 * NA^2/1.45^2

0.00466112

```
a = cutoff * 2.405/(2 * π * NA)
```

2.65203

```
V[λ_] = 2 * π * a * NA/λ;
```

```
V[1.03]
```

2.2649

```
MFR[λ_] = a * (0.65 + 1.619V[λ]^(-3/2) + 2.879V[λ]^(-6));
```

```
MFR[1.03]
```

3.04004

```
Aeff[λ_] = π * MFR[λ]^2;
```

```
Plot[Aeff[λ], {λ, 0.8, 2.0}, AxesLabel → {"Wavelength (μm)", "Aeff (μm^2)"},
PlotStyle → {Blue, Thick}, BaseStyle → {FontWeight → "Bold", FontSize → 16}]
```

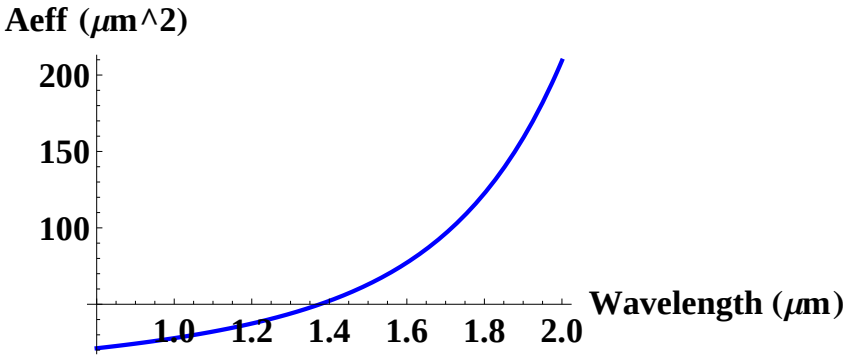


```
Aeff[1.03]
```

29.0341

```
n[λ_] = √(1 + ((6.996166300 * 10^ - 1) * λ^2/(λ^2 - (4.67914826 * 10^ - 3)))+
```

```
(((4.07942600 * 10^ - 1) * λ^2)/(λ^2 - (1.35120631 * 10^ - 2)))+
(((8.97479400 * 10^ - 1) * λ^2)/(λ^2 - (9.79340025 * 10^1))));

n[1.03]
```

1.45124

```
Ka[V_] = (1 + Sqrt[2])/(1 + (4 + V^(4))^(1/4));

b[V_] = 1 - (Ka[V])^2;

aa[λ_] = D[V * b[V], {V, 2}]/.V->2 * π * a * NA/λ;

WvgdDisp[λ_] = -(delta * n[λ] * 1000/(λ * .3)) * (V[λ] * aa[λ]);

WvgdGVD[λ_] = -(λ^2) * WvgdDisp[λ]/(2 * π * .3);
WvgdTOD[λ_] = -(λ^2) * D[WvgdGVD[λ], {λ, 1}]/(2 * π * .3);
WvgdFOD[λ_] = -(λ^2) * D[WvgdTOD[λ], {λ, 1}]/(2 * π * .3);

Plot[WvgdDisp[λ], {λ, 0.8, 1.5}, AxesLabel → {"Wavelength (μm)",
"Waveguide dispersion (ps/nm/km)"}, PlotStyle → {Blue, Thick},
BaseStyle → {FontWeight → "Bold", FontSize → 16}]
```

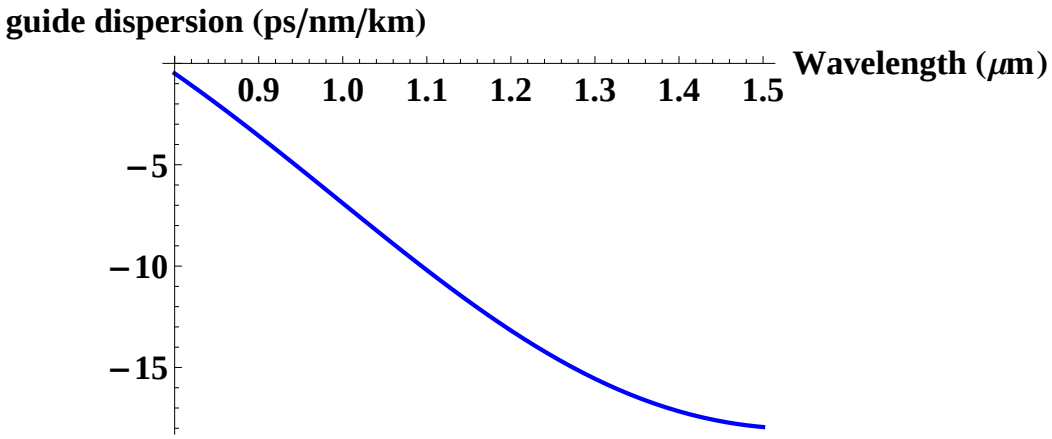

```
Plot[WvgdGVD[λ], {λ, 0.8, 1.5}, AxesLabel → {"Wavelength (μm)",
"Waveguide GVD (fs^2/mm)"}, PlotStyle → {Blue, Thick},
BaseStyle → {FontWeight → "Bold", FontSize → 16}]
```

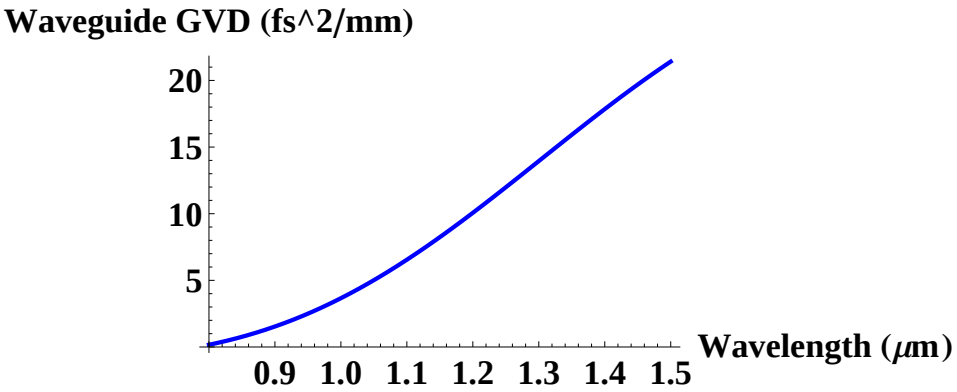


```
MatDisp[λ_] = −(λ) * D[n[λ], {λ, 2}] * 1000/(.3);

MatGVD[λ_] = (λ^3) * D[n[λ], {λ, 2}] * 1000/(2 * π * .3^2);
MatTOD[λ_] = −(λ^2) * D[MatGVD[λ], {λ, 1}]/(2 * π * .3);
MatFOD[λ_] = −(λ^2) * D[MatTOD[λ], {λ, 1}]/(2 * π * .3);

Plot[MatGVD[λ], {λ, 0.8, 1.5}, AxesLabel → {"Wavelength (μm)",
"Material GVD (fs^2/mm)"}, PlotStyle → {Blue, Thick},
BaseStyle → {FontWeight → "Bold", FontSize → 16}]
```

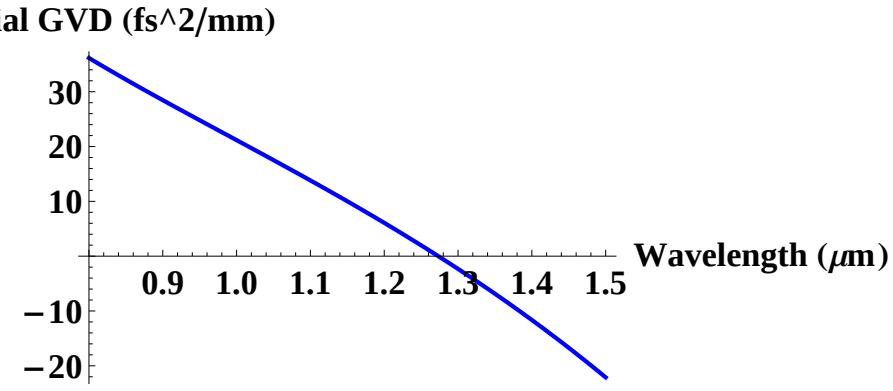


```
Plot[{MatGVD[λ] + WvgdGVD[λ]}, {λ, 0.8, 1.5}, AxesLabel →
```

{"Wavelength (μm)", "GVD (fs^2/mm)"}, PlotStyle → {Blue, Thick},

BaseStyle → {FontWeight → "Bold", FontSize → 16}]

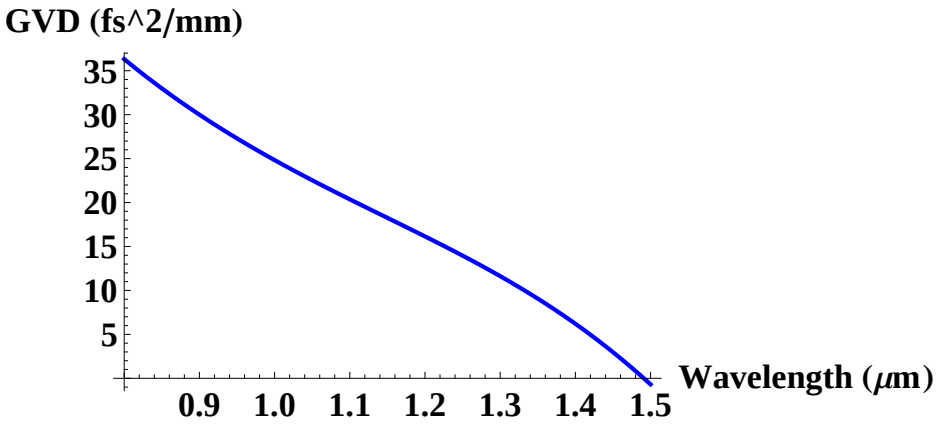

WvgdGVD[1.03]

MatGVD[1.03]

4.44843

18.9889

beta[λ_] = MatGVD[λ] + WvgdGVD[λ];

MatGVD[λ] + WvgdGVD[λ]/.λ → 1.03

23.4373

MatTOD[λ] + WvgdTOD[λ]/.λ → 1.03

25.6112

MatFOD[λ] + WvgdFOD[λ]/.λ → 1.03

−9.58417

Plot[{MatTOD[λ] + WvgdTOD[λ]}, {λ, 0.8, 1.5}, AxesLabel →

{"Wavelength (μm)", "TOD (fs^3/mm)"}, PlotStyle → {Blue, Thick},

BaseStyle → {FontWeight → "Bold", FontSize → 16}]